A polarised neutron study of the dynamic properties of energy materials

Sercan Arslan

Royal Holloway
University of London

A dissertation submitted to the University of London
for the degree of Doctor of Philosophy

December 2021

Declaration of Authorship

I, Sercan Arslan, hereby declare that this thesis and the work presented in it is entirely my own. Where I have consulted the work of others, this is always clearly stated.

Signed: _____

Date: _____

Abstract

The microscopic diffusion of ions in two classes of energy materials, thermoelectric $AgCrSe_2$ and battery cathode $Na_xFe_{1/2}Mn_{1/2}O_2$, have been studied. The use of neutron polarisation analysis to separate the scattering components has been crucial to both studies.

In the case of $AgCrSe_2$, diffuse QENS in the superionic phase thought to arise from ionic diffusion is in fact largely comprised of coherent scattering with a small contribution from magnetism. These results challenge the validity of the PLEC concept in $AgCrSe_2$. Magnetic excitations below $T_N \approx 55\,K$ have been investigated using high resolution neutron spectroscopy, and simulated with the SpinW package. The proposed magnetic Hamiltonian provides a good description of the resolvable magnetic excitations over the entire energy spectrum.

Single-crystal diffraction from P2-$Na_{0.67}Fe_{1/2}Mn_{1/2}O_2$ show that superstructure formation is not suppressed by disorder in the transition-metal layer, and suggests that details of the resulting structure are altered. Polarised QENS from the P2 composition reveals a diffusion mechanism involving two distinct sites. The diffusion rate is an order of magnitude greater than for P2-$Na_{0.8}CoO_2$ at $T \approx 530\,K$, with a more favourable activation energy for battery performance. The diffusion rate in P2-$Na_{0.67}Fe_{1/2}Mn_{1/2}O_2$ is ~ 3 times greater than in O3-$Na_1Fe_{1/2}Mn_{1/2}O_2$, but O3 has an even lower activation energy.

A new uniaxial polarisation analysis technique, z^+ has been developed to perform full separation of nuclear, nuclear spin incoherent and magnetic neutron scattering components from polycrystalline scattering data. z^+ achieves this through measurements of spin-flip and non-spin-flip scattering along a single polarisation direction.

The technique is demonstrated on scattering from spin-ice $Ho_2Ti_2O_7$ using the LET spectrometer at the ISIS neutron facility. Cross-sections separated using z^+ are in good agreement with Monte Carlo simulations and previous results using *xyz* polarisation analysis.

Annem için

Acknowledgements

The wonderful and varied experiences I have had over the past four years are ones I will cherish for the rest of my life. I have had the opportunity to see so much more of this wonderful world, meet outstanding scientists from many backgrounds, and be a part of important work surrounded by highly passionate and experienced scientists. I cannot convey my endless gratitude to Jon Goff and David Voneshen for their excellent supervision, patience, and for giving me this opportunity.

The studies presented in this thesis would not have been possible without the expertise and endurance of Uthayakumar Sivaperumal, who has synthesised the numerous compounds under investigation. It has been such a pleasure working together, and I am very thankful for our conversations.

I am grateful to Dan G. Porter at Diamond Light Source for his help in analysing the x-ray diffraction data on $Na_xFe_{1/2}Mn_{1/2}O_2$. I consider myself very fortunate to have had the opportunity of meeting and working with Gøran J. Nilsen and Manh Duc Le from ISIS Neutron and Muon source. It was inspiring to work with such kind and passionate scientists.

The numerous ThALES experiments would not have been possible without the support of Martin Boehm and Paul Steffens, who have been extremely welcoming and helpful during my time at the ILL. I only wish I could spend more time with

them.

I thank all my officemates, both at RHUL and ISIS, for making this PhD so memorable. Giri, Saeed, Stef, Tim, Rupert - it was an absolute pleasure to get to know you and share an office with you all. We were not together for long, but the memories we made in that short time always bring me joy. I will always remember our short-lived film club. Simona^{n}, Sebastian and Benjamin - I would have been the most miserable person on RAL campus if it were not for you wonderful people! You have made my time in Oxfordshire so so enjoyable. It is with thanks to Simona^{n} that I explored and enjoyed so much of the beautiful Oxfordshire county. Special thanks to Benjamin for introducing me to Squash. I hope that some day we can Squash-Squash again as a trio. I thank you all for being such great people to spend time with, and wish you all the very best going forward.

Special thanks to Ian, Susan and Simon Brooks, who have wholeheartedly welcomed me into their family during my time at ISIS. It was absolutely wonderful to have such fantastic housemates, and I thoroughly enjoyed our time together. You have helped me in so many ways, and I cannot find the words to express my gratitude.

I owe my progress to my guardian angel, my mother. I would not be where I am without the endless sacrifices my family have made for me. I hope that I have made them proud!

Contents

List of Figures

List of Tables

Chapter 1

Introduction

1.1 Materials for energy applications

Recent climate reports consistently highlight the need for drastic changes in how the world's ever growing energy demands are met in order to avoid a climate crisis. To limit the global temperature rise to 1.5 °C above the pre-industrial average, 153 countries have now set emissions targets for the next decade to eventually reach net zero (planet-warming) emissions by the year 2050 [30]. Two crucial factor in meeting these targets will be transition to cleaner energy resources and more efficient energy consumption.

Thermoelectric devices offer one route towards better energy efficiency. These are highly versatile solid-state energy converters, with promising applications in waste heat recuperation and emission-free refrigeration [31, 32]. There is much interest in employing thermoelectric generators as waste heat recovery systems in combustion engine vehicles [33–38] and high-performance integrated circuits [39, 40], where the salvaged energy can be used to power other components or feed into the battery.

Thermoelectric generators can also be used to power small scale devices, such as wireless sensor networks [41, 42], health monitoring systems and wearable gadgets [43–47]. A comprehensive list of applications is provided by Jaziri *et al.* in Ref. [48].

A key limitation to device performance is the thermoelectric efficiency of the materials. The efficiency depends on competing physical parameters which must be optimised for thermoelectric materials to be effective. The material is required to be a good electrical conductor while also having a poor thermal conductivity, which has been a major material design challenge [31]. The Phonon-Liquid Electron-Crystal (PLEC) concept has recently attracted much attention as a route to designing highly efficient thermoelectrics with ultra-low thermal conductivity [49,50]. The validity of the PLEC concept in $AgCrSe_2$ is investigated in Chapter 3.

The shift away from fossil fuels has seen a significant increase in the use of renewable technologies such as wind, solar and tidal. One issue has been the intermittent supply of power, which is dependent on the weather. Hence, it is necessary to development low-cost, efficient energy storage solutions to improve the dependability of renewable power sources. Large-scale energy storage solutions are actively being explored, however many of the current technologies are in their infancy, with high capital costs and geographic requirements that render them impractical for widespread use [51].

Lithium-ion batteries have had great success in mobile applications owing to their unrivalled power and energy densities [52,53]. While the technology has reached maturity, the scarcity of Li mineral and issues surrounding supply from geographically challenging or politically sensitive areas has raised concerns over cost [54–57]. These issues are further enhanced by the rapid growth of battery electric vehicles, which are heavily reliant on Li-ion technology.

Natural abundance and low cost of sodium makes Na-ion batteries a particularly attractive alternative for large-scale static applications, such as load levelling for the grid [57, 58]. While Na-ion batteries may not achieve the energy density of their Li-ion counterparts, that does not pose an issue for static applications due to fewer constraints on weight and dimensions [59]. Furthermore, the transition to Na-ion will have a low initial cost since it is a drop-in replacement for Li-ion, thus allowing existing infrastructure to be used.

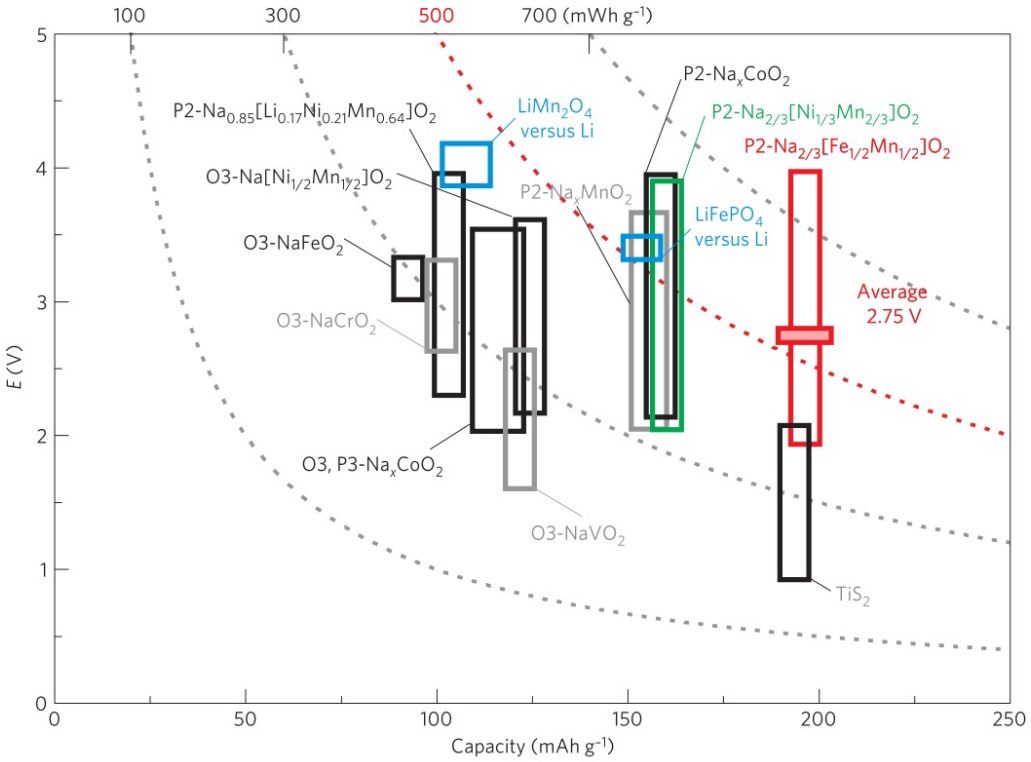

Figure 1.1: **Ranges of reversible capacity and operating voltage for Na-intercalation compounds**. $LiFePO_4$ and $LiMn_2O_4$ are shown for comparison. Image from Ref. [1].

One issue with Na-ion battery technology has been the low reversible capacity of Na insertion materials, typically limited to $100\,\mathrm{mAhg}^{-1}$. Figure 1.1 provides a comparison of the reversible capacity and operating voltage ranges for layered Na cathode

materials. P2-$Na_xFe_{1/2}Mn_{1/2}O_2$ delivers a reversible capacity of 190 $mAhg^{-1}$, reaching an estimated energy density of 520 $mWhg^{-1}$ at an operating voltage of 2.75 V. This is comparable to the energy density of commercially available Li-ion battery cathode $LiFePO_4$, and exceeds that of $LiMn_2O_4$ [1]. Therefore, $Na_xFe_{1/2}Mn_{1/2}O_2$ is an attractive replacement cathode material wholly comprised of naturally abundant elements without Co, Ni, Cu and Li. The role of diffusing ions in the performance of $Na_xFe_{1/2}Mn_{1/2}O_2$ is studied in Chapter 4.

1.2 Thermoelectricity

The thermoelectric (TE) effect is based on multiple thermodynamically reversible effects - the Seebeck effect, Peltier effect, and the Thomson effect. It offers a route to building devices capable of reversibly converting between a temperature differential and potential difference, as illustrated in Fig. 1.2. The direct production of a potential difference from a temperature gradient is known as the Seebeck effect, characterised by the Seebeck coefficient $S = -\Delta V/\Delta T$. Conversely, the Peltier effect refers to the process of establishing a thermal gradient by applying a potential difference across the junctions of a thermocouple [2, 32, 60, 61].

These effects can be understood in terms of charge carriers diffusing along a thermal gradient. Greater thermal energy of carriers in the hot region translates into higher kinetic energies which cause them to migrate from the hot to cold side. This leaves a higher concentration of charge at the cold side, thus establishing a potential difference. This idealised scenario neglects other effects such as thermal excitations and phonons which can reduce the TE effect. The next section discusses properties which determine the performance of thermoelectrics.

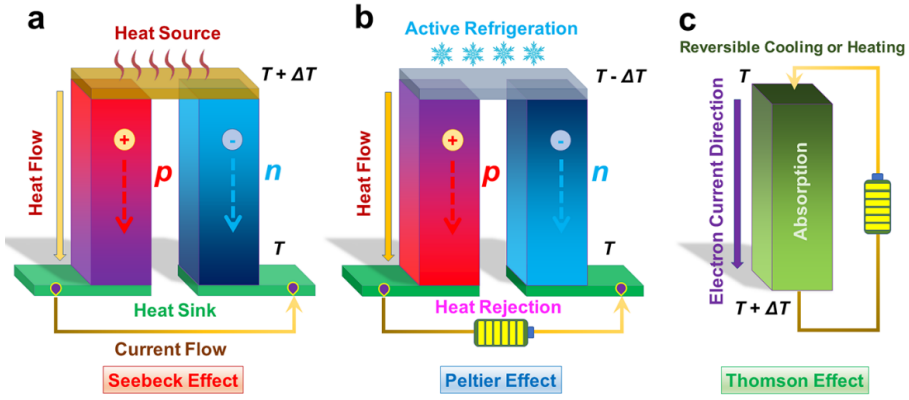

Figure 1.2: **Thermoelectric effects**. (a) Seebeck effect - electrical power is generated from a thermal gradient. (b) Peltier effect - cooling or heating achieved by applying a potential difference across the thermoelectric junction. (c) Thomson effect - reversible heating or cooling can occur when a temperature differential and an electric current coexist within a material. Image from Ref. [2].

1.2.1 Thermoelectric performance

The efficiency of a TE device is quantified through the dimensionless figure of merit, ZT defined as

$$ZT = \frac{S^2\sigma}{\kappa}T, \tag{1.1}$$

which is proportional to the electrical conductivity σ and inversely proportional to thermal conductivity κ [31]. For a TE generator, the maximum efficiency, η is characterised by ZT as

$$\eta = \eta_C \frac{\sqrt{1+ZT}-1}{\sqrt{1+ZT}+\frac{T_c}{T_h}}, \tag{1.2}$$

where T_c and T_h are the temperature of the cold and hot source, respectively, with an average temperature T across the device. The Carnot efficiency $\eta_C = \frac{\Delta T}{T_h}$ is the thermodynamic limit on the generator efficiency such that $\lim_{Z\to\infty}\eta = \eta_C$ [2,31,61].

For Peltier cooling, the maximum flux of heat that a TE material can pump is

given by

$$Q_{max} = \frac{1}{l}\left[\frac{\sigma S^2 T_c^2}{2} - \kappa \Delta T\right], \tag{1.3}$$

where l is the thickness of material [12], and the maximum attainable temperature drop is

$$\Delta T = z T_c \frac{T_c}{2}, \tag{1.4}$$

with zT denoting the figure of merit for the material rather than the device. The heat flux is maximised by maximising the power factor $S^2\sigma$ and minimising κ [31,61].

1.2.2 Improving performance

Realising highly efficient thermoelectric devices is challenging due to the conflicting characteristics that are required. The ideal material is one which simultaneously possesses a large power factor, PF $= S^2\sigma$, and a small thermal conductivity [13, 32, 62, 63].

A highly explored strategy to improve thermoelectric efficiency is the suppression of κ. The total thermal conductivity is a sum of lattice (κ_L) and carrier (κ_e) thermal conductivities,

$$\kappa = \kappa_e + \kappa_L. \tag{1.5}$$

The lattice thermal conductivity is typically mediated by the phonons propagating through the lattice. However, not all materials with a low κ are suitable for use in thermoelectric devices. In glasses, the thermal transport is mediated by a random walk process as opposed to the much faster phonons. Hence, glasses have a very low κ_L, but this is accompanied by lower charge mobilities resulting from lack of a crystalline environment. Therefore, a good thermoelectric material provides a crystalline

environment for electrical conduction while also disrupting phonon propagation to reduce thermal transport [2, 31].

The Wiedemann–Franz law relates κ_e and σ via the Lorenz factor L as

$$\kappa_e = \sigma L T. \tag{1.6}$$

For metals, this suggests that a poor thermal conductor is also a poor electrical conductor, because both are mediated by the electrons. In contrast, the dominant mechanism of thermal transport in semiconductors is via the lattice. In principle, this provides a route to optimising κ without impacting σ. Semiconductors also offer a relatively large Seebeck coefficient with good electrical conductivity, thus making them an ideal thermoelectric candidate [31, 64].

Glass-like values for κ_L have been realised through efforts such as nanostructuring [65–68], reduced phonon velocities [69], anharmonicity resulting from lattice or electronic instabilities [70, 71], and most recently the phonon-liquid electron-crystal (PLEC) model [16, 49, 72]. The PLEC model is examined Chapter 3. It relies on the suppression of κ_L in superionic conductors, such as Cu_2X (X = Te, Se, S) and $MCrY$ (M= Cu, Ag; Y= Se, S) [13,14,18,49,73–76], where long-ranged ionic diffusion is hosted on one sub-lattice with diffusivity comparable to those found in liquid salts [77, 78], while another sub-lattice provides crystalline order necessary for good electrical conductivity.

The next section examines the diffusion of ions in crystalline materials.

1.3 Diffusion

Solid state diffusion is concerned with the net transport of ions through stochastic movements, known as *jumps*, between sites within crystalline material. Each site is a potential energy well that is isolated from neighbouring sites by a potential barrier, known as the activation energy. The ions will have an energy distribution that is influenced by the temperature of the system. A jump to a neighbouring site becomes possible when an ion gains sufficient thermal energy to overcome the activation energy.

The activation energy for a particular diffusion mechanism depends on the local environment of the ions. This is influenced by several aspects of the crystal structure, such as the packing of atoms, effect of lattice defects and the presence of natural diffusion pathways. The layered structure of $Na_xFe_{1/2}Mn_{1/2}O_2$ has weak bonding between the layers, which acts to confine the movement of Na ions within the layer. Chapter 4 explores the influence of changes in the neighbouring planes on the diffusion of ions.

Ions may diffuse between regular sites via an interstitial site, or jump directly between neighbouring sites. For structures in which the interstitial and regular sites are in close vicinity, the occupation of the interstitial sites will be energetically unfavourable. Hence, diffusion is only observed once vacancies of the diffusing species are introduced at regular sites, otherwise the ions do not have any available sites to occupy other than the current one. This is discussed further in Section 1.3.3 and Ref. [3].

1.3.1 Stochastic diffusion

A diffusion process is a stochastic one if its evolution with time has an associated probability distribution. For solid state diffusion, the probability is dependent on the set of all possible states. Here, the probability of a single event taking the system into state a_1 at a time t_1 will be denoted by $P_1(a_1, t_1)$. Then the joint probability for any sequence of states is denoted by $P_n(a_1, t_1; ...; a_n, t_n)$, where $a_1, a_2, a_3, ...$ happen in succession at time $t_1, t_2, t_3, ...$, respectively [12, 79].

The stochastic process considered here is Markovian and has the Markov property that the probability of the next state is independent of all previous states, and only depends on the current state of the system. Then the probability of the system occupying any sequence of states can be written as

$$P_n(a_1, t_1; ...; a_n, t_n) = P_1(a_1, t_1) \times \prod_{n=2}^{n} P(a_n, t_n | a_{n-1}, t_{n-1}), \tag{1.7}$$

where $P(a_n, t_n|a_{n-1}, t_{n-1})$ is the conditional probability of occupying state a_n at time t_n given that the system is initially in state a_{n-1} at time t_{n-1}. The pathway between initial and final states is not unique, hence the conditional probability must satisfy the Chapman–Kolmogorov equation

$$P(a_f, t_f|a_i, t_i) = \sum_j P(a_f, t_f|a_j, t_j)P(a_j, t_j|a_i, t_i), \tag{1.8}$$

where index j refers to the intermediate steps between initial i and final state f such that $t_f > t_j > t_i$ [80]. By imposing the Markov property, the probability of an ion occupying a particular site at a later time depends only on the probability of it occupying an intermediate site at the start and the probability of a transition from

the intermediate to final site, which can be mathematically expressed as

$$P_1(a_f, t_f) = \sum_j P(a_f, t_f | a_j, t_j) P_1(a_j, t_j). \tag{1.9}$$

The jump rate between nearest-neighbour sites is obtained by taking the time derivative as,

$$\begin{aligned} \frac{dP_1(a,t)}{dt} &= \sum_j \dot{p}(a_j; a) P_1(a_j, t) \\ &= \sum_{a_j \neq a} \Gamma_{a_j a} P(a_j, t) - \Gamma_{a a_j} P(a, t), \end{aligned} \tag{1.10}$$

where $\Gamma_{\alpha\beta} = \dot{p}(\alpha, \beta)$ is the transition rate from state α into a state β. For jump diffusion of ions, the transition rate is governed by the principle of detailed balance. Hence, this equation inherently accounts for differences in the energy of sites in the forward and backward directions [12, 79, 80].

1.3.2 Diffusion rates

The jump rate Γ for a stochastic process provides a route to calculating the diffusion rate of ions. It can be assumed that jumps between neighbouring sites arise only from thermally activated processes when the mass of the diffusing species is sufficiently large, as is the case for Na ions. Using statistical mechanics, Eyring formulated a general expression for the reaction rate Γ of processes with an associated activation energy E_a as

$$\Gamma = \frac{k_\mathrm{B} T}{h} \frac{Z'}{Z} \exp\left(-\frac{E_0}{k_\mathrm{B} T}\right), \tag{1.11}$$

where k_B and h are the Boltzmann and Planck constants, respectively, T is the temperature, and E_0 is E_a at $T = 0\,\mathrm{K}$. Here, Z and Z' are the partition functions of the initial and activated states, respectively [81, 82].

In the initial state, ions with insufficient thermal energy to overcome to potential barrier oscillate in the direction of the neighbouring site with a frequency ν_0. The partition functions can be expressed in terms of ν_0 such that the jump rate Γ from Eq. (1.11) becomes

$$\Gamma = \frac{k_\mathrm{B}T}{h}\left(1 - \exp\left(-\frac{h\nu_0}{k_\mathrm{B}T}\right)\right)\exp\left(-\frac{E_0}{k_\mathrm{B}T}\right). \tag{1.12}$$

In the limit of low attempt frequency, i.e. $h\nu_0 \ll k_\mathrm{B}T$, this can be written as

$$\Gamma = \nu_0 \exp\left(-\frac{E_a}{k_\mathrm{B}T}\right), \tag{1.13}$$

where ν_0 has the same units as Γ and is therefore equivalent to a jump rate constant Γ_0 [82]. This form of the jump rate shows that the diffusion is governed by the Arrhenius law.

The mean residence time, τ that an ion spends on a site before another jump is inversely related to the jump rate, and expressed as

$$\tau = \tau_0 \exp\left(\frac{E_a}{k_\mathrm{B}T}\right). \tag{1.14}$$

Variations in τ arise from differences in the local environment of ions, which leads to variations in E_a. This is influenced by factors such as the arrangement of nearest-neighbours and the existence of energetically inequivalent sites. The microscopic property τ relates to the macroscopic diffusion coefficient via the Einstein-

Smoluchowski equation

$$D = \frac{l^2}{2n\tau}, \tag{1.15}$$

where l is the average jump length, and n denotes the dimensionality of the diffusion process [83]. In crystalline systems, l corresponds to the separation of available sites.

1.3.3 Diffusion mechanisms

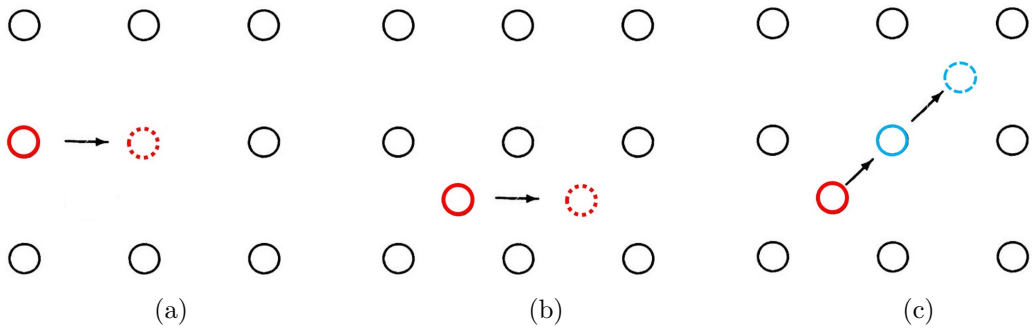

Figure 1.3: **Mechanisms of diffusion**. (a) Vacancy mechanism - the red ion (solid outline) on a regular site jumps to occupy a neighbouring vacant site (broken outline). (b) Interstitial mechanism - the red ion on an interstitial site jumps to a neighbouring interstitial site. (c) Interstitialcy mechanism - An ion on a regular site (solid blue outline) is displaced to an interstitial site (broken blue outline) by an ion previously on an interstitial site (solid red outline). Figures adapted from Ref. [3].

Ionic diffusion in crystalline materials can occur through a range of mechanisms, as outlined in Ref. [3]. The vacancy mechanism is often the dominant mechanism in most materials. Here, an ion occupying a regular site jumps to a neighbouring vacant site, see Fig. 1.3a. For systems in which the ion concentration is high, self-diffusion of a vacancy is likely to be far greater than the self-diffusion of single ions, because there is a higher probability that neighbouring regular sites will be blocked by other ions.

The interstitial mechanism occurs entirely on a secondary lattice and does not involve the regular lattice. An ion occupying an interstitial site around the regular lattice can jump directly to a neighbouring interstitial site, as illustrated in Fig. 1.3b. Generally, the secondary lattice has a high concentration of holes, hence the probability of encountering site blocking in low. This is reflected in the high diffusion rates and low activation energies of ions that migrate through this mechanism.

A more complex example is the interstitialcy mechanism, where an ion on a interstitial site displaces a neighbouring ion on a regular site to a new interstitial site, as depicted in Fig. 1.3c. For this mechanism, the contribution of interstitial sites to the diffusion is typically negligible due to the high energy cost of forming interstitials.

1.4 Separation of contributions to neutron scattering

Neutron scattering is a probe of a broad range of microscopic material properties. The total neutron scattering intensity is comprised of three contributions - nuclear, magnetic and nuclear spin incoherent scattering. The technique of inelastic neutron scattering provides rich information about lattice dynamics, such as phonon excitations from solids with long-range crystalline order. Quasi-elastic neutron scattering (QENS) is used to probe the dynamics of deviations from long-range order. It can arise from a range of phenomena including the diffusion of ions, and the presence of dynamic defects and vacancies. Many energy materials, such as those being investigated in this thesis, contain magnetic species which can also give rise to both

inelastic and quasi-elastic scattering [84].

Complications can arise when two or more sources of scattering coexist, as is often the case. Ionic diffusion is a slow dynamic process that presents weakly in nuclear spin incoherent QENS. It can be obscured by diffuse nuclear and magnetic scattering, as well as thermal diffuse scattering due to phonons. Similarly, phonons and magnons can have similar energy scales and coexist in the same region of Q-space. It is therefore necessary to isolate the different scattering contributions in order to quantitatively analyse the different properties.

There are various methods of isolating the different sources of scattering based on their energy and Q dependence. The magnetic form factor for neutron scattering leads to a significant drop-off in magnetic intensity with increasing Q. Magnetic scattering also becomes broader until the temperature exceeds the ordering temperature of the sample, at which point it becomes diffuse. In contrast, the phonon intensity increases with temperature and scales as Q^2.

Diffuse scattering is usually quasi-elastic and, therefore, it occurs at low energies. Away from Bragg points, it is often possible to use energy analysis to separate it from phonons and magnons which occur at higher energies. However, while it provides qualitative insights, this method of distinguishing the signals does not permit a quantitative treatment of the scattering.

High quality data necessary for a quantitative treatment can be obtained from polarised neutron scattering. The technique of uniaxial polarisation analysis (z) was first demonstrated in 1968 by Moon, Riste and Koehler [85]. By adding a neutron spin dimension to the scattering measurement and analysing the polarisation of the beam with respect to a magnetic field parallel to z-axis, it is possible to isolate the nuclear component to scattering. However, this technique is unable to separate the

magnetic and nuclear spin incoherent contributions.

A generalisation of the uniaxial method was first developed in 1993 by Schärpf and Capellmann [86]. The *xyz* technique involves analysis of the neutron polarisation along three orthogonal directions to provide a complete and unambiguous separation of the nuclear, magnetic and nuclear spin incoherent scattering components. This technique is employed in Chapters 3 and 4 to quantitatively analyse the diffusion of ions via nuclear spin incoherent QENS.

A new polarisation analysis technique, z^+ is introduced in Chapter 5. This novel method, suitable for scattering from polycrystalline samples, provides a full separation of the scattering components using uniaxial polarisation analysis and an instrument with significant out-of-plane coverage. It achieves this by taking advantage of the variation of magnetic intensity around the Debye-Scherrer cone.

Chapter 2

Experimental Techniques

2.1 The crystal structure

2.1.1 The crystal lattice

A crystal lattice is the convolution of lattice points with a basis of atoms, as illustrated in Fig. 2.1. The lattice points form an infinitely repeating pattern of points described by a set of 3 linearly independent basis vectors $(\vec{a}, \vec{b}, \vec{c})$. Then the lattice vector, which joins any two points on the lattice, is given by a linear combination of the basis vectors as

$$\vec{R} = u\vec{a} + v\vec{b} + w\vec{c}, \tag{2.1}$$

where u, v and w are a set of integer values. The volume of space defined by the basis vectors is called a *unit cell* and it contains a small arrangement of atoms know as the *basis*. A single crystal structure is comprised of many identical unit cells stacked together along all three dimensions of space. The position of an atom j within a unit cell is defined with respect to the arbitrary origin of the unit cell in terms of

the basis vectors as

$$\vec{r}_j = u_j\vec{a} + v_j\vec{b} + w_j\vec{c}, \tag{2.2}$$

where u_j, v_j and w_j are the fractional coordinates with values in the range ± 1 [4,87]. Then the position of atom j in any unit cell is given by $R + r_j$.

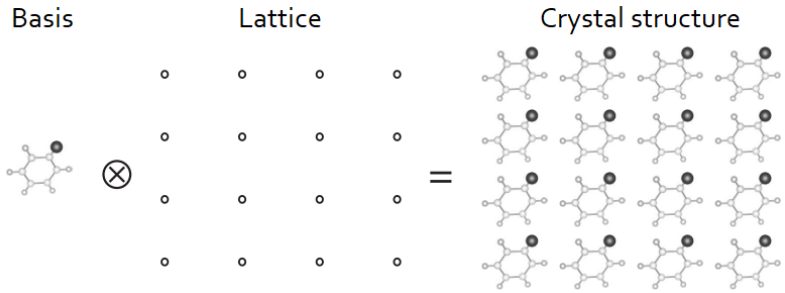

Figure 2.1: **Formation of a crystal structure**. The crystal structure is obtained by placing a basis of atoms on each lattice point. Image from Ref. [4].

2.1.2 The reciprocal lattice

Scattering experiments investigate the structure of a material in the reciprocal space, thereby giving information about the reciprocal lattice of the material. The reciprocal lattice is described by the reciprocal lattice vector

$$\vec{G} = h\vec{a}^* + k\vec{b}^* + l\vec{c}^*, \tag{2.3}$$

which has the periodicity of the lattice in direct space, and mathematically relates to it via the transformation of basis vectors

$$\vec{a}^* = \frac{2\pi \cdot (\vec{b} \times \vec{c})}{\vec{a} \cdot (\vec{b} \times \vec{c})} \qquad \vec{b}^* = \frac{2\pi \cdot (\vec{c} \times \vec{a})}{\vec{a} \cdot (\vec{b} \times \vec{c})} \qquad \vec{c}^* = \frac{2\pi \cdot (\vec{a} \times \vec{b})}{\vec{a} \cdot (\vec{b} \times \vec{c})}, \tag{2.4}$$

such that $e^{i\vec{G}\cdot\vec{R}} = 1$ for all points $\vec{R}$ of the lattice in direct space. The integer values h, k and l are known as Miller indices, which are often used to specify positions or families of (hkl) planes in the reciprocal space. Every valid reciprocal lattice vector $\vec{G}_{hkl}$ is normal to a family of planes with a planar separation [87]

$$d_{hkl} = 2\pi/|\vec{G}_{hkl}|. \tag{2.5}$$

2.1.3 Superlattices

The periodicity of a crystal structure may be broken if it exhibit lattice sites with missing atoms - referred to as *vacancies*. In materials that host many such vacancies, the interactions between vacancies can give rise to a long-range-ordered pattern with a new periodicity. When this is the case, the resulting superstructure can be treated in very much the same way as the underlying crystal structure defined above. The superstructure will occupy a lattice known as the superlattice, and have a basis of atoms comprised of an integer number of unit cells that make up a *supercell*. The supercell vectors are given by an integer sum of unit cell vectors as

$$\begin{aligned} \vec{a}' &= n_1\vec{a} + m_1\vec{b} + p_1\vec{c} \\ \vec{b}' &= n_2\vec{a} + m_2\vec{b} + p_2\vec{c} \\ \vec{c}' &= n_3\vec{a} + m_3\vec{b} + p_3\vec{c}. \end{aligned} \tag{2.6}$$

Then the superlattice vector between two superlattice points is defined as

$$\vec{R}' = u\vec{a}' + v\vec{b}' + w\vec{c}'. \tag{2.7}$$

A diffraction experiment will observe two components, one due to scattering from the underlying unit cell and another from the supercell. The larger volume of the superlattice in direct space leads to Bragg reflections that are much closer together in reciprocal space. Bragg reflections from the superstructure present as satellite reflections around principal Bragg reflections from the unit cell, and are indexed by the reciprocal superlattice [88]. The ordering of the atoms in a superstructure can be inferred from the intensities and systematic absences of superlattice reflections. This technique is employed in Section 4.3.1 to investigate the formation of superstructures in $Na_xFe_{1/2}Mn_{1/2}O_2$.

2.2 Elastic scattering

The scattering of radiation, such as X-ray photons or neutrons, from a crystalline material is characterised by the exchange of momentum and energy E between the two systems. An elastic scattering event is one for which the energy transfer of the radiation,

$$\Delta E = \hbar\omega = E_i - E_f \tag{2.8}$$

is zero. The energy of a X-ray photon can be expressed in terms of the wavevector k as $E = \hbar c|\vec{k}|$, where c is the speed of light. Likewise, the kinetic energy of a non-relativistic neutron of mass m_{n} is $E = \hbar|\vec{k}|^2/2m_n$.

Using wave-particle duality of nature, the momentum transfer during a scattering event is given by

$$\hbar(\vec{k}_i - \vec{k}_f) = \hbar\vec{Q}, \tag{2.9}$$

where $\vec{k}_i$ and $\vec{k}_f$ are the initial and final wavevector of the scattered radiation, and

$$\vec{Q} = \vec{k}_i - \vec{k}_f \tag{2.10}$$

is known as the momentum transfer vector [5, 6].

2.2.1 Scattering from an atom

A key step in understanding the structure of materials through scattering experiments is to form the link between the measured deflections and the atomic structure. The simplest case to consider is the elastic scattering of radiation from a single fixed atom, as illustrated in Fig. 2.2. A steady stream of monochromatic particles with wavelength λ travelling in the x direction can be described by the complex plane wave

$$\psi_i = \psi_0 \exp\Big(i|\vec{k}_i||\vec{x}|\Big), \tag{2.11}$$

where $\vec{k}_i$ is the wavevector (of magnitude $|\vec{k}_i| = 2\pi/\lambda$) in the direction of propagation. The flux incident on the atom is given by $\Phi = v_i|\psi_i|^2 = v_i|\psi_0|^2$, where v_i is the incident neutron velocity.

After interacting with the atom at the origin, the waves are scattered radially outwards with a wavevector $\vec{k}_f$ parallel to a displacement vector $\vec{r}$. The scattered waves take the form

$$\psi_f = \psi_0 f(\lambda, \theta) \frac{\exp\Big(i|\vec{k}_f||\vec{r}|\Big)}{r}, \tag{2.12}$$

where θ is half of the scattering angle 2θ between $\vec{r}$ and $\vec{x}$, and $f(\lambda, \theta)$ is the scattering form factor which gives the probability that a particle is scattered in a particular direction [5, 6].

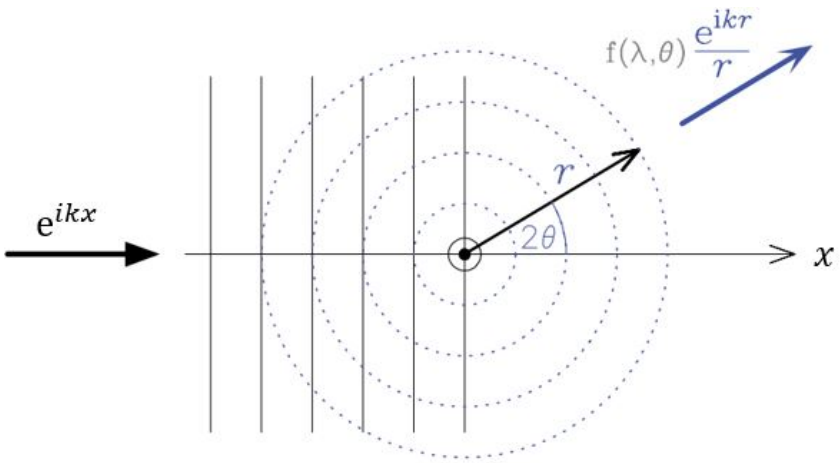

Figure 2.2: **The geometry of scattering from a single atom in 2D**. A collimated plane wave incident on an atom at the origin produces a spherical scattered wave. Image from Ref. [5].

2.2.2 Angular dependence of scattered intensity

Scattering can arise from interactions with any part of the atom, and the form of $f(\lambda, \theta)$ varies significantly depending on the values of λ and θ. When λ is comparable to the size of the atom, $f(\lambda, \theta)$ becomes a function of $\sin(\theta)/\lambda$. Therefore, there is no influence on the scattered intensity when θ is small since all possible path lengths from the atom to $\vec{r}$ will be comparable. However, as θ increases so does the path length difference between scattering from different parts of the atom, giving rise to interference effects. $f(\lambda, \theta)$ becomes independent of θ when λ is much greater than the length scale of the scatterer [5].

2.2.3 Scattering from a collection of atoms

By considering the scattering from an arbitrary distribution of fixed atoms, it is possible to calculate the count rate at the detector during a diffraction experiment. This model of a crystalline sample is a generalisation of the model from Section 2.2.1.

Once again, a complex plane wave with $\vec{k}_i \parallel \hat{x}$ is incident on the sample, but now scatters from an atom j located at position $\vec{R}_j$ with respect to an arbitrary origin in the sample. The wave function of the scattered radiation is

$$\psi_{f,j} = \psi_0 \exp\left(i\vec{k}_i \cdot \vec{R}_j\right) f_j(\lambda,\theta) \frac{\exp\left(i\vec{k}_f \cdot (\vec{r} - \vec{R}_j)\right)}{|\vec{r} - \vec{R}_j|}. \tag{2.13}$$

Here, $\vec{r}$ is the position vector of the detector relative to the origin, therefore $|\vec{r} - \vec{R}_j|$ is the distance from the j^{th} atom to the detector. The details of the interaction between the incident wave and the j^{th} atom is given by $f_j(\lambda,\theta)$. Then the total scattered wave amplitude at the detector position is obtained by summing the contributions from each of the N atoms making up the sample as

$$\psi_f = \psi_0 \exp\left(i\vec{k}_f \cdot \vec{r}\right) \sum_{j=1}^{N} f_j(\lambda,\theta) \frac{\exp\left(i\vec{Q} \cdot \vec{R}_j\right)}{|\vec{r} - \vec{R}_j|}. \tag{2.14}$$

This general result assumes a sufficiently weak scattering process such that the scattered wavelets do not interfere with the incident waves. This assumption, known as the Born approximation, is generally valid both for neutrons and X-rays. However, multiple scattering and absorption can become important considerations for large samples.

In practice, the detector is located a relatively large distance from the sample, therefore $|\vec{R}_j| \ll |\vec{r}|$ and $|\vec{r} - \vec{R}_j| \approx r$. Then, using the result $\left|\exp\left(i\vec{k}_f \cdot \vec{r}\right)\right|^2 = 1$,

the intensity at the detector position is given by

$$\begin{aligned} I(\vec{Q}) &= |\psi_f|^2 \\ &= \frac{\Phi}{r^2} \left| \sum_{j=1}^{N} f_j(\lambda, \theta) \exp\Big(i\vec{Q} \cdot \vec{R}_j\Big) \right|^2 . \end{aligned} \tag{2.15}$$

This result shows that the scattering intensity is not a function of the neutron state before or after scattering, rather it is a function of the momentum transferred to the sample [5, 6].

2.2.4 Scattering from a crystal

A crystal structure may comprise somewhere in the region of 10^{23} atoms, which makes the previous calculation of intensity a highly intensive one. This task can be greatly simplified by recalling, from Section 2.1, the highly periodic structure of crystalline materials. This allows the intensity to be expressed in terms of two sums, one over all n atoms in the unit cell and the second over all N_{cells} unit cells in the structure such that

$$|\psi_f|^2 = \frac{\Phi}{r^2} \left| \sum_{m=1}^{N_{\text{cells}}} \sum_{j=1}^{n} f_j(\lambda, \theta) \exp\Big(i\vec{Q} \cdot (\vec{R}_m + \vec{r}_j)\Big) \right|^2 , \tag{2.16}$$

where the position of the j^{th} atom within the m^{th} unit cell is given by $\vec{R}_m + \vec{r}_j$. Using the result

$$\left| \sum_{m=1}^{N_{\text{cells}}} \exp\Big(i\vec{Q} \cdot \vec{R}_m\Big) \right|^2 = N_{\text{cells}}^2, \tag{2.17}$$

the above summation can instead be performed only over the atoms within the unit cell since the unit cell contains all necessary information to build the whole structure.

Hence, the detected scattering intensity from a crystalline material is described by

$$\begin{aligned} |\psi_f|^2 &= \frac{\Phi N_{\text{cells}}^2}{r^2} \left| \sum_{j=1}^{n} f_j(\lambda, \theta) \exp\left(i\vec{Q} \cdot \vec{r}_j\right) \right|^2 \\ &= \frac{\Phi N_{\text{cells}}^2}{r^2} \left| \sum_{j=1}^{n} f_j(\lambda, \theta) \exp\left(2\pi i(hu_j + kv_j + lw_j)\right) \right|^2 . \end{aligned} \tag{2.18}$$

This results shows that $(hu_j + kv_j + lw_j)$ must be an integer for constructive interference to occur [4].

2.3 Scattering cross-sections

Scattering experiments are able to perform a variety of measurements on the scattered radiation, which in turn provides information about different aspects of the scattering system. The granularity of the information can be expressed in terms of the scattering *cross-section* of the sample. Defined below are the various scattering cross-sections corresponding to different types of measurements. These definitions and further discussions of the cross-sections are provided in Refs. [5, 89] and [6].

The work in this thesis utilises neutron scattering to probe the dynamic behaviour of crystalline material, with X-ray scattering being used to gain complementary understanding of the crystal structures. Henceforth, the discussions in this chapter will place greater emphasis on neutron scattering, with a brief comparison to X-rays provided in Section 2.9.1.

2.3.1 Total scattering cross-section

The overall number of scattering events that occurs when a stream of radiation is incident on a sample is called the *total scattering cross-section* of the sample, defined as

$$\sigma_{\text{tot}} = \frac{R}{\Phi}, \tag{2.19}$$

where R is the scattering rate summed over all directions, and Φ is the incident flux of neutrons. To relate this back to the discussion of elastic scattering from a single fixed atom, σ_{tot} can be calculated from Eq. (2.12), the wave function of the scattered beam. The scattered intensity is given by $v_f|\psi_f|^2 = v_f\psi_f\psi_f^*$, and R is calculated as

$$\begin{aligned} R &= \int_{2\theta=0}^{\pi}\int_{\phi=0}^{2\pi} v_f|\psi_f|^2 dA \\ &= \int_{2\theta=0}^{\pi}\int_{\phi=0}^{2\pi} \frac{\Phi|f(\lambda,\theta)|^2}{r^2} \times r^2\sin(2\theta)d\phi d2\theta \\ &= 2\pi\int_{2\theta=0}^{\pi} \Phi|f(\lambda,\theta)|^2\sin(2\theta)d2\theta \\ &= 4\pi\Phi|f(\lambda,\theta)|^2, \end{aligned} \tag{2.20}$$

where v_f is the scattered neutron velocity and $dA = r^2\sin(2\theta)d\phi d2\theta$. For neutron scattering, the form factor $f(\lambda,\theta)$ is the *nuclear scattering length* b, which is independent of λ and θ. Then the total scattering cross section is given by

$$\sigma_{\text{tot}} = 4\pi|b|^2. \tag{2.21}$$

2.3.2 Differential scattering cross-section

In practice, the detector is positioned a large distance from the sample and subtends a small solid angle $d\Omega = dA/r^2$ at the sample position defined by the polar coordinates 2θ and ϕ shown in Fig. 2.3. Therefore, only the portion of incident radiation scattered into $d\Omega$ are counted by the detector. This quantity is called the *differential scattering cross-section*, defined as

$$\frac{d\sigma}{d\Omega} = \frac{R(2\theta, \phi)}{\Phi \times d\Omega}, \tag{2.22}$$

where $R(2\theta, \phi)$ is the rate of scattering into $d\Omega$. The equality in Eq. (2.22) is only valid in the limit of $d\Omega \to 0$, which corresponds to a small area of detector coverage over which the scattered intensity remains constant. It follow from Eqs. (2.18) and (2.20) that for a system comprised of many nuclei

$$\frac{d\sigma}{d\Omega} = \left| \sum_{j=1} f_j(\lambda, \theta) \exp\left(i\vec{Q} \cdot \vec{R}_j\right) \right|^2 . \tag{2.23}$$

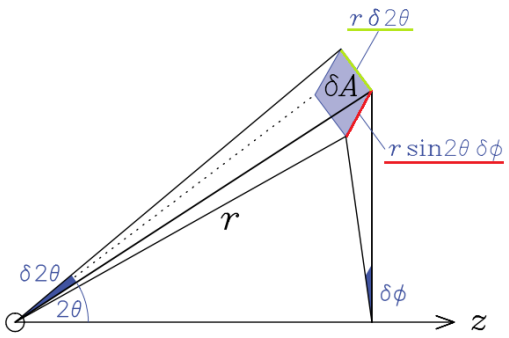

Figure 2.3: **Geometry of scattering experiments**. Image adapted from Ref. [5].

The transition rate $R(2\theta, \phi)$ from the initial to final state is determined using

Fermi's Golden Rule (see Ref. [6]). The resulting differential cross-section for neutron scattering has the form

$$\frac{d\sigma}{d\Omega} = \frac{k_f}{k_i}\left(\frac{m_{\mathrm{n}}}{2\pi\hbar^2}\right)^2 |\,\langle k_f\eta_f|\,V(\vec{Q})\,|k_i\eta_i\rangle\,|^2, \tag{2.24}$$

where $V(\vec{Q})$ is the Fourier transform of the interaction potential $V(\vec{r})$ the radiation experiences due to the atoms. The Dirac notation for the inner product $\langle f|\,V\,|i\rangle = \int \Psi_f^* V \Psi_i d\tau$, with Ψ_i and Ψ_f representing the initial and final states of the combined system of the radiation and scatterer, and $d\tau$ represents the volume for all integration variables [6]. The differential scattering cross-section provides details of spatial correlations within the sample, however temporal correlations continue to be averaged in experiments which measure $d\sigma/d\Omega$.

2.3.3 Partial differential cross-section

The differential scattering cross-section can be generalised further by analysing the energies of scattered neutrons, which enables temporal correlations to be probed via quasi-elastic and inelastic scattering. The *partial differential cross-section* measures the rate at which incident neutrons are scattered into $d\Omega$ with E_f between E and $E + dE$, expressed mathematically as

$$\frac{\partial^2\sigma}{\partial\Omega\partial E} = \frac{R(2\theta,\phi,E)}{\Phi d\Omega dE}. \tag{2.25}$$

Considerations of energy during a scattering event requires the initial and final state of the scattering system to also be considered in order to ensure conservation of energy. Hence, any transition of neutrons from a state $\vec{k_i}$ with E_i to a state k_f

with E_f is accompanied by a transition from state λ_i to λ_f for the scattering system. The master equation for the partial differential neutron scattering cross-section is

$$\frac{\partial^2\sigma}{\partial\Omega\partial E} = \frac{k_f}{k_i}\left(\frac{m_\mathrm{n}}{2\pi\hbar^2}\right)^2 \sum_{\eta_i} p_{\eta_i} \sum_{\eta_f} |\left\langle k_f\eta_f\right| V(\vec{Q}) \left|k_i\eta_i\right\rangle|^2 \delta(E_{\eta_f} - E_{\eta_i} + E_f - E_i). \quad (2.26)$$

Here, the sum is weighted by the probability of the scattering system being in the initial state $|\eta_i\rangle$, p_{η_i} to account for the possibility of multiple transitions which can take the neutrons from $\vec{k}_i$ to $\vec{k}_f$. E_{η_i} and E_{η_f} are the initial and final energies of the scattering system, and the delta function ensures conservation of energy [5, 6].

2.4 Neutron scattering

Neutrons are an ideal probe of structural and magnetic characteristics in matter. A lack of charge means that neutrons can penetrate deep into a sample and scatter directly from the nuclei via the short-ranged strong nuclear force. Additionally, the magnetic moment of neutrons can interact with the magnetic moment of atoms that have unfilled electron shells. This long-range dipole-dipole interaction offers a powerful method of studying the magnetic properties of a material.

The comparable rates of nuclear and magnetic scattering make neutrons well suited to the study of magnetic systems [5]. However, a significant drawback of neutron scattering is the difficulty of generating neutrons, which make this a highly flux-limited technique that necessitates very long counting times to produce reliable statistics.

2.4.1 Nuclear scattering

For nuclear scattering, the cross-sections introduced in Section 2.3 can be decomposed into a sum of coherent and incoherent components as

$$\sigma_{\text{tot}} = \sigma_{\text{coh}} + \sigma_{\text{incoh}}. \tag{2.27}$$

Each component contains information about different properties of the scattering system. Coherent scattering arises from the collective behaviour of atoms, such as the crystal structure and lattice vibrations. In contrast, incoherent scattering provides information about the random distribution of deviations from the average structure, such as local excitations, molecular vibrations and diffusion [89].

Expressions for coherent and incoherent scattering from a primitive unit cell can be obtained from Eq. (2.23), which may be written as

$$\frac{d\sigma}{d\Omega} = \sum_{j,m} \overline{b_j b_m} \exp\Big(i\vec{Q} \cdot (\vec{R}_j - \vec{R}_m)\Big), \tag{2.28}$$

where for a system of N uncorrelated nuclei

$$\overline{b_j b_m} = \begin{cases} \overline{b^2} & \text{for } j = m \\ \overline{b}^2 & \text{otherwise.} \end{cases} \tag{2.29}$$

Here, $\vec{R}_j$ is the lattice position of atom j, and $\overline{b}$ and $\overline{b^2}$ are the averages of b and b^2, respectively. Then, for a monatomic system, the coherent and incoherent differential

cross-sections are expressed as

$$\begin{aligned}\frac{d\sigma}{d\Omega}_{\text{coh}} &= \overline{b}^2 \left| \sum_j \exp\left(i\vec{Q}\cdot\vec{R}_j\right) \right|^2 \\ &= \overline{b}^2 \frac{N(2\pi)^3}{v_0} \sum_{\vec{G}} \delta(\vec{Q}-\vec{G})\end{aligned} \tag{2.30}$$

and

$$\frac{d\sigma}{d\Omega}_{\text{incoh}} = N(\overline{b^2} - \overline{b}^2), \tag{2.31}$$

where v_0 is the unit cell volume, N is the number of unit cells, and the Dirac delta function describes Bragg peaks which are observed when the Laue condition is satisfied [6, 89].

The coherent cross-section gives information about interference from different sites and will be weak for highly disordered systems due to lack of an average structure. Its dependence on the Laue condition makes elastic coherent scatter an ideal method of determining the lattice parameters of a crystalline system in real space, and studying the presence of superstructures.

Equation (2.31) shows the dependence of incoherent scattering on the difference between scattering lengths. The scattering length b varies depending on the atom, isotope and the nuclear spin state. Hence, for a system comprised of a single element, *isotope incoherent* and *nuclear spin incoherent* scattering can arise from the random distribution of isotopes and nuclear spins, respectively.

An equivalent decomposition of the partial differential cross-section has the fol-

lowing form:

$$\begin{aligned}\frac{\partial^2\sigma}{\partial\Omega\partial E} &= \frac{k_f}{k_i}\frac{1}{2\pi\hbar}\sum_{j,m}\overline{b_j b_m}\int\langle j,m\rangle\exp(-i\omega t)dt \\ &= \frac{k_f}{k_i}\frac{1}{2\pi\hbar}\bar{b}^2\sum_{j,m}\int\langle j,m\rangle\exp(-i\omega t)dt \\ &\quad + \frac{k_f}{k_i}\frac{1}{2\pi\hbar}\left(\overline{b^2}-\bar{b}^2\right)\sum_{j}\int\langle j,j\rangle\exp(-i\omega t)dt,\end{aligned} \tag{2.32}$$

where ω is the angular frequency, t is time and

$$\langle j,m\rangle = \langle\exp\Big(-i\vec{Q}\cdot\vec{R}_j(0)\Big)\exp\Big(i\vec{Q}\cdot\vec{R}_m(t)\Big)\rangle.$$

The first and seconds term in Eq. (2.32) are the coherent and incoherent cross-sections, respectively. It is clear that the coherent scattering provides information about the correlation between different atoms at different times, whereas the incoherent scattering probes the same atom at different times [6, 89].

2.4.2 Magnetic scattering

For magnetic scattering, the spin state of the neutron, σ (not to be confused with σ_{tot} for the total cross-section) must also be incorporated into the partial differential cross-section since the interaction depends on the orientation of σ. Then the master equation becomes

$$\frac{\partial^2\sigma}{\partial\Omega\partial E} = \frac{k_f}{k_i}\left(\frac{m}{2\pi\hbar^2}\right)^2\left|\left\langle\vec{k}_f\sigma_f\eta_f\right|V_m\left|\vec{k}_i\sigma_i\eta_i\right\rangle\right|^2\delta(E_{\eta_f}-E_{\eta_i}+E_f-E_i), \tag{2.33}$$

where σ_i and σ_f are the initial and final neutron spin states, and V_m is the magnetic potential. The interaction with the electrons has a contribution from the magnetic moment of the electron and the moment arising from the orbital motion of electrons. This is expressed by re-stating the partial differential cross-section as

$$\frac{\partial^2\sigma}{\partial\Omega\partial E} = (\gamma r_0)^2 \frac{k_f}{k_i} |\left\langle \sigma_f \eta_f \right| \boldsymbol{\sigma} \cdot \boldsymbol{M}_\perp(\vec{Q}) \left| \sigma_i \eta_i \right\rangle|^2 \delta(E_{\eta_f} - E_{\eta_i} + E_f - E_i), \tag{2.34}$$

where $\gamma = 1.913$ and r_0 is the classical radius of an electron. The Pauli spin operator $\boldsymbol{\sigma}$ relates to the neutron spin operator $\boldsymbol{S}$ through $\boldsymbol{\sigma} = 2\boldsymbol{S}/\hbar$. $\boldsymbol{M}(\vec{Q})$ is the spatial Fourier transform of $\boldsymbol{M}(\vec{R})$, which is the operator for the magnetisation of the scatterer at lattice position $\vec{R}$. It is important to note that neutron scattering only probes the component of magnetisation perpendicular to $\vec{Q}$. Then $\boldsymbol{M}_\perp(\vec{Q})$ is the component of $\boldsymbol{M}(\vec{Q})$ perpendicular to $\vec{Q}$, defined as

$$\boldsymbol{M}_\perp(\vec{Q}) = \sum_j \exp\Big(i\vec{Q}\cdot\vec{r}_j\Big) \left[\hat{Q} \times \left(\vec{s}_j \times \hat{Q} + \frac{i}{\hbar Q}(\vec{p}_j \times \hat{Q})\right)\right], \tag{2.35}$$

with $\vec{s}_j$ as the spin of the j^{th} electron at position $\vec{r}_j$. Equation (2.35) shows the two components of the interaction, with the first term involving $\vec{s}_j$ corresponding to the spin, and the second term to the orbital motion of electrons [89]. The distribution of electrons around the nucleus introduces a form factor for magnetic scattering intensity, $F_{\text{M}}(\vec{Q})$ which quickly decays with increasing Q. Empirically determined values of the magnetic form factor for different ions are tabulated in Ref. [90]. Further discussion of magnetic scattering is provided in Section 2.5.

2.5 Inelastic neutron scattering

The discussion so far has focused on elastic scattering, which provides information about the static nuclear and magnetic structures within a sample. Studies of the excitations are achieved via inelastic scattering where $E_i \neq E_f$. The origin of excitations are generally considered to be either purely structural (phonons) or magnetic (magnons), with each having a different dependence on $\vec{Q}$.

The excitations of a magnetic system with long-range order are oscillations of the moments about their equilibrium position. These excitations are known as spin waves, and the quanta of energy are called magnons [6]. The inelastic scattering of a neutron from a magnetic system can either create or destroy a magnon. For a ferromagnetic system, the scattering is described by

$$\begin{aligned}\frac{\partial^2\sigma}{\partial\Omega\partial E} =& \frac{(\gamma r_0)^2}{4\pi\hbar}\frac{k_f}{k_i}S(1+\hat{Q}_z^2)\left(\frac{gF_{\mathrm{M}}(\vec{Q})}{2}\right)^2\exp(-2W) \\ &\times\sum_{\vec{q},\vec{G}}[\,\langle n_q+1\rangle\delta(\hbar\omega_q-\hbar\omega)\delta(\vec{Q}-\vec{q}-\vec{G}) \\ &\qquad +\langle n_q\rangle\delta(\hbar\omega_q+\hbar\omega)\delta(\vec{Q}+\vec{q}-\vec{G})\,]\,,\end{aligned} \tag{2.36}$$

where $\vec{q}$ and $\hbar\omega_q$ are the wavevector and energy of the spin wave, and g is the Landé splitting factor which depends on the spin and total angular momentum quantum numbers, S and J, respectively. The Debye-Waller factor, $exp(-W)$ accounts for the thermal motion of atoms about their equilibrium position at finite temperature $T > 0\,\mathrm{K}$. Terms involving $\langle n_q+1\rangle$ and $\langle n_q\rangle$ respectively correspond to creation and annihilation of a magnon, which must satisfy the conservation laws imposed by the δ-functions. The thermal average of magnon density at $\vec{q}$ is given by Bose-Einstein

statistics

$$\langle n_q \rangle = \left[\exp\left(\frac{\hbar\omega_q}{k_{\mathrm{B}}T} \right) - 1 \right]^{-1},$$

where k_{B} is the Boltzmann constant [6, 89].

Excitations can also take the form of collective lattice vibrations that present as quasiparticles called phonons. The coherent component of the partial differential cross-section for one-phonon scattering is

$$\begin{aligned} \frac{\partial^2\sigma}{\partial\Omega\partial E}_{\mathrm{coh}} = \frac{k_f}{k_i}\frac{(2\pi)^3}{2v_0}\sum_{\vec{G}}\sum_{s}|G_s(\vec{Q})|^2 \\ \times \frac{1}{\omega_s}[\langle n_s+1\rangle\delta(\hbar\omega-\hbar\omega_s)\delta(\vec{Q}-\vec{q}-\vec{G}) \\ + \langle n_s\rangle\delta(\hbar\omega+\hbar\omega_s)\delta(\vec{Q}+\vec{q}-\vec{G})], \end{aligned} \tag{2.37}$$

where v_0 is the unit cell volume, $\hbar\omega_s$ is the phonon energy, and $G_s(\vec{Q})$ is the phonon structure factor for mode s, defined as

$$G_s(\vec{Q}) = \sum_j \frac{\bar{b}_j}{\sqrt{m_j}}(\vec{Q}\cdot\vec{e}_{j,s})\exp(-W_j)\exp\Big(i\vec{Q}\cdot\vec{r}_j\Big). \tag{2.38}$$

Here, $\vec{r}_j$ specifies the equilibrium position of atom j (of mass m_j) within the unit cell. The term $\vec{e}_{j,s}$ encodes the amplitude, direction and relative phase of mode s for atom j. The product $\vec{Q}\cdot\vec{e}_{j,s}$ leads to a Q^2 dependence of phonon intensity. At finite temperatures, this Q-dependence of a phonon mode is moderated by the Debye-Waller factor, which causes intensity to decay with increasing Q [6].

Multiple branches of each excitation may persist within the Brillouin zone. The lowest energy branch is called the acoustic branch and higher energy branches are known as the optic branches. A scattered neutron can either lose energy to create

an excitation mode with $\hbar\omega = E_i - E_f$ and waevector $\vec{q}$, or gain energy by absorbing a mode with $\hbar\omega = E_f - E_i$ and wavevector $-\vec{q}$ [6]. The intensity varies with energy because the two processes do not occur with equal rates. At low temperatures, the low occupation of high energy states will lead to fewer neutron energy-gain events, see Fig. 2.4 [89]. This is clearer to see from the coherent scattering function $S(\vec{Q}, \omega)$ defined as:

$$\frac{\partial^2\sigma}{\partial\Omega\partial E}_{\text{coh}} = A\frac{k_f}{k_i}S(\vec{Q}, \omega), \tag{2.39}$$

where A is an arbitrary constant. The principle of detailed balance states the difference between the two processes as

$$S(\vec{Q}, \omega) = \exp\left(\frac{\hbar\omega}{k_{\text{B}}T}\right)S(-\vec{Q}, -\omega). \tag{2.40}$$

A greater number of high energy states become populated as the temperature is increased, and the difference in the intensity of the two processes decreases [6].

Magnons and phonons also have an intrinsic temperature dependence that is separate from detailed balance. The intensity of magnons is expected to decay as the temperature is increase above the ordering temperature of the system. In contrast, the intensity from phonons is expected to increase with increasing temperature as a result of the population factor. This difference can be used to differentiate between the two types of excitations [89].

Another distinguishing feature of magnons and phonons is the dependence of intensity on Q. The magnetic intensity decays with increasing Q due to the magnetic form factor, whereas the intensity from phonons exhibits a Q^2 dependence [5, 6]. While these distinguishing feature provide some insight into the origin of an excitation, the analysis quickly becomes very complicated at temperatures and regions of

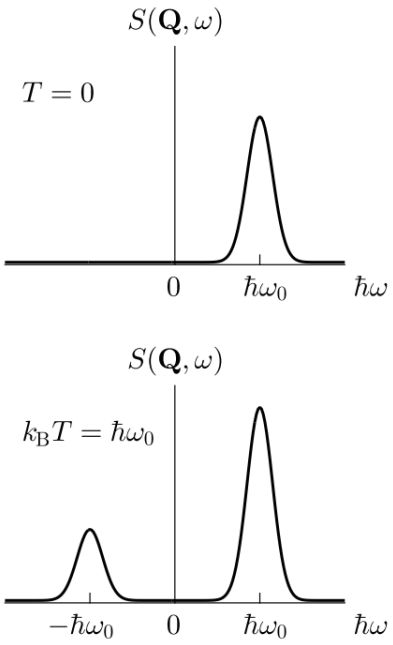

Figure 2.4: **Principle of Detailed Balance**. At low temperatures, a neutron energy-gain process has a lower intensity than a neutron energy-loss process involving the exchange of same amount of energy, $|\hbar\omega_0|$. The difference in intensity of the two processes is reduced as the temperature is increased. Image from Ref. [6].

Q where the excitations overlap. Unambiguous separation of magnons and phonons is achieved by performing a polarised neutron experiment, the details of which are discussed in Section 2.7.

2.6 Quasi-elastic neutron scattering

The neutron scattering techniques discussed thus far arise from static correlations in the case of elastic scattering, and dynamic correlations for inelastic scattering. These techniques are unable to provide information on diffusion of ions which is at the heart of the studies presented in this thesis. Quasi-elastic neutron scattering (QENS) is a variant of inelastic scattering involving the transfer of low energies between the neutron and the scattering system. QENS arises from configurational fluctuations within the system, such as the random hopping of atoms between equivalent sites [6].

QENS can arise either from coherent or incoherent scattering of neutrons by the scattering system. Coherent QENS is a probe of the pair distribution function, $G(\vec{r}, t)$ which gives the probability of finding an atom at the origin at time $t = 0$ and any atom at position vector $\vec{r}$ at a later time t. This enables the study of collective diffusive dynamics and dynamic disorder. Incoherent QENS is a probe of the self-correlation function, $P(\vec{r}, t)$ which gives the probability of finding an atom at the origin at $t = 0$ and the same atom at position vector $\vec{r}$ at a later time t. This enables the study of local vibrational and rotational modes, and translational diffusion. At very low temperatures, the self-correlation function becomes independent of time since vibrations are damped and ions generally become immobile. The time-dependence is regained as the temperature is increased and atoms become mobile.

The jump rate describing jump diffusion of ions is expressed in terms of the mean residence time τ that the ions spends on each site between jumps as

$$\frac{\delta P(\vec{r},t)}{\delta t} = \frac{1}{z\tau}\sum_{j}^{z}[P(\vec{r}+\vec{l}_j,t) - P(\vec{r},t)], \tag{2.41}$$

where $\vec{l}_j$ are vectors joining a site with its nearest neighbours, and the sum is performed over every possible hop up to the coordination number z. The first term in the sum corresponds to the increase in probability that site $\vec{r}$ is occupied after a jump from neighbouring sites, and the second term is the reduction in probability of occupation as a result of jumps away from $\vec{r}$ [6, 79].

A spatial Fourier transform of Eq. (2.41) yields the self intermediate scattering function, defined as

$$\begin{aligned} I(\vec{Q},t) &= \exp\left(-\frac{1}{z\tau}\sum_{j}^{z}\left[1-\exp\left(-i\vec{Q}\cdot\vec{l}_j\right)\right]t\right) \\ &= \exp\left(-\frac{1}{\hbar}\Gamma(\vec{Q})t\right). \end{aligned} \tag{2.42}$$

$I(\vec{Q},t)$ is comprised of two components - rotational and translational diffusion of atoms. Rotational diffusion is a special case of translational diffusion that arises when the diffusing particle is isolated from the bulk system by a spatial or energy barrier. This leads to a finite number of available sites for the particle. At $t = 0$, the two contributions are indistinguishable since $I(\vec{Q},0) = 1$. However, as $t \to \infty$, scattering contributions from rotational diffusion converge on a finite value whereas contributions from translational diffusion converge at zero [6, 79, 91].

The Fourier transform of Eq. (2.42) with respect to time yields the incoherent

scattering function, $S(\vec{Q},\omega)_{\text{inc}}$. For translational diffusion,

$$S(\vec{Q},\omega)_{\text{inc}} = \frac{1}{\pi}\frac{\Gamma(\vec{Q})}{\Gamma(\vec{Q})^2 + (\hbar\omega)^2} \tag{2.43}$$

is a quasi-elastic signal that is described by a Lorentzian function with a half-width at half maximum (HWHM)

$$\Gamma(\vec{Q}) = \frac{\hbar}{z\tau}\sum_{j}^{z}\left[1 - \exp\left(-i\vec{Q}\cdot\vec{l_j}\right)\right]. \tag{2.44}$$

In contrast, the localised nature of rotational diffusion leads to an additional elastic component in $S(\vec{Q},\omega)_{\text{inc}}$ [92]. Ideally, this characteristic scattering behaviour can be used to identify the presence of a rotational component to diffusion. In practice, an elastic response may be present due to scattering from the static atoms in the system.

A description of incoherent QENS arising from translational diffusion was developed in 1961 by Chudley and Elliott [91]. The Chudley-Elliott model of jump diffusion aimed to explain the diffusion mechanism in liquids using a Lorentzian with a HWHM of the form

$$\Gamma(Q) = \frac{\hbar}{\tau}\left(1 - \frac{\sin(Ql)}{Ql}\right), \tag{2.45}$$

where l is the scalar jump length between adjacent sites in direct space, and Q is the magnitude of the jump vector. It follows from this model that $\lim_{Q\to 0}\Gamma(Q) \propto Q^2$, in agreement with Fick's law. This is a distinct feature of translational diffusion. Away from $Q = 0$, $\Gamma(Q)$ tends towards a finite value that depends on the mean residence time τ between jumps. This value is approached in a sinusoidal manner, with shorter jumps corresponding to a much larger period in reciprocal space.

The Chudley-Elliott model provides a very good approximation for the diffusion of atoms in crystalline systems. Equation (2.45) is a simplification of Eq. (2.44) that results from taking a spatial average over all available jumps. This form is particularly useful for describing translational diffusion in polycrystalline systems, which have random orientations of jump vectors Q due to the random orientation of crystallites.

In cases when multiple hops with different τ and l are simultaneously present, the observed QENS signal can be described by separate Lorentzian functions for each mechanism. On the other hand, if multiple mechanism have the same jump length their contributions to the width cannot be separated. Then τ would correspond to an averages of the mean residence times.

2.7 Neutron polarisation analysis

The discussion thus far has only been concerned with scattering of radiation from one momentum and energy state to another. Further information about the nature of the scattering can be gained by specifically employing polarised neutrons as the probe and analysing the spin state in addition to momentum and energy. The advantage of including this extra dimension is the ability to unambiguously separate nuclear, magnetic and nuclear spin incoherent scattering.

The spin angular momentum is denoted by a operator $\boldsymbol{S}$ with components S_x, S_y and S_z. A detailed discussion of these operators is provided in Ref. [6]. The component S_z has eigenvalues $m_s = \pm(1/2)\hbar$, meaning that the neutron spin can either be parallel ("spin-up") or anti-parallel ("spin-down") to an arbitrary polarisation direction. For convenience, the neutron spin can be expressed in terms of Pauli matrices

by defining a dimensionless Pauli spin operator $\boldsymbol{\sigma} = 2\boldsymbol{S}/\hbar$, with components

$$\sigma_j = \begin{pmatrix} \delta_{j3} & \delta_{j1} - i\delta_{j2} \\ \delta_{j1} + i\delta_{j2} & -\delta_{j3} \end{pmatrix}, \tag{2.46}$$

where $j = 1, 2, 3$ indexes the x, y, z components, and δ_{jk} is 1 if $j = k$ and 0 otherwise [93].

A neutron beam is said to be polarised when one spin state predominates. The polarisation of a beam is described by a polarisation vector $\vec{P}$ with components along an arbitrary direction α defined as

$$P_\alpha = \frac{n_\uparrow - n_\downarrow}{n_\uparrow + n_\downarrow}, \tag{2.47}$$

where $n_\uparrow$ and $n_\downarrow$ are respectively the number of neutrons that are in the spin-up and spin-down state with respect to quantisation axis α. It follows from this definition that a beam of neutrons is unpolarised if $P = 0$, and perfectly polarised when $P = \pm 1$ [6].

The partial differential cross-section for spin polarised neutron scattering is very similar to Eq. (2.33) for magnetic scattering. In this case, $V(\vec{Q})$ has components from nuclear and electronic spin, expressed as

$$V(\vec{Q}) = \sum_j b_j \exp\Big(i\vec{Q} \cdot \vec{R}_j\Big) - \gamma r_0 \boldsymbol{\sigma} \vec{M}_\perp(\vec{Q}), \tag{2.48}$$

where $\vec{R}_j$ is the position vector and b_j is the nuclear scattering length of the j^{th} atom [94]. Nuclear and electronic spin scattering have comparable strengths since the value of γr_0 is generally comparable to b [6].

For polarised neutron scattering, the value of b has a dependence on the neutron polarisation that is expressed as

$$b = A + B\boldsymbol{\sigma}\boldsymbol{I}, \tag{2.49}$$

where A, B are constants and $\boldsymbol{I}$ is the nuclear spin operator [94]. Going forward, it is assumed that the nuclear spins and isotope distribution are both uncorrelated. Therefore, nuclear spin scattering will be entirely incoherent, and the coherent component of nuclear scattering can be expressed as

$$N(\vec{Q}) = \sum_j \overline{b}_j \exp\Big(i\vec{Q}\cdot\vec{R}_j\Big), \tag{2.50}$$

with $\overline{b}_j = \overline{A}_j$. Coherent nuclear scattering is independent of the neutron spin, hence the neutron spin is unaltered during a coherent nuclear scattering event. In contrast, components of magnetic scattering have the form

$$\left\langle \vec{k}_f\sigma_f \right| \boldsymbol{\sigma}\boldsymbol{M}_\perp(\vec{Q}) \left| \vec{k}_i\sigma_i \right\rangle \approx \sum_\alpha \left\langle \sigma_f \right| \sigma_\alpha \left| \sigma_i \right\rangle \left\langle \vec{k}_f \right| M_\perp^\alpha \left| \vec{k}_i \right\rangle, \tag{2.51}$$

which is explicitly dependent on the quantisation axis of the neutron spin. Expressing in this forms allows the neutron spin properties to be separated from the sample properties. The first term in the sum reveals that the neutron spin remains unchanged if the field direction is parallel or anti-parallel to spin quantisation axis. When the incident neutron spin and field are orthogonal the neutron is scattered with the spin flipped along the quantisation axis [94].

A description of polarised neutron scattering from the nuclei and unpaired electrons was first developed in 1963 by Blume [95] and Maleev *etl al.* [96]. The partial

spin state cross-section for equal-time correlations is

$$\frac{\partial^2\sigma}{\partial\Omega\partial E} = \langle N^*N\rangle_{T,\omega} + \langle \boldsymbol{M}_\perp^*\boldsymbol{M}_\perp\rangle_{T,\omega} + \langle N^*[\vec{P}_i\cdot\boldsymbol{M}_\perp]\rangle_{T,\omega} + \langle N[\vec{P}_i\cdot\boldsymbol{M}_\perp^*]\rangle_{T,\omega} + i\vec{P}_i\cdot\langle[\boldsymbol{M}_\perp^*\times\boldsymbol{M}_\perp]\rangle_{T,\omega} + \langle\nu_i\rangle_T + \langle\sigma_{\text{nsi}}\rangle_T. \tag{2.52}$$

Here, $\vec{P}_i$ is the incident polarisation vector, ν_i is the isotope incoherent term, σ_{nsi} is the nuclear spin incoherent term, and the coherent nuclear and magnetic scattering at $\vec{Q}$ are denoted by N and $\boldsymbol{M}_\perp$, respectively. The subscripts T and ω correspond to thermal average and Fourier transform with rest to time [94].

2.7.1 *xyz* polarisation analysis

The xyz polarisation analysis (PA) technique is an implementation of uniaxial polarisation analysis. In general, an orthogonal, right-handed coordinate system is defined with $\hat{x} \parallel \hat{Q}$ ($\phi = 0$), $\hat{z}$ is orthogonal to the scattering plane, and $\hat{y} = \hat{z}\times\hat{x}$, as illustrated in Fig. 2.5. The incident neutron polarisation is oriented along the x, y and z direction using a guide field at the sample position, and the scattered neutron polarisation is analysed with respect to the quantization axis of incident neutron spins.

A scattering event in which neutrons incident with polarisation parallel to an axis α emerge with flipped spins is denoted by $\sigma^{\alpha\overline{\alpha}}$. The elastic cross-sections and their compositions along each quantisation axis are provided in Table 2.1. Thermal averages and Fourier transforms from Eq. (2.52) have been omitted for brevity. These expressions reveal that non-spin-flip scattering along x (σ^{xx} and $\sigma^{\overline{xx}}$) does not contain a magnetic component $\boldsymbol{M}_\perp$, while spin-flip scattering along y and z have no structural component N.

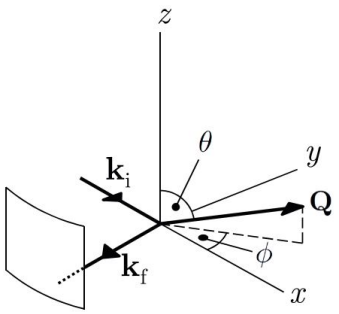

Figure 2.5: **Geometry of a *xyz* polarisation analysis set-up**. The direction of the scattering vector $\vec{Q}$ is specified by the spherical polar angles θ and ϕ. Image from Ref. [6].

$\sigma^{xx} = \sigma^{\overline{xx}} = NN^* + \nu_i + \frac{1}{3}\sigma_{\mathrm{nsi}}$
$\sigma^{x\overline{x}} = \boldsymbol{M}_\perp^* \boldsymbol{M}_\perp + i\hat{x} \cdot (\boldsymbol{M}_\perp^* \times \boldsymbol{M}_\perp) + \frac{2}{3}\sigma_{\mathrm{nsi}}$
$\sigma^{\overline{x}x} = \boldsymbol{M}_\perp^* \boldsymbol{M}_\perp - i\hat{x} \cdot (\boldsymbol{M}_\perp^* \times \boldsymbol{M}_\perp) + \frac{2}{3}\sigma_{\mathrm{nsi}}$
$\sigma^{yy} = NN^* + (\boldsymbol{M}_\perp \cdot \hat{y})(\boldsymbol{M}_\perp^* \cdot \hat{y}) + \hat{y} \cdot (\boldsymbol{M}_\perp N^* + \boldsymbol{M}_\perp^* N) + \nu_i + \frac{1}{3}\sigma_{\mathrm{nsi}}$
$\sigma^{\overline{y}\overline{y}} = NN^* - (\boldsymbol{M}_\perp \cdot \hat{y})(\boldsymbol{M}_\perp^* \cdot \hat{y}) + \hat{y} \cdot (\boldsymbol{M}_\perp N^* + \boldsymbol{M}_\perp^* N) + \nu_i + \frac{1}{3}\sigma_{\mathrm{nsi}}$
$\sigma^{y\overline{y}} = \sigma^{\overline{y}y} = (\boldsymbol{M}_\perp \cdot \hat{z})(\boldsymbol{M}_\perp^* \cdot \hat{z}) + \frac{2}{3}\sigma_{\mathrm{nsi}}$
$\sigma^{zz} = NN^* + (\boldsymbol{M}_\perp \cdot \hat{z})(\boldsymbol{M}_\perp^* \cdot \hat{z}) + \hat{z} \cdot (\boldsymbol{M}_\perp N^* + \boldsymbol{M}_\perp^* N) + \nu_i + \frac{1}{3}\sigma_{\mathrm{nsi}}$
$\sigma^{\overline{z}\overline{z}} = NN^* - (\boldsymbol{M}_\perp \cdot \hat{z})(\boldsymbol{M}_\perp^* \cdot \hat{z}) + \hat{z} \cdot (\boldsymbol{M}_\perp N^* + \boldsymbol{M}_\perp^* N) + \nu_i + \frac{1}{3}\sigma_{\mathrm{nsi}}$
$\sigma^{z\overline{z}} = \sigma^{\overline{z}z} = (\boldsymbol{M}_\perp \cdot \hat{y})(\boldsymbol{M}_\perp^* \cdot \hat{y}) + \frac{2}{3}\sigma_{\mathrm{nsi}}$

Table 2.1: **Scattering cross-sections for *xyz* polarisation analysis** [29].

It is worth noting that the xyz technique is not suitable for the study of ferromagnetic systems, because the polarisation of the neutron beam is lost due to the presence of different magnetic domains [90]. This is not an issue for the work presented in this thesis since the xyz PA studies were carried out in the paramagnetic phase of the samples.

2.8 Neutron spectrometers

Neutrons used for scattering experiments have energies on the order of 10 to 100 meV (1 meV $\equiv$ 11.604 K) which give wavelengths comparable to the interatomic spacing of materials. A high flux of neutrons with these properties can be accessed through spallation and reactor sources. A reactor source such as the Institut Laue-Langevin (ILL) employs a nuclear fission reactor optimised for neutron generation to provide a continuous beam. Inside the reactor, isotopically enriched uranium (^{235}U) fuel undergoes fission with thermal neutrons to release on average 2.5 fast neutrons per fission event, each with an energy of $\sim$ 1 MeV. The fuel rods are submerged in a H_2O or D_2O moderator that slows down the fast neutrons until they come close to thermodynamic equilibrium. Energies of the moderated neutrons follow a Maxwell-Boltzmann distribution, with a peak in flux at the energy corresponding to the moderator temperature. Hollow neutron guide tubes positioned tangentially around the reactor core transport the neutrons from the reactor to the experimental halls where scattering instrumentation are installed. Neutron energies along a beamline can be tuned by under-moderating the reactor core and using local moderating material at higher or lower temperatures [7, 90].

For many years reactor sources have been leading in the flux of neutrons they

deliver, however they have now reached the limit of their technological capabilities. Relatively speaking, spallation technology is still in its infancy and has the potential to deliver even higher fluxes [7]. Spallation neutron sources create short pulses of neutrons by colliding high energy particles into a heavy metal target, often tungsten or lead. The high energy particles are produced by an ion source and bunched together before being accelerated in a synchrotron particle accelerator. The spallation reaction is a sequential one that starts with the incorporation of the incident particle by a nucleus in the target, which initiates a cascade process eventually producing 20 to 30 neutrons per incident proton [90]. The spallation neutrons are moderated before entering the neutron beam guide to be delivered at the scattering instruments.

At the ISIS Neutron and Muon Source, 800 MeV protons strike one of two tungsten targets 50 time per second, with 4 out of every 5 bunches being directed to target station 1 (TS1). Details of the spallation components installed at ISIS are available in Ref. [97]. The key advantage of using a pulsed beam of neutrons is that the neutron energy can be accurately determined from its time-of-flight (TOF) measured by sensitive timing equipment along the guide tube between the target and the instruments.

2.8.1 Time-of-flight spectrometers

The intrinsic pulsed nature of the beam at a spallation source makes it well suited for time-of-flight spectrometry. However, TOF spectrometers can also be realised at reactor sources by employing additional pulsing devices. The use of multi-detectors make TOF spectrometers well suited to surveying excitations over a broad range of $Q - E$ space.

In a TOF spectrometer, the energy transfer between incident neutrons and the sample is determined from the neutron's time-of-flight between two points a known distance apart and its incident/final energy. Figure 2.6 shows the schema for the two possible geometries of a TOF spectrometer; the key distinction between direct and indirect geometry spectrometers is that the former uses a monochromatic incident beam with a fixed incident energy E_i, while the latter employs an analyser crystal to select a particular final energy E_f after the scattering event [7]. Here, the focus will be on direct geometry MAPS and LET spectrometers of the ISIS facility which were used during the works presented in this thesis.

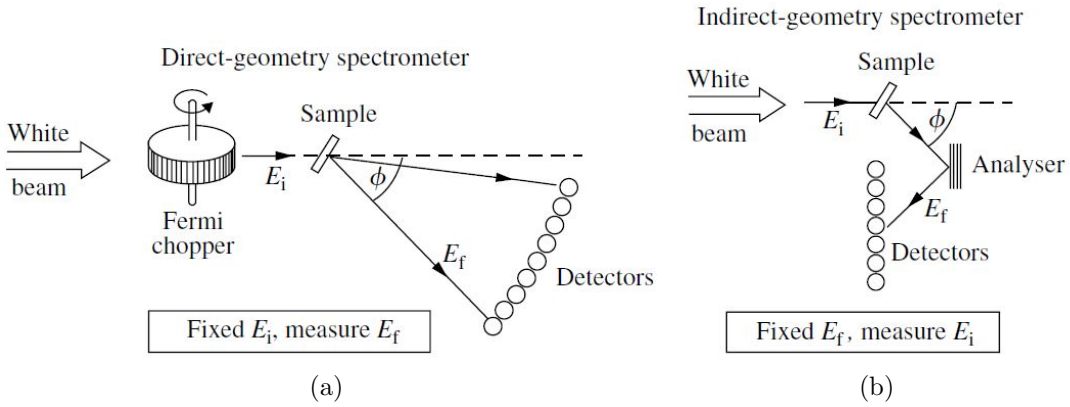

Figure 2.6: **Schema of different TOF spectrometer geometries**. (a) A direct geometry instrument employs choppers to create a monochromatic incident beam, and determines E_f from the neutron time-of-flight. (b) Indirect geometry instruments illuminate the same with a white beam and use an analyser crystal to backscatter neutrons of a particular E_f to the detector. Then the neutron TOF is used to determine E_i. Figures sourced from Ref. [7].

The incident pulse leaving the spallation source has a distribution of neutron energies, and is referred to as a white beam. A direct geometry spectrometer monochromates the incoming beam using a series of rotating mechanical choppers along the

beam guide to the sample environment. After the scattering event, the energy transfer between the sample and the beam is determined from the neutron's time-of-flight over the known distance between the sample position and the detector array. Neutrons which gain energy from the sample will be detected first, whereas those that have lost energy will be detected later.

A chopper is a device constructed from neutron absorbing materials with specifically engineered windows that allow neutrons to pass through. The successful operation of a chopper relies on the precise knowledge of when the neutrons are produced, and the fixed path length between the source and the chopper position. The two types of choppers, Fermi and disk, both operate based on the same principle; the frequency of rotation is set such that the window in the chopper aligns with the incident neutrons at the exact moment when those with the desired energy reach the chopper position. The chopper defines the profile of an instrument's energy resolution and its background level, which can be further engineered using a series of choppers operating out of phase with each other [7].

The MAPS spectrometer located in TS1 views a water moderator at 300 K which provides incident neutrons with energies of $15 - 2000$ meV, making it suitable for the study of high energy excitations. A combination of Fermi and disk choppers are employed to minimise the background and improve neutron utilisation by allowing simultaneous measurements with multiple incident energies, a mode of operation known as 'repetition rate multiplication' (RRM), illustrated in Fig. 2.7 [8]. A choice of two interchangeable Fermi choppers are available to optimise for either higher neutron flux or better energy resolution. The scattered beam is analysed by an array of ^{3}He position-sensitive detectors (PSDs) comprised of 40,000 pixels, providing an almost continuous coverage of the solid angle in the forward direction [7]. Each ^{3}He

detector tube maps out an arc through $Q - E$ space.

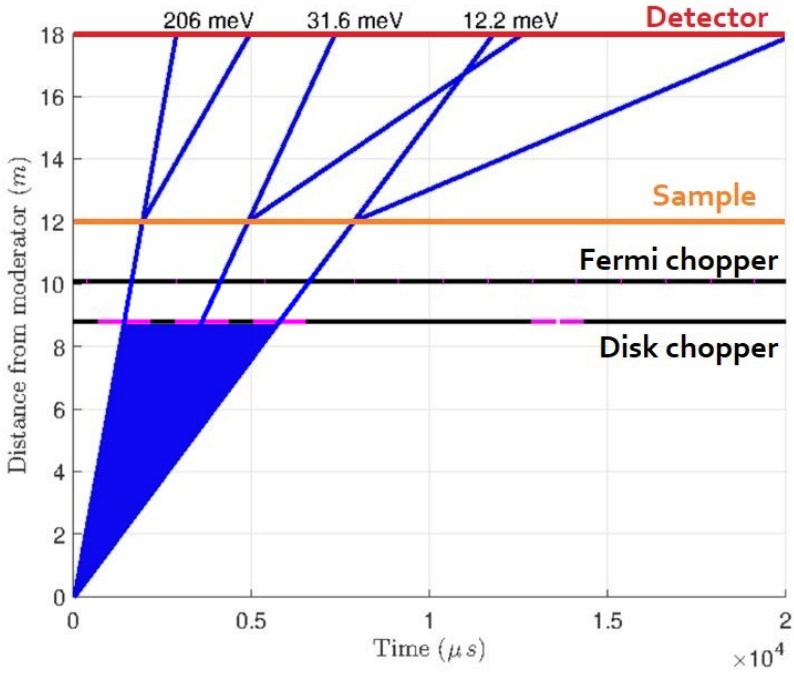

Figure 2.7: **A time-distance graph illustrating the RRM mode on the MAPS direct geometry spectrometer**. Neutrons with $E_i = 15 - 2000\,\text{meV}$ leave the water moderator at time $t = 0\,\mu\text{s}$. The disk chopper operating at 50 Hz is encountered 8.8 m along the guide tube, followed by the Fermi chopper operating at 400 Hz. This configuration allows neutrons with incident energy $E_i \sim 206, 31.6$ and $12.2\,\text{meV}$ to reach the sample situated 12 m downstream of the moderator. These scatter elastically and inelastically before reaching the ^{3}He PSDs. Figure adapted from Ref. [8].

Measurement of low energy excitations and quasi-elastic scattering necessitate the use of a cold neutron spectrometer such as LET, situated in the second target station of the ISIS facility. The broad energy range emitted by the high intensity, cold, solid methane moderator of TS2 allows LET to operate over incident energies of $0 - 30\,\text{meV}$. High flux of neutrons in this range together with extremely low background and versatile sample environment make LET well suited to the study of

dynamics below 25 meV in energy.

LET employs five disk choppers along the 25 m flight path between the moderator and the sample environment, with each operating at a different speed, see Fig. 2.8. This multi-chopper arrangement makes it possible to finely tune the pulse shape, incident energies, and the associated energy resolution. Another advantage is the realisation of RRM mode, enabling simultaneous measurement of quasi-elastic and inelastic scattering. The energy resolution on LET ranges from 0.8 % at $E_i = 1$ meV to 1.5 % at $E_i = 20$ meV. The large area multi-detector is comprised of 4 m long ^{3}He PSDs located 3.5 m away from the sample environment, providing high resolution continuous coverage of π st in the forward direction [9]. This allows a large volume of reciprocal space to be probed in a single measurement.

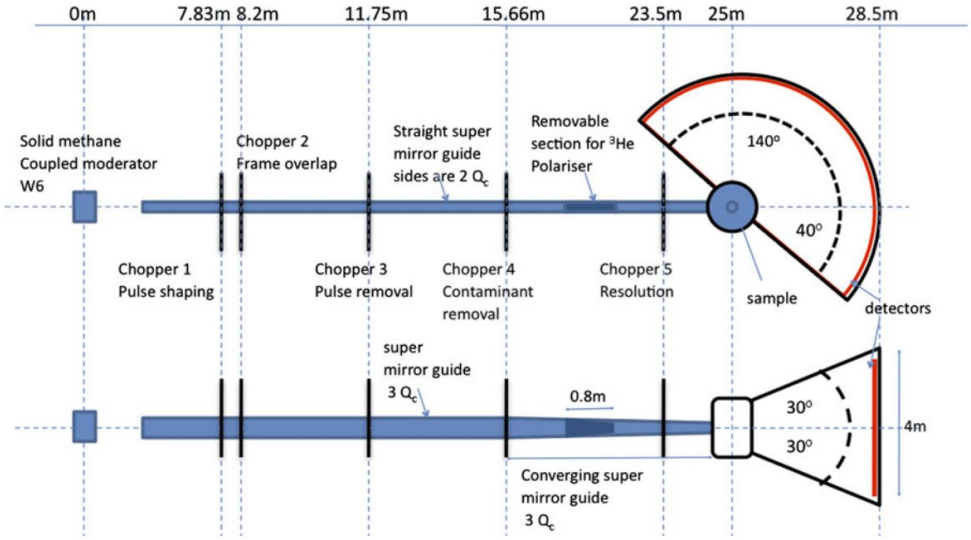

Figure 2.8: **Schematic of the LET spectrometer at the ISIS facility**. Image from Ref. [9].

2.8.2 Triple-axis spectrometers

In contrast to TOF spectrometers, a triple-axis spectrometer (TAS) operates in a step-by-step mode which makes them well suited to the study of excitations at a particular point or along a given direction in $Q - E$ space. TAS are commonly installed at reactor sources where a higher flux of incident monochromatic neutrons are available, thus offsetting the reduced information obtained in each scan [7, 90].

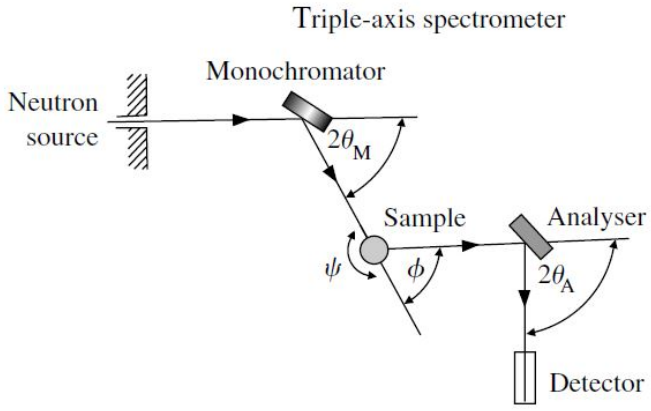

Figure 2.9: **Schematic diagram of triple-axis spectrometers**. Black arrows indicate the direction of travel for the neutrons, which encounter the monochromator then scatter off the sample and encounter the analyser before arriving at the single detector. Image from Ref. [7].

A TAS is comprised of three crucial components - a crystal monochromator, the sample and a crystal analyser, each of which can rotate on its axis, see Fig. 2.9. Neutrons produced at the source emerge with a distribution of energies and the monochromator is responsible for selecting a single energy, thereby defining the incident neutron wave vector $\vec{k_i}$. At the sample position, a variety of environments can be installed to control the temperature, pressure, magnetic or electric field strength. Neutrons scatter from the sample with a spectrum of energies and the analyser allows only those with a specific energy (and k_f) to reach the single detector.

Typically, the monochromator and analyser are comprised of many small single crystals of either copper, silicon, germanium, beryllium or pyrolytic graphite (PG). The multi-crystal array is mounted on a mechanical device that provides control over the orientation of the individual crystals, making it possible to focus the beam on the sample and detector. Heavy neutron shielding around the monochromator and analyser ensures that only certain neutrons are able to propagate beyond. Neutrons having the desired energy and wavelength are selected through Bragg reflection by an angle θ from a family of (hkl) planes of the monochromator and analyser crystal [90].

The Bragg reflected beam will have the nominal wavelength λ along with higher order harmonics λ/n (where $n = 2, 3...$) reflected by the (nh, nk, nl) planes. These give rise to spurious signals if permitted to reach the detector. Measures to prevent higher-order harmonic contamination include the use of a helical velocity selector - a rotating cylinder fabricated from a neutron-absorbing material, with helical grooves along the outer surface. Neutrons having an allowed velocity navigate through the grooves while those which are too fast or too slow strike the walls. Higher-order contamination can also be tackled using neutron absorption filters which have particular chemistries to match a target wavelength. On cold neutron spectrometers, such as those used during the works reported in this thesis, it is common to use a cooled polycrystalline beryllium filter to ensure that only neutrons with $k < 1.57\,\text{Å}^{-1}$ are transmitted [7, 90].

The cold neutron triple-axis spectrometer ThALES was used during the works presented in this thesis. Situated within the reactor hall at the ILL, ThALES is provided with a high flux of low energy neutrons which make it well suited to the study of weak excitations in the energy range $0.2 - 10\,\text{meV}$ with an energy resolution $\sim 3\,\%$ of E_i [10].

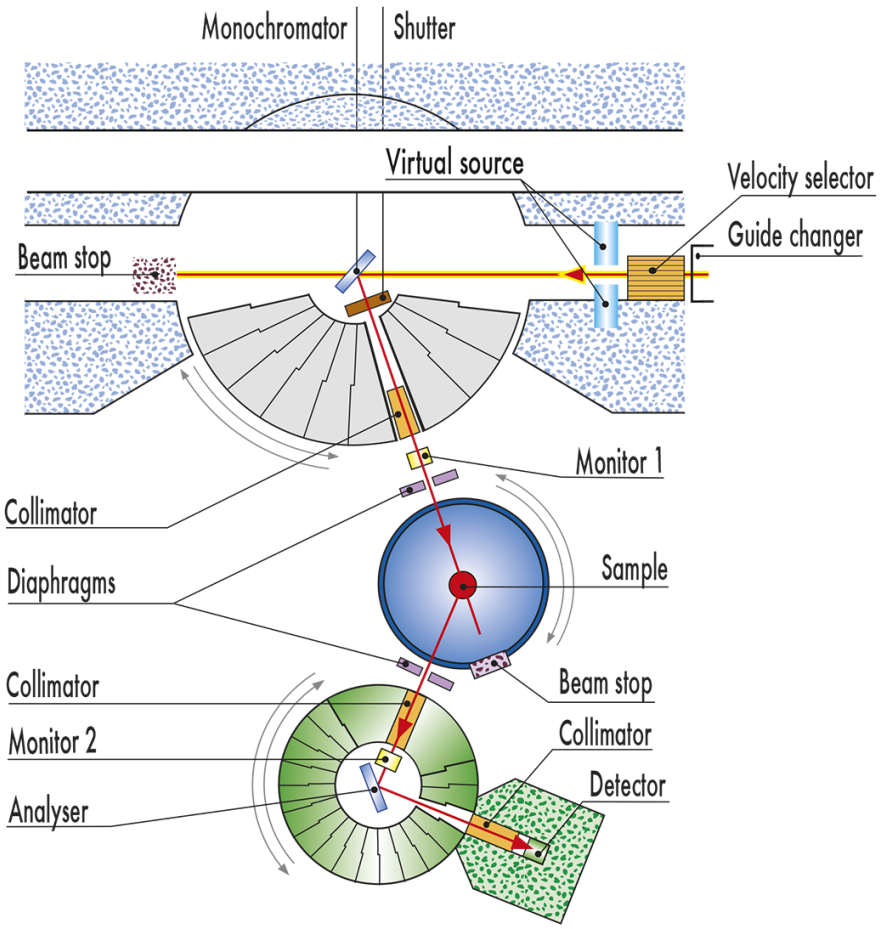

Figure 2.10: **Schematic of triple-axis spectrometer ThALES at the ILL**. Image from Ref. [10].

The layout of ThALES is shown in Fig. 2.10. A choice of heusler, pyrolytic graphite or silicon crystals are available as the monochromator and analyser. The choice of crystal depends on the requirements of the experiment, with PG offering the highest flux, and silicon able to access higher energies [10]. The polarised neutron experiments reported in this thesis were performed using the (111) plane of a heusler crystal.

Other important components include the beam monitors and diaphragms. The incident beam monitor is a low-efficiency detector that is used to remove any artefacts of fluctuations in the incident flux. The second monitor is sometimes used to investigate spurious signals in the spectra [90]. In cases when the beam height and width are much greater than the sample, the neutrons reaching the detector without scattering lead to an increased background. The diaphragms, constructed from neutron absorbing materials, allow control of the beam size to reduce such effects.

2.8.3 *xyz* polarisation analysis on ThALES

Polarised neutron studies presented in this thesis were performed by adapting ThALES to utilise *xyz* polarisation analysis. This is achieved by introducing two new components to the standard TAS set-up that allow manipulation of the polarised incident beam - the Mezei spin-flipper and the Helmholtz coil set. A polarised beam is generated using the (111) family of planes from a Heusler monochromator crystal. A Heusler crystal is a ferromagnetic metal alloy which has comparable magnitudes of nuclear ($F_N(\vec{Q})$) and magnetic ($F_M(\vec{Q})$) structure factors for reflections from the (111) family of planes. The scattered intensity is proportional to $F_N(\vec{Q})^2 + F_M(\vec{Q}^2)$ when the neutron spin is parallel to the internal magnetic moment, and $F_N(\vec{Q})^2 -$

$F_M(\vec{Q})$ when anti-parallel [90]. The polarisation of the resulting monochromatic beam is parallel to the z-direction.

The beam polarisation is manipulated using magnetic fields generated by the Mezei flipper and Helmholtz coil set. The spin quantisation axis is switched between x, y and z by the Helmholtz coil set around the sample environment. Figures 2.11a and 2.11b show the arrangement of the independent coils that make up the Helmholtz coil set (each represented by a different colour), and the corresponding field directions. The resultant magnetic field adiabatically rotates the polarisation axis to be parallel with the desired direction at exactly the sample position, and the polarisation of scattered neutrons is adiabatically reverted back to point along the z axis [11, 98].

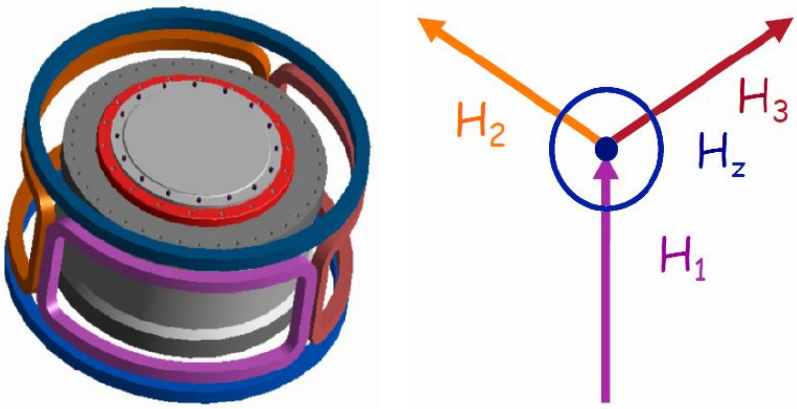

(a) (b)

Figure 2.11: **The Helmholtz coil set**. (a) The coil set is composed of five different coils. (b) A representation of the field direction for each coil in (a). Images sourced from Ref. [11].

If activated, the Mezei flipper produces a field orthogonal to the z-direction to reverse the spin direction through a non-adiabatic transition [90, 98, 99]. Beyond the flipper, at the Heusler crystal analyser, only neutrons in the spin state σ^z are

reflected into the detector.

The data collected during a polarised neutron experiment requires additional corrections due to the finite polarisation of the beam, inefficiencies in the flipper, and the analysing power of the analyser. Below is a summary of polarisation correction from Ref. [84]. A comprehensive discussion of polarisation corrections is provided in Ref. [100].

The inefficiencies of the polarisation analysis components can be quantified by measuring the diffuse scattering from a quartz sample. An ideal polarisation analysis set-up with a perfectly polarised beam, and perfect flipper and analyser will not detect any spin-flip scattering from quartz since the scattering is entirely nuclear. Hence, the scattering from quartz is ideal for quantifying the flipping ratio defined as

$$F = \frac{n_{\uparrow}}{n_{\downarrow}}. \tag{2.53}$$

In the limit of large F, which corresponds to minor inefficiencies in the set-up, the corrected non-spin-flip (nsf) and spin-flip (sf) differential cross-sections are given by

$$\frac{d\sigma}{d\Omega}^{\text{corr}}_{\text{nsf}} = \frac{d\sigma}{d\Omega}_{\text{nsf}} + \frac{1}{F-1}\left[\frac{d\sigma}{d\Omega}_{\text{nsf}} - \frac{d\sigma}{d\Omega}_{\text{sf}}\right] \tag{2.54}$$

$$\frac{d\sigma}{d\Omega}^{\text{corr}}_{\text{sf}} = \frac{d\sigma}{d\Omega}_{\text{sf}} - \frac{1}{F-1}\left[\frac{d\sigma}{d\Omega}_{\text{nsf}} - \frac{d\sigma}{d\Omega}_{\text{sf}}\right]. \tag{2.55}$$

2.9 X-ray diffraction on lab sources

Powder X-ray diffraction is used in Chapters 3 and 4 to check the phase purity of samples and study superstructure formation in $Na_{0.67}Fe_{1/2}Mn_{1/2}O_2$. This sections

provides a brief background on X-ray diffractions and details the instruments which have been utilised during the works presented in this thesis.

2.9.1 X-ray scattering

X-ray scattering arises from the electromagnetic interaction with the orbital electrons in a material. The distribution of electrons around the nucleus means X-ray scattering is not point-like. Hence, relating back to the discussion in Section 2.2.2, X-ray scattering intensity varies as $\sin(\theta)/\lambda$. The scattering power of an atom is influenced by the density of electrons $\rho(\vec{r})$. In contrast to neutrons, for which the structure factor depends on the constant scattering length b, the X-ray structure factor depends on the atomic form factor defined as

$$f(Q) = Zg(Q)r_e, \tag{2.56}$$

where Z is the atomic number, r_e is the classical radius of the electron, and $g(Q)$ is the Fourier transform of the electron charge density, which decays from 1 at the origin to 0 as $Q \to \infty$ [5]. Analytical approximations of $g(Q)$ are based on empirically determined parameters tabulated in Ref. [101].

2.9.2 Lab source X-ray generation

The x-ray measurements reported in this thesis were all performed using lab based sources of X-rays. These systems produce x-rays by accelerating electrons across a large potential gap towards a heavy metal target such as copper or molybdenum. Two different mechanisms lead to the production of photons upon collision with the metal target. The Bremsstrahlung process, also referred to as 'braking radiation',

is the direct production of a continuum of wavelengths upon rapid deceleration of electrons. The second process is fluorescence, in which photons are produced at a discrete set of wavelengths that depend on the energy of the incident electron and the target material. Fluorescence arises when the incoming electron delocalises an electron from the inner shells of an atom in the target, which is followed by the relaxation of an electron from a higher energy level to occupy the vacancy, emitting a photon with energy equal to the difference in the two energy states. The K_α line of an element, which corresponds to a transition from the second lowest energy level to the ground state, produces x-rays with the greatest intensity [5].

2.9.3 X-ray diffractometers

The Xcalibur diffractometer by Agilent Technologies is a fully automated system controlled by the CrysAlis$^{\text{Pro}}$ software which is used to both perform experiments and analyse the data. A labelled image of the Xcalibur is shown in Fig. 2.12. X-rays generated by a molybdenum source pass through a monochromator to produce a monochromatic beam with $\lambda = 0.709\,\text{Å}^{-1}$ that is then collimated to reduce beam divergence. At the sample position a 4-circle kappa goniometer can rotate the sample through almost any angle with high angular resolution. The scattered x-rays are detected by a CCD camera area detector which hosts a beryllium window and scintillation screen to convert x-rays into visible light [102].

While the Xcalibur diffractometer supports measurements in both transmission and reflection modes, the x-ray data reported in this thesis were acquired using the transmission mode only. Typical duration of experiments on polycrystalline samples range from 15 minutes to an hour, whereas for single crystal samples it can take

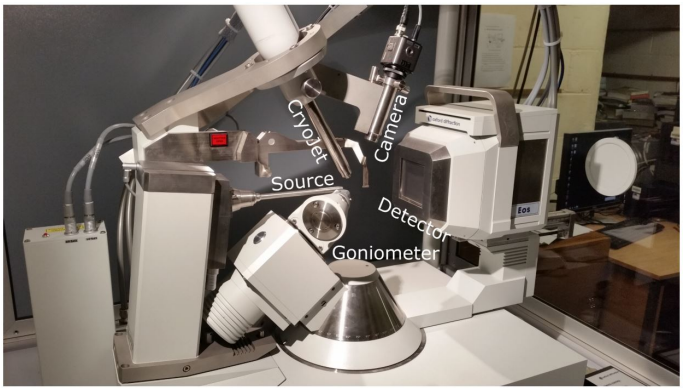

Figure 2.12: **Xcalibur X-ray diffractometer**. X-rays generated from a Mo source scatter from the sample mounted on the goniometer in the middle, and are detected by a CCD camera area detector on the right. Image from Ref. [12].

12 hours or longer to collect high resolution data with full coverage of reciprocal space. Experiments strategies are automatically calculated by the CrysAlis$^{\text{Pro}}$ software which allows the user to select the desired resolution and coverage. During an experiment, sequences of frames are captured by the CCD camera for each orientation of the sample and detector, and then stitched together and analysed within CrysAlis$^{\text{Pro}}$.

The operating principles of the Gemini S diffractometer by Agilent Technologies are identical to the Xcalibur described above. The distinguishing factors between the two diffractometers are the upgraded x-ray generation and detection systems installed on the Gemini S. A fine x-ray beam can be generated with a choice of copper and molybdenum targets. The HyPix-6000HE hybrid photon detector installed on the Gemini S captures 100 frames per second with a pixel size of $100\,\mu\text{m} \times 100\,\mu\text{m}$ [103]. A Cryostream 800 Plus system, also operated through the CrysAlis$^{\text{Pro}}$ software, offers a laminar nitrogen gas flow to control sample temperature over $\sim 100 - 500\,\text{K}$ [104].

High resolution polycrystalline x-ray diffraction measurements were performed using a Rigaku Smartlab system in the Materials Characterisation Laboratory at the ISIS Neutron and Muon Source. This system generated high intensity x-rays from a rotating Cu anode, and creates a monochromatic fine beam using Ge crystals and a automatic variable divergence slit. Data quality is improved using a high-precision goniometer to rotate the sample stage at each 2θ position of the semiconductor photon detector; thereby averaging the effects of surface imperfections and preferential ordering of layered samples. Measurement strategies are defined within the Smartlab Guidance software which controls the orientation of the source, sample and detector. High quality diffraction data over $2\theta = 5 - 154^\circ$ can be acquired in as little as 1 hour.

Chapter 3

Is $AgCrSe_2$ a Phonon-Liquid Electron Crystal?

3.1 Literature review

Superionic $AgCrSe_2$ has recently attracted much attention for its ultra-low κ of $\sim 0.2 - 0.5\,\mathrm{WK^{-1}m^{-1}}$, see Fig. 3.1a [13, 62, 105]. Combined with a large Seebeck coefficient this enables $AgCrSe_2$ to achieve good thermoelectric performance with $zT \sim 1$ at high temperature, as shown in Fig. 3.1b. In the superionic phase at $T > 450\,\mathrm{K}$, the thermal conductivity becomes almost temperature independent owing to the pseudo two-dimensional lattice of highly mobile Ag^+ ions. Despite extensive studies, the atomic dynamics responsible for this extremely low κ remain controversial.

The crystal structure of $AgCrSe_2$ is built up of edge sharing $CrSe_6$ octahedra that sandwich layers of tetrahedral Ag^+ sites, see Fig. 3.2a [17, 106, 107]. The ABC type stacking of Cr leads to two equivalent sites, α and β, for Ag^+ ions. Only the α site

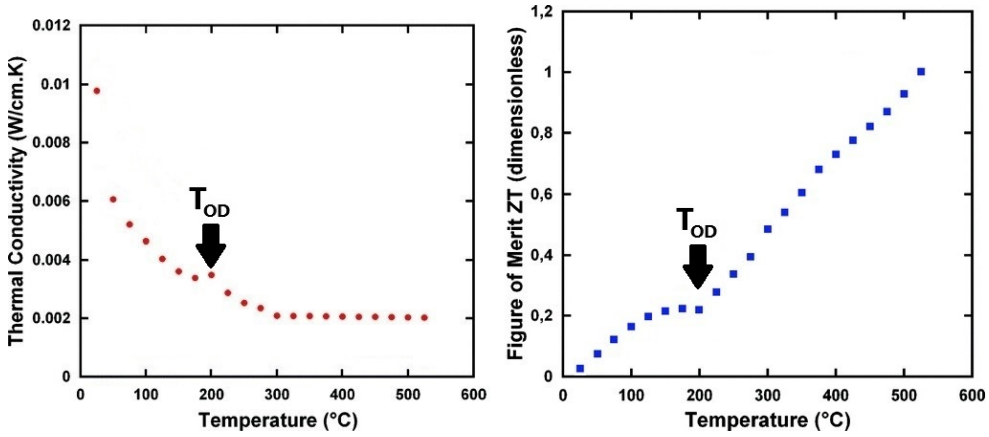

(a) (b)

Figure 3.1: **Thermoelectric parameters of $AgCrSe_2$.** (a) Thermal conductivity, κ as a function of temperature calculated using experimental C_p values. (b) Temperature dependence of the thermoelectric figure of merit, which exceeds 1 at $T > 500\,^{\circ}\mathrm{C}$. Both figures exhibit a marked change upon entering the superionic regime at $T > 200\,^{\circ}\mathrm{C}$ [13].

is occupied below the superionic transition temperature, T_{OD} of $\sim 450\,K$, and the structure has $R3m$ symmetry. Above T_{OD}, the system undergoes an order-disorder transition involving the migration of Ag^{+} ions from α to β site (Fig. 3.2b) with equal occupation of both, and the structure adopts $R\bar{3}m$ symmetry [107].

A recent inelastic neutron scattering (INS) study by Li *et al.* reported evidence to suggest that the phonon-liquid electron-crystal (PLEC) concept may explain the origin of the ultra-low κ in $AgCrSe_2$ [14]. In the PLEC model, it is assumed that liquids are unable to host shearing forces. Hence, the propagation of significant heat carrying transverse phonon modes is prohibited in liquids [78, 108, 109]. The PLEC concept intends to exploit this characteristic of liquids to significantly reduce the thermal conductivity in solids with a liquid-like substructure, such as superionic conductors. It posits that liquid-like behaviour resulting from superionic diffusion in

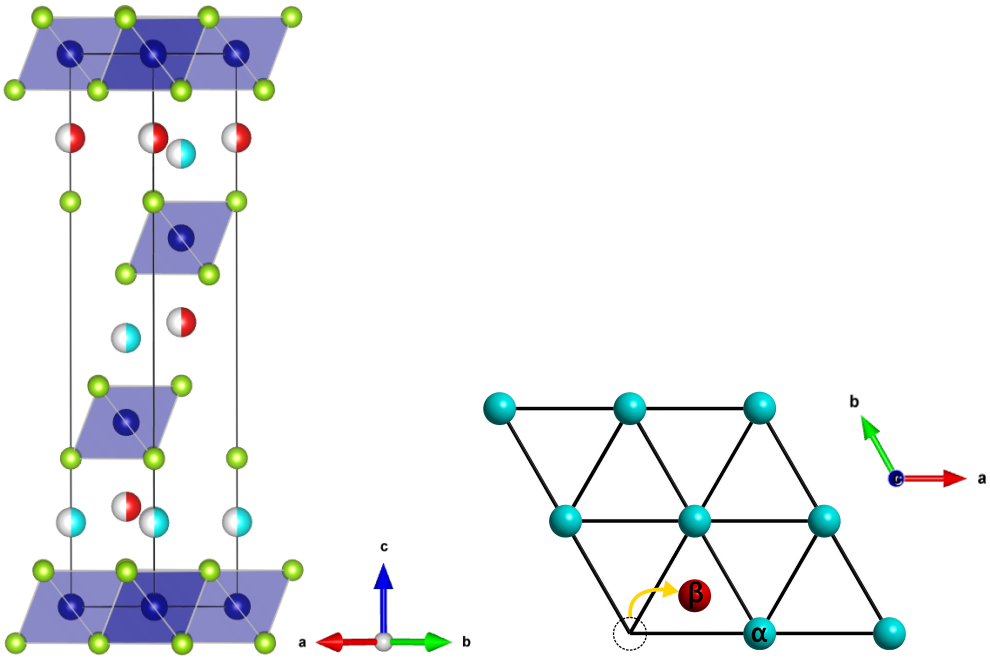

(a) (b)

Figure 3.2: **Crystal structure of $AgCrSe_2$**. (a) Unit cell with Se shown in green, Cr in blue and two possible Ag sites, α and β shown in cyan and red, respectively. (b) Above T_{OD} the Ag ions move from α to β site with an average equal occupation of both.

one crystal sublattice suppresses the transverse acoustic (TA) phonon modes, while another rigid sublattice provides a crystalline environment for the diffusion of charge carriers [49].

Whether a material qualifies as a PLEC depends upon the time-scales of the dynamic processes involved [72]. In liquids, the residence time τ is the time between atomic jumps from one equilibrium position to another. Frenkel *et al.* identified that the comparison of τ and the vibrational period determines whether propagation of shear waves is possible in a liquid. Transverse acoustic phonon modes are suppressed when τ is shorter than the phonon period. If, however, τ is much longer than the phonon period then waves propagate just as in a solid [50, 108].

The PLEC concept was first used by Liu *et al.* to explain the extremely low κ_L in Cu_2Se [49]. However, INS from Cu_2Se has found that the phonon period is smaller than τ, hence the TA phonon modes continue to exist [72]. Recent neutron studies investigating the origin of ultra-low κ_L in $AgCrSe_2$ have reached conflicting conclusions [14,15]. Polycrystalline INS study by Li *et al.* observed extremely broad quasi-elastic neutron scattering (QENS) originating from $Q \sim 2\,\text{Å}^{-1}$ at $T < \mathrm{T_{OD}}$, see Fig. 3.3a. The QENS signal broadens dramatically upon entering the superionic phase and eventually merges with the non-dispersive TA phonons at $E \sim 3\,\text{meV}$, as shown in Fig. 3.3b-c. This behaviour was interpreted as arising from ionic diffusion with sufficiently low τ to suppress the TA phonon modes in the superionic phase [14].

More recent work by Ding *et al.* concluded that the PLEC concept fails to explain the dynamics in $AgCrSe_2$. This study utilised both polycrystalline INS and single crystal inelastic x-ray scattering (IXS) techniques to further investigate the behaviour of TA phonons above and below T_{OD}. Single crystal data enables

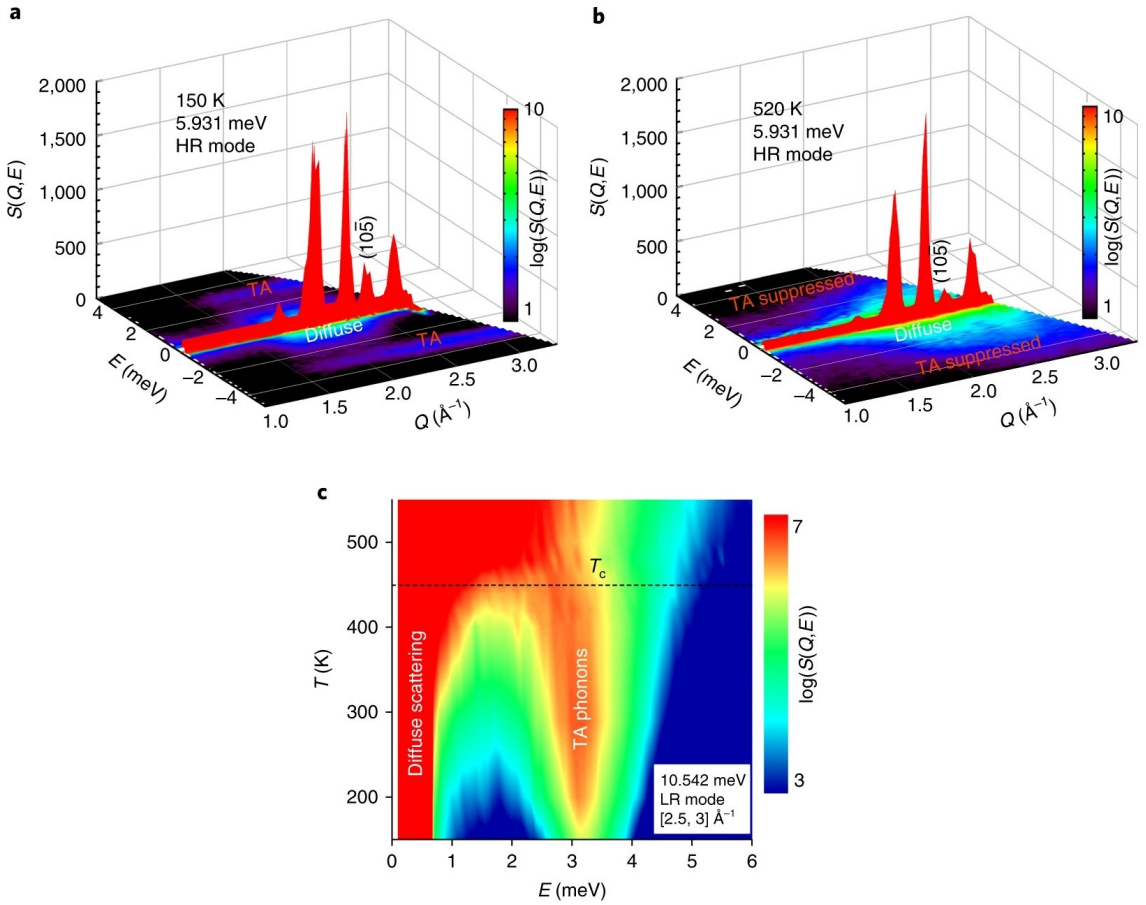

Figure 3.3: **Transverse acoustic phonon modes and QENS in $AgCrSe_2$.** $S(Q, E)$ surface plots at temperature (a) $T = 150\,\mathrm{K}$ and (b) $T = 520\,\mathrm{K}$. (c) Contour plot of $S(Q, E)$ as a function of energy and temperature, integrated over $2.5 - 3\,\mathrm{Å}^{-1}$ [14].

investigation of phonon modes at certain points in reciprocal space, whereas powder averaged data is dominated by the signal at the zone boundary. Much like the data of Li *et al.*, the polycrystalline INS spectra show a QENS signal which in the superionic phase broadens and merges with the non-dispersive TA phonons, see Fig. 3.4. More importantly, Fig. 3.4b shows dispersive TA phonons as vertical streaks which persist into the superionic phase, particularly at $Q = 3.3\,\text{Å}^{-1}$ [15].

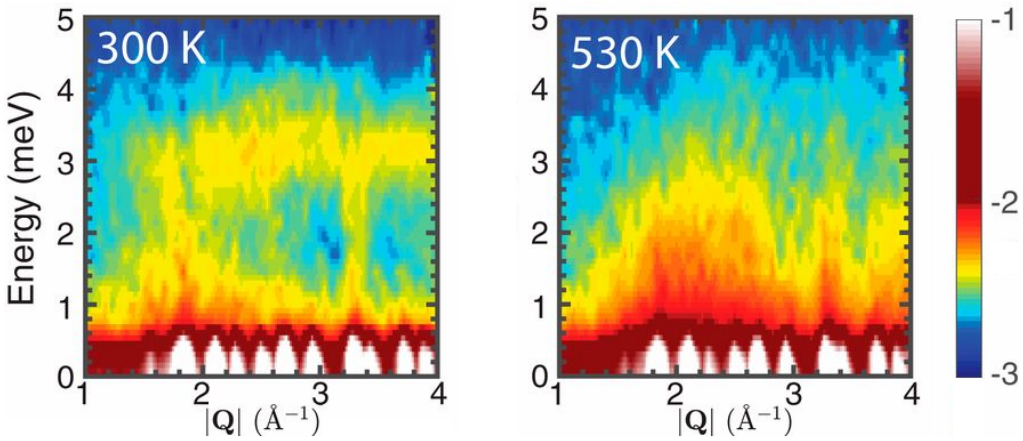

Figure 3.4: **Polycrystalline INS spectra from $AgCrSe_2$.** (a) At $T < T_{OD}$, a broad QENS develops around $Q = 2\,\text{Å}^{-1}$, and the non-dispersive TA phonons appear as a flat band around 3 meV. (b) At $T > T_{OD}$, the QENS signal further broadens and merges with the non-dispersive TA phonons. The vertical streaks which represent the dispersive acoustic phonons remain intact even in the superionic phase [15].

The single crystal IXS data further evidences the selective breakdown of TA phonons. Fig. 3.5a shows the temperature dependence of TA phonons at the zone boundary, $Q = 0, 1.5, 0$ (rlu). At $T < T_{OD}$, the spectrum is well described by an over-damped harmonic oscillator (DHO) profile that is represented by the solid lines in the figure. In the superionic phase, the short-wavelength non-dispersive TA phonons

at the zone boundary become extremely damped, with no observable phonon peak at $T = 560\,\mathrm{K}$. In contrast, it is clear from Fig. 3.5b that long-wavelength dispersive TA phonons at $Q = 0.9, 0.95, 0$ continue to exists well into the superionic phase, with the presence of a well-defined phonon peak even at 560 K. The same behaviour was also observed along the $[1, 0, L]$ and $[-2 + H, 1, 0]$ directions. Hence, this study suggests that all modes of heat propagation persist into the superionic regime despite the presence of broad QENS [15].

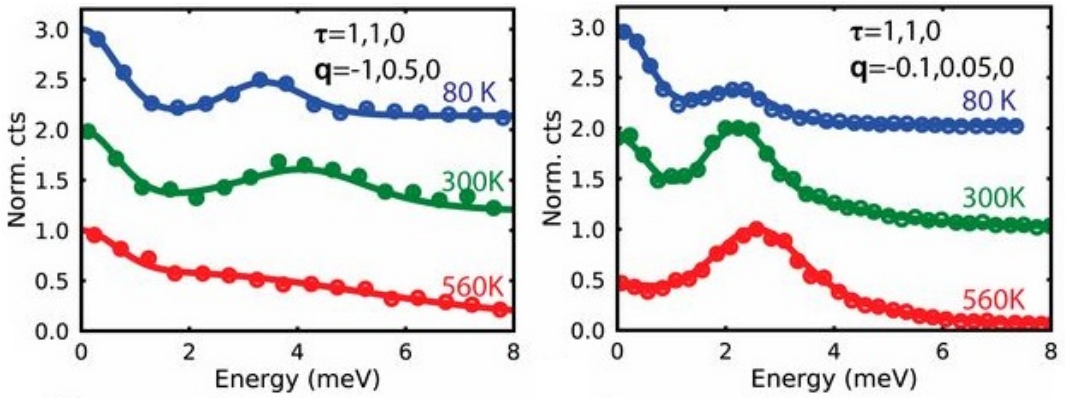

(a) (b)

Figure 3.5: **Temperature dependent IXS spectra of $AgCrSe_2$ at specific Q in rlu**. (a) $Q = (0, 1.5, 0)$. (b) $Q = (0.9, 0.95, 0)$. Data are represented by markers, with corresponding DHO fits as solid lines [15].

Meanwhile, a recent QENS study of $CuCrSe_2$ observed much slower diffusion and found that TA phonons persist in the superionic phase at $T = 495\,\mathrm{K}$. A mean residence time of $\sim 7\,\mathrm{ps}$ was reported for Cu ions in the superionic phase, which is significantly greater than the typical period of $\sim 1\,\mathrm{ps}$ for TA phonons [16]. This value of τ is much slower than those reported by both previous studies of $AgCrSe_2$ [14,15]. Such a significant difference is unexpected given the fundamentally similar properties and almost identical crystal structure of the two compounds. This value of τ bring

into question the validity of the PLEC concept in $CuCrSe_2$.

Further investigation is necessary to resolve the conflict over the validity of the PLEC concept in superionic $M CrSe_2$ (M = Ag, Cu). Investigating the dynamics in these layered compounds using unpolarised neutron scattering is challenging, and could be the underlying reason for the contradictory findings. In neutron scattering the total signal has contributions from three different sources of scattering. Each probe a different aspect of the system and can give rise to similar looking experimental signatures that cannot be isolated in an unpolarised neutron scattering experiment.

Neutrons can interact with a system through the strong nuclear force, or with unpaired electrons in magnetic systems [7]. Scattering from the nucleus can either be coherent or incoherent due to isotopic mixing or the nuclear spin. Coherent scattering gives information on the crystal structure through Bragg peaks and diffuse scattering, and phonons through inelastic scattering [110]. Information on the phonon-density-of-states and single particle dynamics is gained from incoherent scattering, which enables self diffusion to be probed through QENS [111]. Hence, this is the most relevant component to the study of atomic residence times in $AgCrSe_2$. However, short-range structural correlations with a finite lifetime can also lead to a QENS-like coherent scattering signal [112].

The unpolarised QENS in $CuCrSe_2$ reported by Niedziela *et al.* [16] demonstrates the challenges introduced by the inability to separate each scattering contribution. The spectra shown in Fig. 3.6 were interpreted as arising from incoherent scattering from diffusing ions, and used to determine the mean residence time of Ag ions. In this data, the integrated intensity at $Q = 2.2\,\text{Å}^{-1}$ is significantly larger in comparison to that at $Q = 1.1\,\text{Å}^{-1}$. However, for incoherent scattering the Debye-Waller factor

predicts a decrease in the integrated intensity with increasing Q. Hence, this suggests that the data used to estimate the residence time may be contaminated with coherent scattering signal.

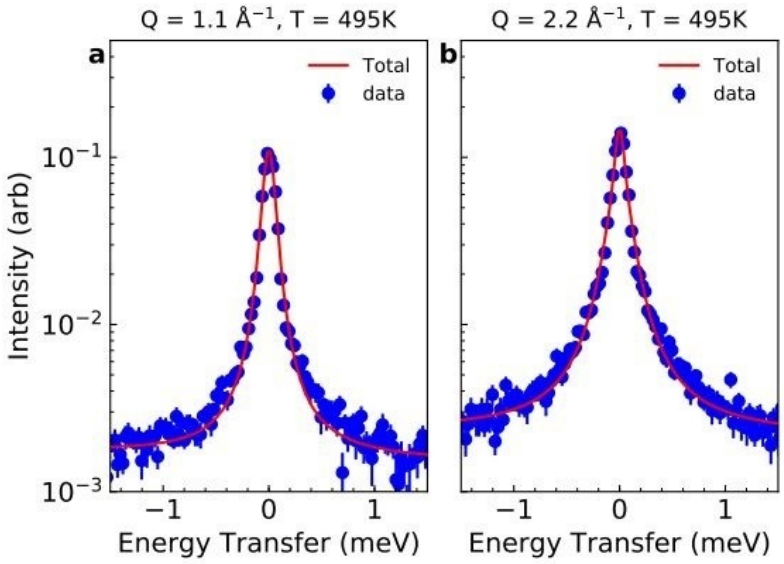

Figure 3.6: **Unpolarised QENS spectra of $CuCrSe_2$.** Energy transfer measured at $T = 495\,\mathrm{K}$ over (a) $1.0 \leq Q \leq 1.2\,\mathrm{Å}^{-1}$ and (b) $2.15 \leq Q \leq 2.25\,\mathrm{Å}^{-1}$. Data points shown in blue with representative Lorentzian fits shown in red [16].

For magnetic systems such as $AgCrSe_2$, it is also import to consider the magnetic scattering. This adds another level of complication, and increases the potential to misinterpret the origin of signals in an unpolarised neutron scattering data set. Below the ordering temperature, this gives information on the magnetic structure and spin-waves. Above the ordering temperature, magnetic scattering can also present as a quasi-elastic signal that gives information on the residual magnetic correlations [113, 114].

It is important to consider and be able to isolate each of these scattering components in $AgCrSe_2$. The technique of polarised neutron scattering alleviates the

problems discussed above by enabling separation of each contribution. Hence, both the origin of the reported QENS signal and the ionic residence times can be investigated with greater certainty.

3.1.1 Magnetism in $AgCrSe_2$

The Néel temperature, T_N of $AgCrSe_2$ is 55 K, below which the Cr^{3+} spins magnetically order with a propagation vector $\mathbf{k} = (\epsilon, \epsilon, 3/2)$, where $\epsilon \sim 0.038(2)$). Fig. 3.7 shows the corresponding long range spiral magnetic structure which is stacked antiferromagnetically along the *c*-direction, with the Cr spins confined to the *ab* plane [17, 115].

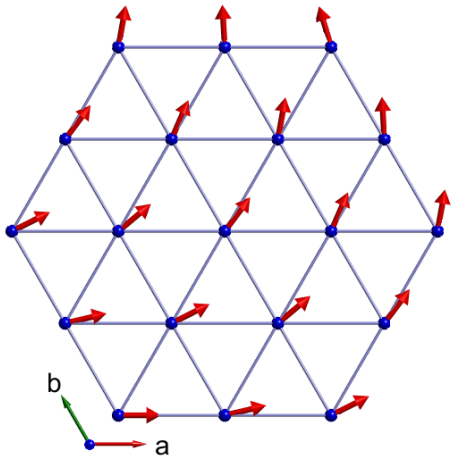

Figure 3.7: **Magnetic structure of $AgCrSe_2$.** Below T_N = 55 K, the Cr layer adopts a long range ordered spiral magnetic structure with antiferromagnetic coupling between the layers [17].

An INS study by Damay *et al.* investigated the dynamics in $AgCrSe_2$ between 10-200 K and constructed a spin Hamiltonian by simulating the data [18]. In the magnetically ordered phase, a dispersive spin-wave excitation is observed at $T = 2$ K, originating from the magnetic Bragg peaks at $Q \sim 0.5$ Å^{-1}, as shown in Fig. 3.8a.

This signal is estimated to extend up to $\sim 30\,\text{meV}$, with a mode having a maximum around $20\,\text{meV}$. Another strongly dispersive magnetic signal is observed at $Q \sim 2\,\text{Å}^{-1}$, with a strong intensity below $2\,\text{meV}$. Measurements above T_N show that 2D dispersive magnetic excitations persist well into the paramagnetic phase, up to $T \sim 200\,\text{K}$.

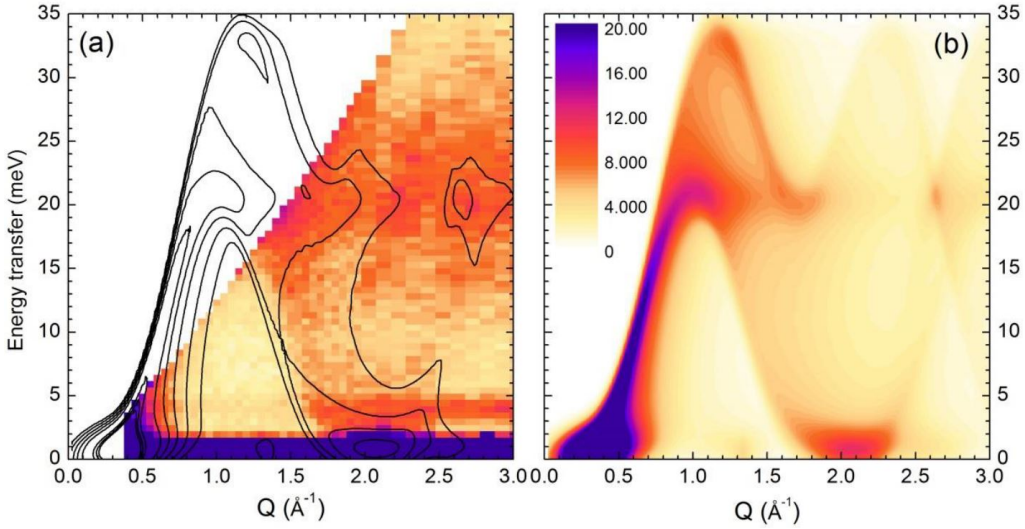

Figure 3.8: **Modelling the magnetic structure of $\mathbf{AgCrSe_2}$ at** $T = 2\,\text{K}$. (a) INS data from powder sample with spin-wave calculation represented by black lines. (b) Simulated spin-wave spectrum using $J_N \sim -2.1\,\text{meV}$, $J_{NN} \sim 0.71\,\text{meV}$ and $J_c \sim 0.09\,\text{meV}$ [18]. Values quoted using SpinW convention of a negative value corresponding to a ferromagnetic interaction [19].

Spin-wave simulations were performed using a Hamiltonian with nearest (J_N) and next-nearest (J_{NN}) neighbour interactions within the *ab* plane, with a coupling J_c between nearest neighbours in adjacent layers. Fig. 3.8b shows the spectrum simulated using a ferromagnetic $J_N \sim -2.1\,\text{meV}$ and two antiferromagnetic exchanges $J_{NN} \sim 0.71\,\text{meV}$ and $J_c \sim 0.09\,\text{meV}$. The J_c parameter was found to directly influence the maximum of the mode at $Q \sim 1.2\,\text{Å}^{-1}$ [18].

These exchange values perform well in reproducing the high energy excitations

with energy scales estimated from the data. However, the low resolution and limited coverage of the experimental spectrum introduces great uncertainty in the energy scales of these modes. The majority of the high energy mode at $Q \sim 1.2\,\text{Å}^{-1}$ is outside the coverage of these measurements, and the low energy modes are very challenging to resolve. Hence, the accuracy of the spin Hamiltonian may be improved using better quality data to base the simulations on.

3.2 Experimental procedure

Unpolarised INS and *xyz*-polarised QENS experiments were performed on the LET spectrometer at ISIS [9] and the ThALES spectrometer at the Institute Laue-Langevin [116], respectively. Additional INS was performed on the MAPS spectrometer at ISIS [8] to investigate the high energy magnetic excitations. All experiments were performed on the same batch of polycrystalline sample. This section details the sample preparation and characterisation, the experimental conditions under which data were collected, and the results of the analyses.

3.2.1 X-ray diffraction

Polycrystalline sample of $AgCrSe_2$ was synthesised by Dr Uthayakumar Sivaperumal and Dr Robin Perry following the method detailed in Ref. [14]. The purity of the sample was checked with the help of Dr Dan Nye using a Rigaku Smartlab, a high resolution powder x-ray diffractometer (XRD) at the ISIS Materials Characterisation Laboratory. An aluminium watch-cell sample holder with a silicon base was used to ensure minimal background signal during measurements. The sample is spread over the base of the holder, then a uniform surface is obtained by gently pressing down

with a glass slide. The sample holder was then loaded into the diffractometer and measured using a copper source for 12 hours at room temperature over $5 - 154^\circ$ in 2θ.

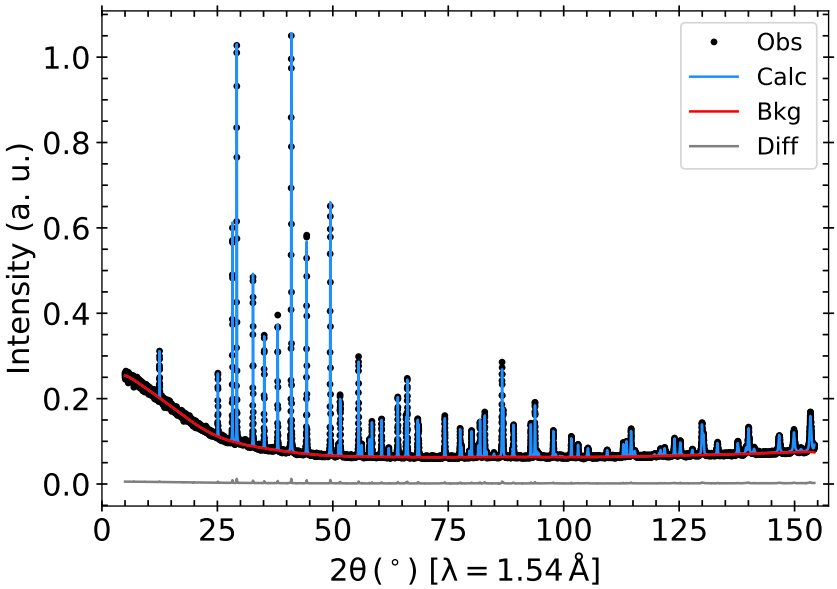

Figure 3.9: **Le Bail refinement of powder XRD from the $AgCrSe_2$ sample at room temperature using a Cu source.** Experimental data are shown as black filled circles. The calculated intensity of Bragg reflections is shown in blue while the difference between the experimental data and the calculation is shown in grey. The red curve is a fit of the background signal.

The measured powder diffraction pattern and Le Bail refinement results are presented in Fig. 3.9. Refinement performed using the `Jana2006` software shows that all of the reflections in the measurement are indexed by the expected $AgCrSe_2$ Bragg peaks at room temperature, thus confirming the phase purity of the sample. Rietveld refinement of the data was attempted but unsuccessful due to texturing in the sample.

3.2.2 INS on LET

Prior to the measurements on LET the sample was loaded into a thin walled annular aluminium can. This can is then screwed onto the end of the sample stick and lowered into the sample environment of the instrument. Cadmium masking was applied at the top and bottom of the cylindrical can to minimize the background.

Measurements were performed at $5, 150$ and $300\,\mathrm{K}$ using a standard orange cryostat. The "intermediate" aperture on the resolution chopper was used with resolution frequency set to $200\,\mathrm{Hz}$ and pulse remover frequency of $100\,\mathrm{Hz}$, giving a good balance between neutron flux and resolution. An incident energy of $8.9\,\mathrm{meV}$ was used to achieve a resolution of $\sim 0.26\,\mathrm{meV}$ at the elastic line. Additionally, repetition rate multiplication (RRM) was utilised to simultaneously perform measurements with incident energies $E_i = 2, 3.7$ and $45\,\mathrm{meV}$. A proton charge of $240\,\mu\mathrm{Ahr}$ ($1\,\mathrm{hr} = 40\,\mu\mathrm{Ahr}$) was detected at the target during measurements at both 5 and $150\,\mathrm{K}$, whereas a charge of $127\,\mu\mathrm{Ahr}$ was detected for the measurement at $300\,\mathrm{K}$. The data were subsequently reduced and analysed using the Mantid package [117].

3.2.3 INS on MAPS

The sample and sample holder previously used during the LET experiment were used once again. These were cooled to and kept at $6\,\mathrm{K}$ using a CCR. The "sloppy" fermi chopper was employed to maximise neutron flux at the sample. Measurements were performed with incident energies of 60 and $100\,\mathrm{meV}$ using a chopper frequency of $400\,\mathrm{Hz}$, and with $200\,\mathrm{meV}$ at a chopper frequency of $600\,\mathrm{Hz}$. The energy resolutions achieved at the elastic line, shown in Fig. 3.10, are approximately $2.51, 5.90$ and $11.53\,\mathrm{meV}$ for $60, 100$ and $200\,\mathrm{meV}$ respectively. The $60\,\mathrm{meV}$ data set was acquired

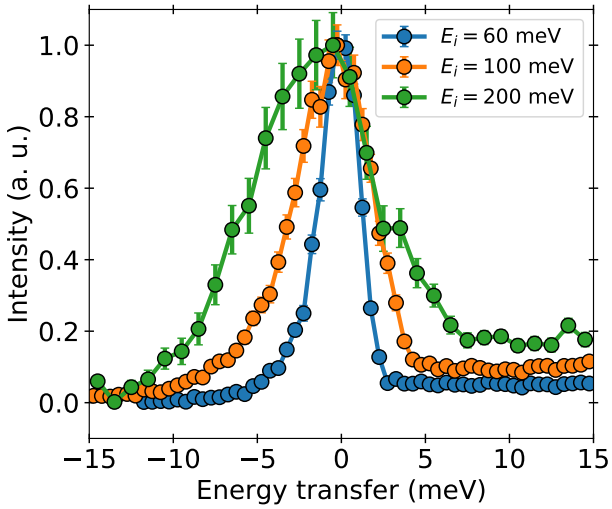

Figure 3.10: **Energy resolution of MAPS at the elastic line.** Energy transfer measured on $AgCrSe_2$ over $1.55 \leq Q \leq 1.65\,\text{Å}^{-1}$ using incident energies of 60, 100 and 200 meV.

with a proton charge of 360 μAhr at the target, 100 meV with 3 times more and 200 meV with 6.25 times more. These were followed by equivalent measurements of the empty sample can to be used for background subtraction. The data were reduced and analysed using the Mantid package [117].

3.2.4 *xyz*-polarised QENS on ThALES

In a standard INS experiment it is very difficult isolate the different scattering components discussed in Section 3.1. Separation can be achieved by employing a polarised neutron beam and analysing the neutron spin state after scattering from the sample, as summarised in Fig. 3.11 for a uniaxial polarisation experiment. A thin walled annular aluminium sample can was loaded with sufficient powder to cover the 3 cm height of the incident beam. ThALES was set up with large focusing Heusler monochromators and analysers at a fixed final energy of 8 meV. A Helmholtz coil

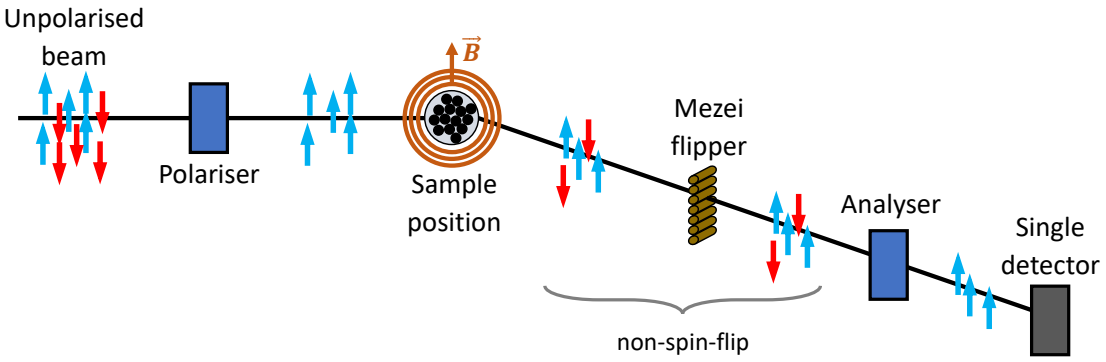

(a)

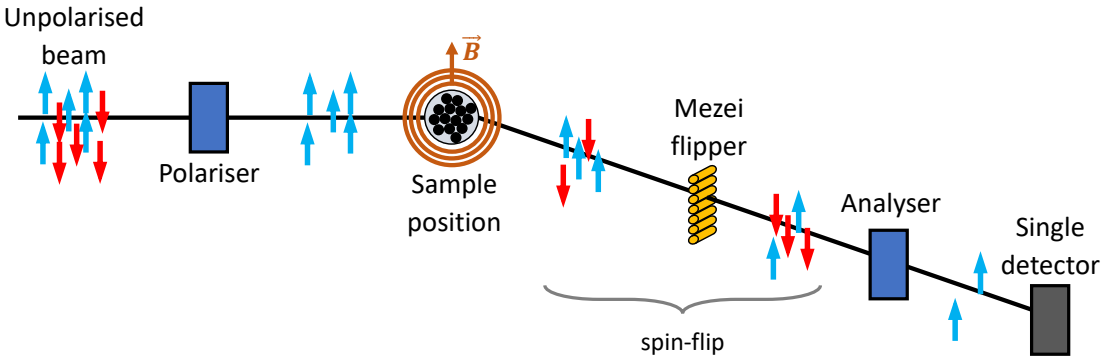

(b)

Figure 3.11: **Schematic view of a uniaxial polarised neutron experiment on a TAS**. From left to right, the unpolarised neutron beam encounters a polariser that reflects only neutrons with their spin oriented along one particular axis towards the sample. At the sample position a Helmholtz coil set reorients the spins along any arbitrary direction before the beam encounters the sample. The neutron spins become mixed after scattering from the sample, and later encounter a Mezei flipper. (a) Mezei flipper is switched off to measure the non-spin-flip scattering. (b) Mezei flipper is switched on to measure the spin-flip scattering. The scattered beam is then reflected by the analyser towards the single detector.

set around the sample generates a uniform magnetic field to orient the incoming neutron spins along any arbitrary direction at the sample position (see Fig. 3.12), and a Mezei flipper is employed to switch between the non-spin-flip and spin-flip channels, as illustrated in Figs. 3.11a and 3.11b respectively. Measurements were performed between 5 and 500 K using a standard orange cryofurnace, which has a maximum attainable temperature of 550 K.

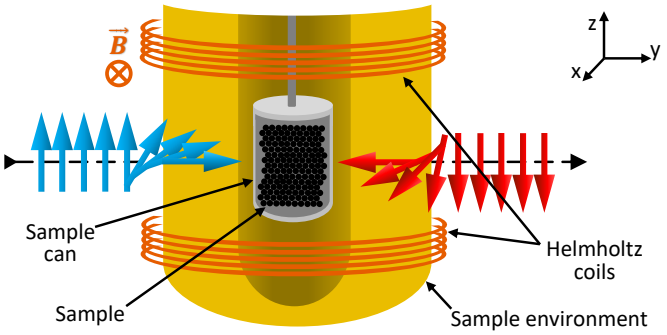

Figure 3.12: **Interaction of a polarised neutron with the sample**. A neutron initially polarised along the z-axis is reoriented using a set of Helmholtz coils to be polarised along the y-axis before scattering from the sample. Here the neutron undergoes a spin-flip interaction with the sample. The spin return to being parallel or anti-parallel to the z-axis upon leaving the uniform field generated by the Helmholtz coils.

The polarisation axes were set up with x parallel to the scattering vector Q and z perpendicular to the scattering plane defined by k_i and k_f. The nuclear (both isotopic incoherent and coherent) (N), magnetic (M) and nuclear spin incoherent (I) scattering are then separated by polarising the incident neutron beam along x, y and z and using combinations of the spin-flip (sf) and non-spin-flip (nsf) scattering

cross sections [84]. In this configuration the six cross section give

$$\begin{aligned} x_{nsf} &= \frac{1}{3}I + N, \\ x_{sf} &= M + \frac{2}{3}I, \\ y_{nsf} &= \frac{1}{2}M + \frac{1}{3}I + N, \\ y_{sf} &= \frac{1}{2}M + \frac{2}{3}I, \\ z_{nsf} &= \frac{1}{2}M + \frac{1}{3}I + N, \\ z_{sf} &= \frac{1}{2}M + \frac{2}{3}I. \end{aligned} \tag{3.1}$$

It is necessary to correct each cross section for the finite polarising efficiencies of the monochromator, analyser and flipper. This requires the measurement of the scattering in these six channels from a quartz sample to obtain for each the ratio of nsf and sf, known as the flipping ratio F. Quartz is a purely nuclear scatterer, hence in an ideal polarised neutron scattering experiment with perfectly polarised beam and perfect analysers there will be no sf scattering [84]. Flipping ratios of $F_x = 22.8(4), F_y = 21.6(4)$ and $F_z = 21.6(4)$ were achieved during this experiment on $AgCrSe_2$. Then, using x as an example, the corrected cross sections are given by

$$\begin{aligned} x_{nsf}^{corr} &= x_{nsf} + \frac{1}{F_x - 1}(x_{nsf} - x_{sf}), \\ x_{sf}^{corr} &= x_{sf} - \frac{1}{F_x - 1}(x_{nsf} - x_{sf}). \end{aligned} \tag{3.2}$$

The quantities in Eq. (3.1) can be combined in different ways to express the M, I and N components of scattering. The expressions used together with the relative duration of each measurement determines the statistical quality of each cross section. All three cross sections were of interest for this experiment, because the objective

was to reveal the origin of the previously reported QENS, hence the cross sections were determined using

$$\begin{aligned} M &= 2x_{sf} - y_{sf} - z_{sf}, \\ I &= \frac{1}{2}(x_{sf} + y_{sf} + z_{sf}) - 2x_{sf} + y_{sf} + z_{sf} \\ &= \frac{2}{3}(-x_{sf} + y_{sf} + z_{sf}), \\ N &= \frac{1}{6}[2(x_{nsf} + y_{nsf} + z_{nsf}) - x_{sf} - y_{sf} - z_{sf}]. \end{aligned} \tag{3.3}$$

The statistical error associated with each cross section determined in this way is then given by

$$\begin{aligned} \delta M &= \sqrt{4(\delta x_{sf})^2 + (\delta y_{sf})^2 + (\delta z_{sf})^2}, \\ \delta I &= \frac{2}{3}\sqrt{(\delta x_{sf})^2 + (\delta y_{sf})^2 + (\delta z_{sf})^2}, \\ \delta N &= \frac{1}{6}\sqrt{4[(\delta x_{nsf})^2 + (\delta y_{nsf})^2 + (\delta z_{nsf})^2] + (\delta x_{sf})^2 + (\delta y_{sf})^2 + (\delta z_{sf})^2}, \end{aligned} \tag{3.4}$$

where $\delta x, \delta y$ and δz are the standard deviations of the x, y and z cross sections respectively, and each is given by the square root of the respective neutron counts. The propagated uncertainties are denoted by $\delta M, \delta I$ and δN. The relative duration of measurements of the six cross sections from Eq. (3.1) were chosen such that similar percentage uncertainties are achieved for M, I and N components to the scattering. All nsf channels were measured for approximately 1 minute each, the y_{sf} and z_{sf} channels for 3 times as long, and the x_{sf} for 12 times as long.

The instrumental resolution function is of particular importance for QENS measurements. It is often determined by the functional form of the scattering from a purely incoherently scattering sample, commonly vanadium, measured with the same

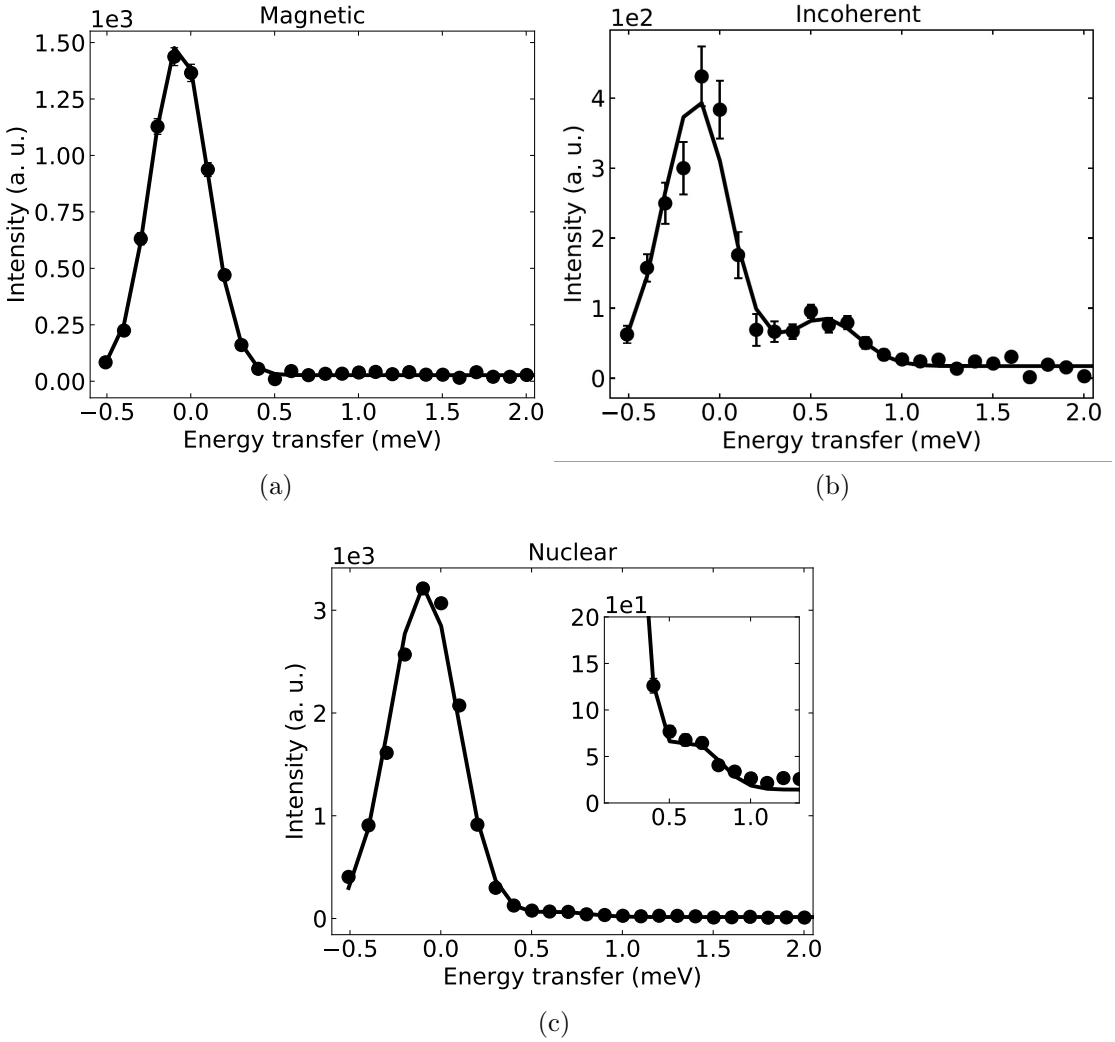

(a) (b)

(c)

Figure 3.13: **Resolution function for each scattering cross section of $AgCrSe_2$ measured at $T = 5\,\mathrm{K}$ on ThALES**. (a) Magnetic cross section. (b) Nuclear spin incoherent cross section. (c) Nuclear cross section, with the inset focusing on the spurious signal at $\sim 0.6\,\mathrm{meV}$. For each cross section the data are represented as dots, and the analytical fit as a solid line.

incident energy as the main measurements. However, for this experiment the vanadium scan was performed at a different value of k_f and was therefore not suitable. Instead, measurements of $AgCrSe_2$ at base temperature of 5 K, shown in Fig. 3.13, were used to define the instrumental resolution for each cross section.

The elastic peak profile on ThALES approximately follows a Gaussian distribution, with the full width at half maximum ($FWHM$) being the energy resolution of the instrument at the elastic line. For the magnetic cross section the fit in Fig. 3.13a corresponds to an energy resolution of 0.401(7) meV. On the other hand, an additional Gaussian term was included in the fit functions for the nuclear spin incoherent and nuclear cross sections due to the presence of spurious scattering at ~ 0.6 meV. Elastic energy resolutions of 0.43(3) meV and 0.442(9) meV were determined for the nuclear spin incoherent and nuclear cross sections respectively.

3.3 Results & Discussion

3.3.1 Unpolarised INS

The unpolarised inelastic neutron scattering data acquired on LET with $E_i = 8.9$ meV is shown in Fig. 3.14. In the magnetically ordered phase at $T = 5$ K there is strong dispersive scattering at $|Q| = 0.5\,\text{Å}^{-1}$, which broadens significantly at elevated temperatures. Furthermore, this signal becomes weaker at $|Q| = 2.0\,\text{Å}^{-1}$. Long range spin waves at $T < T_N$ present as sharp excitations, whereas above T_N they become short range spin correlations that scatter diffusely. Additionally, the magnetic form factor for neutron scattering drops off with increasing Q. Hence, this strong dispersive signal is likely magnetic in origin.

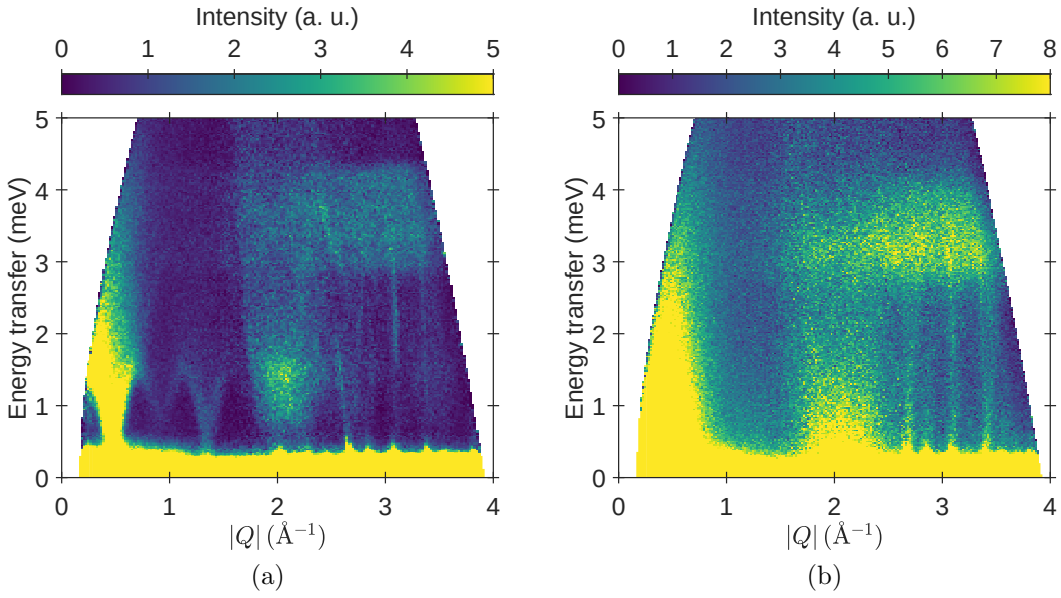

Figure 3.14: **Multi-detector unpolarised data acquired on LET with an incident energy of** 8.9 meV. (a) Data acquired in the magnetically ordered phase at $T = 5$ K. (b) Data acquired at 150 K, above T_N but far below T_{OD}. Several of the sharp features become diffuse at higher temperature, with significant additional scattering around $|Q| \sim 2\,\text{Å}^{-1}$.

Another prominent component both above and below T_N is the band of scattering between energy transfer of 3 and 4 meV that consistently becomes more intense as Q and temperature are increased, a characteristic behaviour of phonon modes. Density functional theory calculations and molecular dynamics simulations predict a phonon mode at this energy arising from the in-plane vibrations of the loosely bound silver ions [14, 15, 18].

As the temperature is increased a strong quasi-elastic feature develops around $|Q| = 2\,\text{Å}^{-1}$, where the two signals discussed above overlap. This quasi-elastic feature is consistent with the work of Li *et al.* [14].

3.3.2 Polarised QENS

The polarised data enables each of the constituent cross sections of the QENS signal shown in Fig. 3.15 to be studied individually. It is well established that Ag exhibits both nuclear spin incoherent and isotopic incoherent scattering [118], hence scattering arising from diffusing Ag ions would present as quasi-elastic energy broadening in the nuclear spin incoherent and nuclear cross sections with equal widths. However, neither of these cross sections show evidence of quasi-elastic energy broadening at $T = 150\,\text{K}$, and the data is well described by the instrumental resolution function used to fit the data at 5 K. For $T_N < T < T_{OD}$ it is evident from Fig. 3.15c that the diffusive scattering previously attributed to ionic diffusion instead arises from the magnetic cross section. The data is well described by convolving the resolution Gaussian and a Loretnzian function with a half width at half maximum $\Gamma = 0.9(3)\,\text{meV}$. This is comparable to widths reported by unpolarised QENS from $AgCrSe_2$ [14], hence the QENS signal in the normal phase is dominated by spin fluctuations rather

than ionic diffusion.

Both the nuclear and nuclear spin incoherent cross sections exhibit additional unexpected scattering around $\sim 0.6\,\mathrm{meV}$ in energy transfer throughout the temperature range studied here. This signal is not present in the unpolarised LET data collected on the same sample, shown in Fig. 3.14, and therefore must be non-magnetic scattering from the sample environment. It was quantified in the analysis by an additional Gaussian term, with a width not changing from that at $T = 5\,\mathrm{K}$.

In the superionic phase, at $T > T_{OD}$, there is a strong enhancement of the QENS signal. The energy broadening in the magnetic cross sections increases to $\Gamma = 1.3(5)\,\mathrm{meV}$, but its contribution to the total scattering is reduced. The nuclear spin incoherent cross section exhibits a drop in the elastic intensity accompanied by an increase in the background level, all of which is consistent with the increasing population of the phonon-density-of-states. Rescaling the resolution function from $T = 5\,\mathrm{K}$ gives a good description of the nuclear spin incoherent data in the superionic phase. However, the goodness of fit is marginally improved with the addition of a Lorentzian broadening term with $\Gamma = 0.08(3)\,\mathrm{meV}$. Interestingly, the enhancement is dominated by a contribution from the nuclear cross section with $\Gamma = 0.5(1)\,\mathrm{meV}$.

The mean residence time (τ) of ions on a lattice site is related to Γ through the Chudley-Elliot model of jump diffusion [91]

$$\Gamma(Q) = \frac{\hbar}{\tau}\left(1 - \frac{\sin(Ql)}{Ql}\right), \tag{3.5}$$

where for $AgCrSe_2$ the tetrahedral hop length l of Ag ions from an α site to a β site is $\sim 2.12\,\text{Å}$ [17]. The broadening observed in the nuclear spin incoherent cross section corresponds to a lower bound on the mean residence time of $\tau \sim 8\,\mathrm{ps}$. This value is

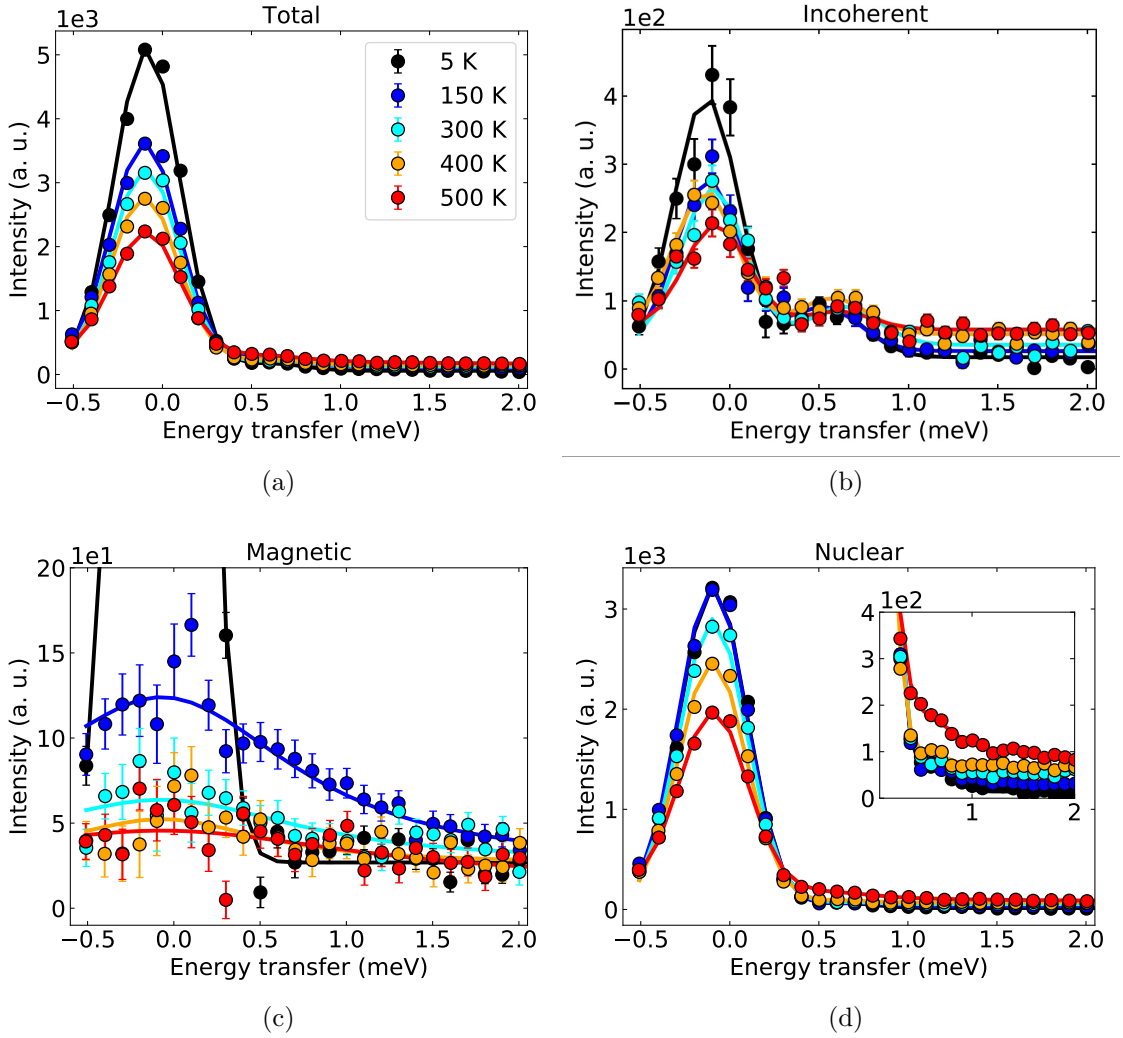

Figure 3.15: **Total and individual scattering cross sections measured at $|Q| = 2.16\,\text{Å}^{-1}$ on ThALES.** (a) The total neutron scattering cross section with the combined fits overlaid. (b) The nuclear spin incoherent cross section. All of the higher temperature data are fitted by scaling the fit of data at 5 K. The small peak at $\sim 0.6\,\text{meV}$ is spurious scattering, most likely from the sample environment as it does not appear in the LET data. (c) The magnetic cross section. All data sets have been fitted by convolving the 5 K fit with a Lorentzian. (d) The nuclear cross section. At 150 K the data is fitted by the re-scaled best fit to the 5 K data. An additional Lorentzian is required to describe the data at $T = 500\,\text{K}$.

consistent with simulations which estimated τ to be in the range of $7 - 11\,\mathrm{ps}$ [119]. Additionally, the value of τ for $AgCrSe_2$ is comparable to the value from unpolarised QENS from $CuCrSe_2$ at $T = 495\,\mathrm{K}$, $\tau \sim 7\,\mathrm{ps}$ [16], however it is much slower than that reported by both previous studies of $AgCrSe_2$ [14, 15]. Given that the typical period of transverse acoustic phonons is $\sim 1\,\mathrm{ps}$, a mean residence time of $\sim 8\,\mathrm{ps}$ is too long to affect the phonons.

The enhanced QENS signal in the superionic phase comprises a quasi-elastic component from dynamic disorder with a possible small contribution from broadened phonons. Detailed understanding of the lattice dynamics and diffusion can be gained through inelastic neutron scattering experiments on single crystal samples. However, synthesis of suitably large single crystals of $M CrSe_2$ has not yet been realised.

In contrast, the availability of large single crystals of superionic fluorite compounds has enabled such coherent QENS to be understood in greater detail. Study of the acoustic phonon modes in PbF_2 revealed that the low-temperature behaviour is consistent with the effects of anharmonicity, and that the sudden change in line width in the superionic phase is attributable to the effects of defects in the lattice, with only a slight contribution from diffusion [120]. Coherent QENS in the superionic phases of PbF_2,$SrCl_2$ and CaF_2 arise from dynamic disorder [121]. The diffusion mechanism in $SrCl_2$ has also been studied using incoherent QENS, revealing longer mean residence times of diffusing ions than the characteristic times of dynamic disorder from coherent QENS [122]. Hence, the coherent QENS can be interpreted as arising from lattice distortions caused by diffusing ions.

The drop in thermal conductivity, κ above T_{OD} [13] likely results from scattering of phonons by the defects in $AgCrSe_2$. Although, κ is low at all temperatures and since Ag is fully ordered at low temperature a mechanism other than defect scattering

must be involved. Presence of strong anharmonicity is evidenced by the substantial broadening of the phonon modes far below T_{OD} [15, 18], which is also observed in diffraction studies of the atomic-displacement parameters [107].

3.3.3 INS studies of magnetic excitations

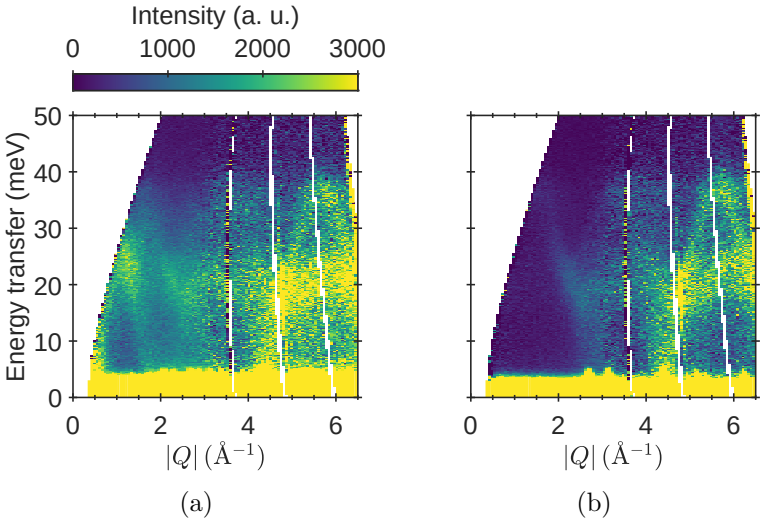

Figure 3.16: **Breakdown of INS data acquired at 6 K on MAPS**. (a) The total signal obtained during measurement of the sample in a aluminium sample can. (b) Signal from independent measurement of an empty aluminium sample can.

It can be very challenging to study high energy spin wave dispersion using neutron scattering, because the magnetic form factor for neutron scattering dictates that magnetic signals are strongest at low values of momentum transfer. Many neutron instruments have a limited coverage of energy transfer in this region. Hence complimentary unpolarised INS experiments were performed on MAPS with $E_i = 100\,\text{meV}$ and LET with $E_i = 8.9\,\text{meV}$. The MAPS data has captured the behaviour of excitations over a large energy and momentum transfer window, whereas the LET data

has sufficiently high resolution to resolve excitations closer to the elastic line.

Distinguishing the scattering from different cross sections is difficult due to a lack of polarisation analysis. Additionally, distinguishing signal from the sample and those from the sample environment is not trivial. The MAPS data shown in Fig. 3.16a has been normalised by the detector efficiency obtained by measuring a vanadium sample. Then the background signal of an empty sample can is subtracted to remove contamination from phonon modes in aluminium, see Fig. 3.16b. This is crucial since the energies of the phonon modes in aluminium coincide with those of spin waves in $AgCrSe_2$. Background from an empty can is not subtracted from the higher resolution LET data since aluminium phonons do not contribute to the signal at the energies probed by this measurement.

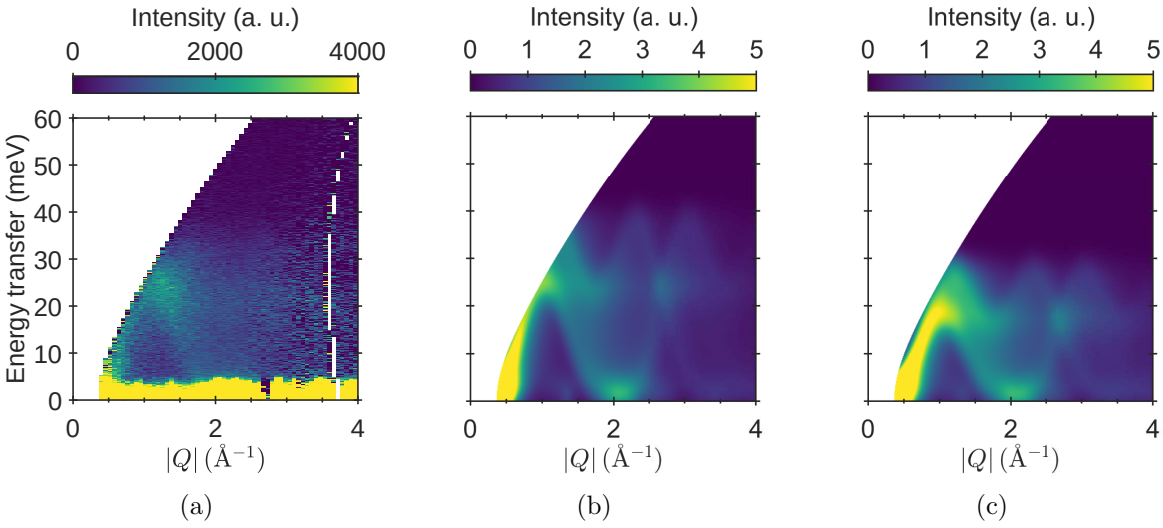

Figure 3.17: **Comparison of experimental and simulated data on high energy magnetic excitations**. (a) Data acquired on MAPS at 6 K with an incident energy of 100 meV. (b) SpinW simulation performed with magnetic exchange couplings quoted in the text. (c) SpinW simulation performed using magnetic exchange couplings quoted by Damay *et al.* [18].

The MAPS data shown in Fig. 3.17a contains multiple features at high energy transfer. A very strong dispersive mode is observed at $Q = 0.5\,\text{Å}^{-1}$, and it extends up to $\sim 25\,\text{meV}$ in energy transfer at $Q \sim 1\,\text{Å}^{-1}$. The intensity of this mode quickly drops at larger Q, suggesting it is likely magnetic in origin. This is further evidenced by the LET data which shows a significant broadening of this mode upon heating above T_N, see Fig. 3.14 on page 110. Additionally, there is very broad scattering extending up to $\sim 30\,\text{meV}$ which is visible even above $2\,\text{Å}^{-1}$. The LET data in Fig. 3.18a reveals a low energy dispersive mode that the MAPS data is unable resolve, with a peak energy of $\sim 1.5\,\text{meV}$ for $Q < 2\,\text{Å}^{-1}$. A very sharp dispersive mode is present above $2\,\text{Å}^{-1}$, and a band of scattering between 3 and 4 meV, both of which are likely phononic in nature based on their Q and temperature dependence.

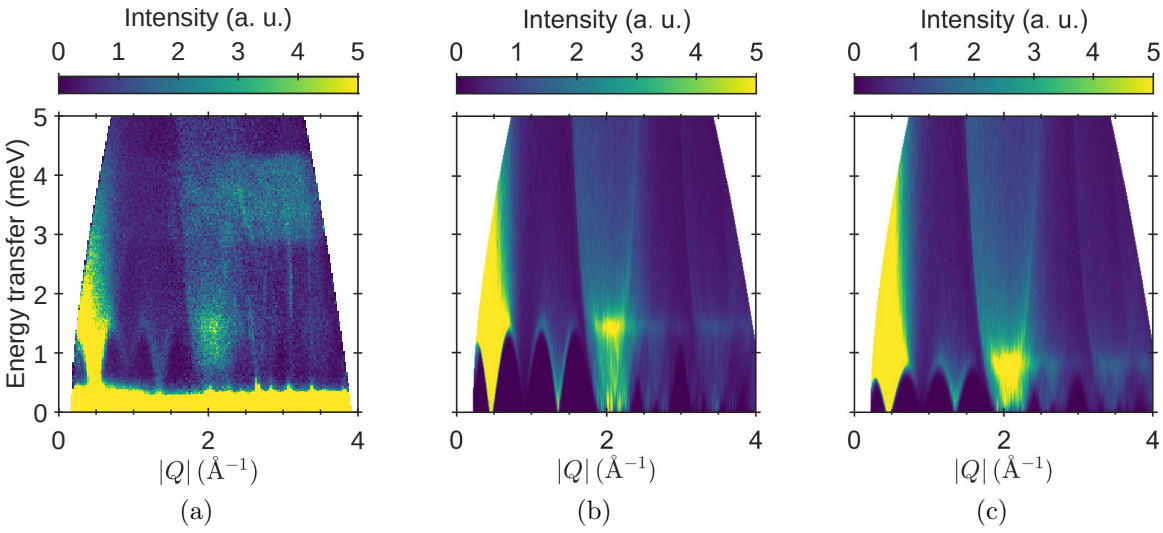

Figure 3.18: **Comparison of experimental and simulated data on low energy magnetic excitations**. (a) Data acquired on LET at 5 K with an incident energy of 8.9 meV. (b) SpinW simulation performed with magnetic exchange couplings quoted in the text. (c) SpinW simulation performed using magnetic exchange couplings quoted by Damay *et al.* [18].

Further insight into the nature of the magnetic interactions in $AgCrSe_2$ can be gained by simulating the magnetic dispersion spectra. Simulations enable determination of the ground state magnetic structure of long-range ordered magnetic systems, for instance through determining the propagation vector and the spin Hamiltonian. In the case of $AgCrSe_2$ the magnetic propagation vector $\mathrm{k} = (\eta, \eta, 3/2)$ ($\eta \sim 0.038(2)$) is well established in literature [17, 18]. In contrast, the spin Hamiltonian has not been studied conclusively.

Simulations of spin wave dispersion spectra were performed using `SpinW`, a `Matlab` library that utilises linear spin wave theory to identify possible magnetic interactions and the corresponding energies [19]. All simulations were performed using the crystal structure at 4 K reported by Engelsman *et al.* [17]. Finite resolution of the instruments were applied to calculations by convolving the signal with different Gaussian functions. A constant energy resolution of 5.6235 meV and Q resolution of $0.12\,\text{Å}^{-1}$ were used to simulate the MAPS data. LET simulations were performed using an energy dependent resolution function obtained from the `PyChop` module within `Mantid` [117], without applying any finite Q resolution.

The magnetic exchange couplings $J_N \sim -2.1, J_{NN} \sim 0.71$ and $J_C \sim 0.09$ meV reported by Damay *et al.* [18] leads to a metastable magnetic structure, with spin wave dispersion spectra as shown in Fig. 3.17c and Fig. 3.18c. It is immediately evident that the energy scales do not agree between the experimental and simulated data, with modes in the simulation consistently having lower energies. Furthermore, applying the kinematic constraints of the MAPS spectrometer to the simulated data makes it apparent that the Q position of the modes in the simulation are not quite right. In the contour plots, this is most obvious around $0.5\,\text{Å}^{-1}$ in Fig. 3.18. Hence, the magnitude of reported exchange couplings need to be optimised. The simulation

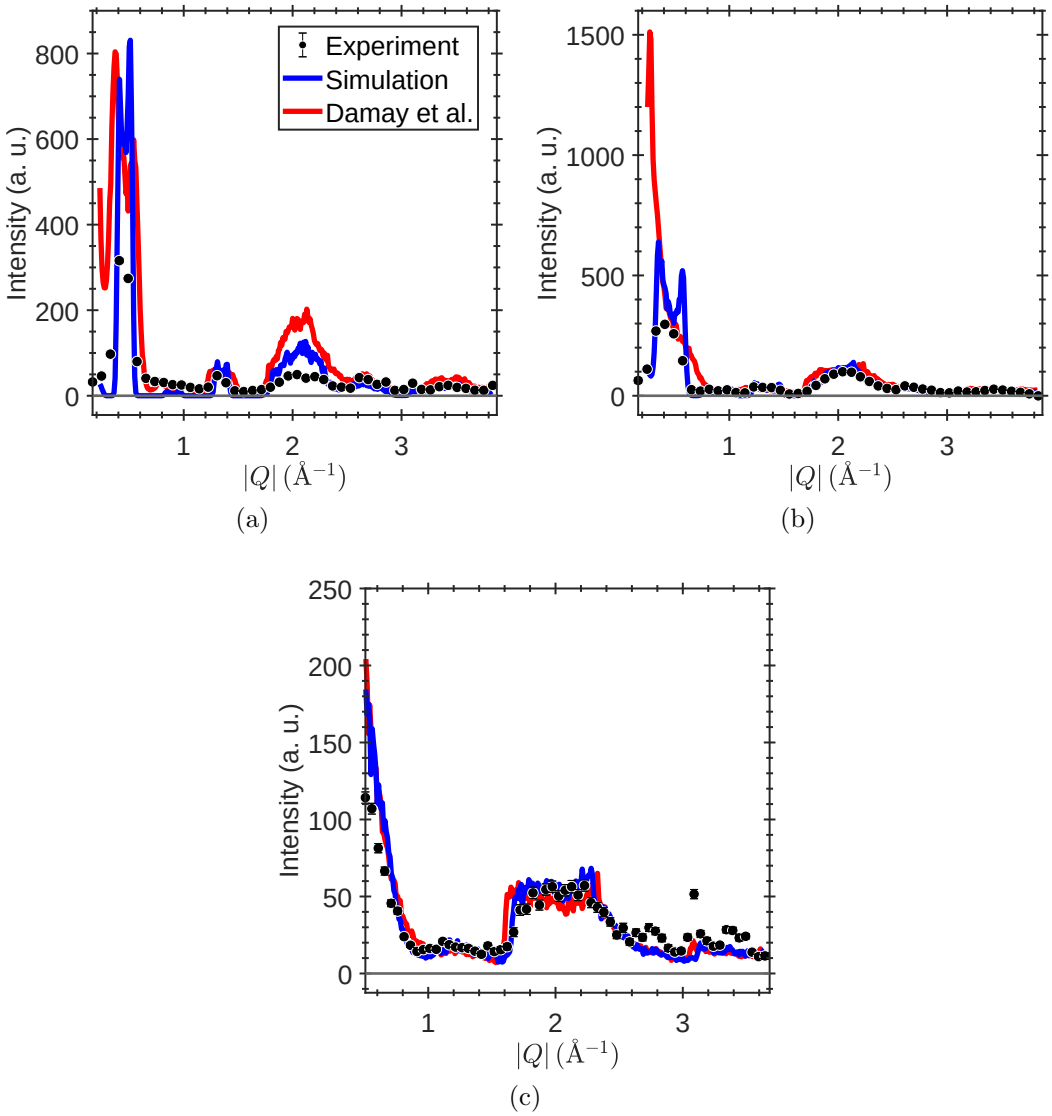

Figure 3.19: **Constant energy line plots comparing the Q positions of low energy excitations observed on LET and simulated with SpinW**. Energy integrations were performed over (a) $0.5 \leq \Delta E \leq 0.7$, (b) $1.0 \leq \Delta E \leq 1.2$ and (c) $2.1 \leq \Delta E \leq 2.3\,\mathrm{meV}$.

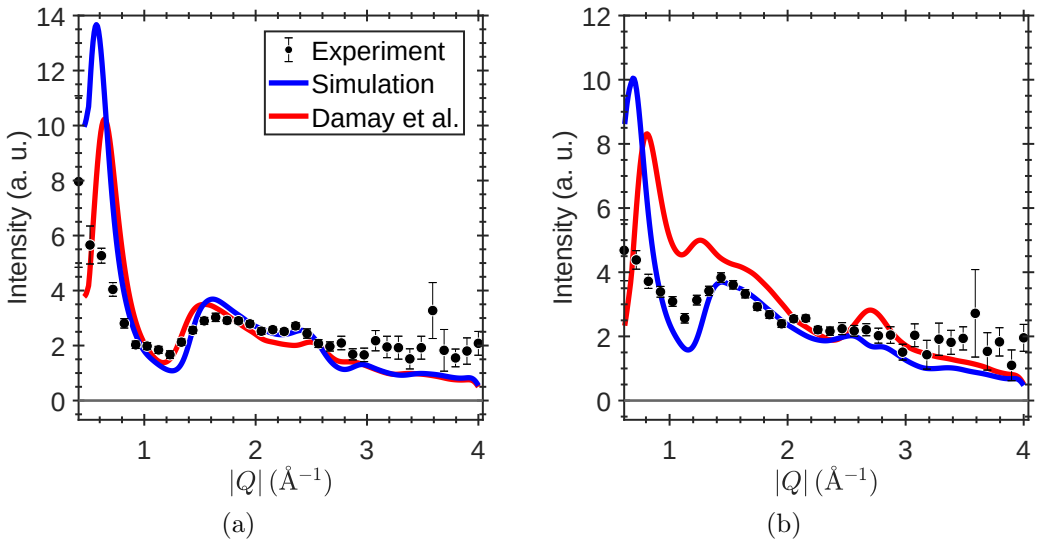

Figure 3.20: **Constant energy line plots comparing the Q positions of high energy excitations observed on MAPS and simulated with SpinW**. Energy integrations were performed over (a) $8 \leq \Delta E \leq 10$ and (b) $14 \leq \Delta E \leq 16$ meV.

does however capture all of the magnetic dynamics that can be resolved from the current data, suggesting that Cr may only interact with up to next-nearest neighbours, but much weaker additional interactions cannot be ruled out.

Magnetic exchange couplings $J_N \sim -2.88(1)$, $J_{NN} \sim 0.99(1)$ and $J_C \sim 0.16(2)$ meV, corresponding to spectra shown in Fig. 3.17b and Fig. 3.18b, were determined using the method of trial and error. Initially, J_{NN} and J_C were fixed at values reported by Damay *et al* while J_N was systematically varied. For each value of J_N the propagation vector optimisation routine `optmagk` was used to check whether the spin Hamiltonian corresponded to the expected propagation vector. Agreement was achieved for $J_N/J_{NN} = 2.9$, however the resulting magnetic excitations were much softer than those experimentally observed. The high energy modes arising from in-plane interactions were hardened using a scaling factor 1.4 to multiply J_N and

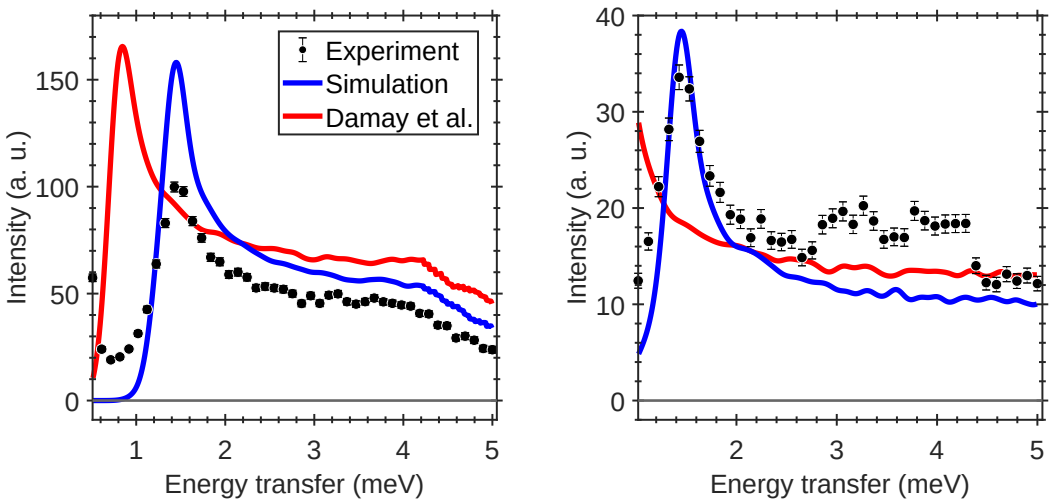

Figure 3.21: **Constant Q line plots comparing low energy excitations observed on LET and simulated with SpinW.** Q integrations were performed over (a) $0.6 \leq Q \leq 0.8$ and (b) $1.0 \leq \Delta E \leq 1.2\,\text{Å}^{-1}$.

J_{NN}, whereas a factor of 1.8 was used for J_C in order to achieve agreement between simulation and LET data.

Figures 3.19 to 3.22 show line plots comparing the experimental observations to simulations performed using both spin Hamiltonians. Figures 3.19 and 3.20 show the Q dependence of scattering intensity at a series of constant energy transfer values, which is useful for checking the Q-position of the excitations. It is apparent from Fig. 3.19 that both simulations successfully identify the position of low energy spin wave modes. On the other hand, the two models differ at higher energies, most notably around $Q \sim 0.5$ and $1.1\,\text{Å}^{-1}$, where the current simulation is a better description of experimental observations, see Fig. 3.20.

The energy scales of excitations can be compared by looking at the energy dependence of scattering intensity at fixed positions in reciprocal space, as shown in

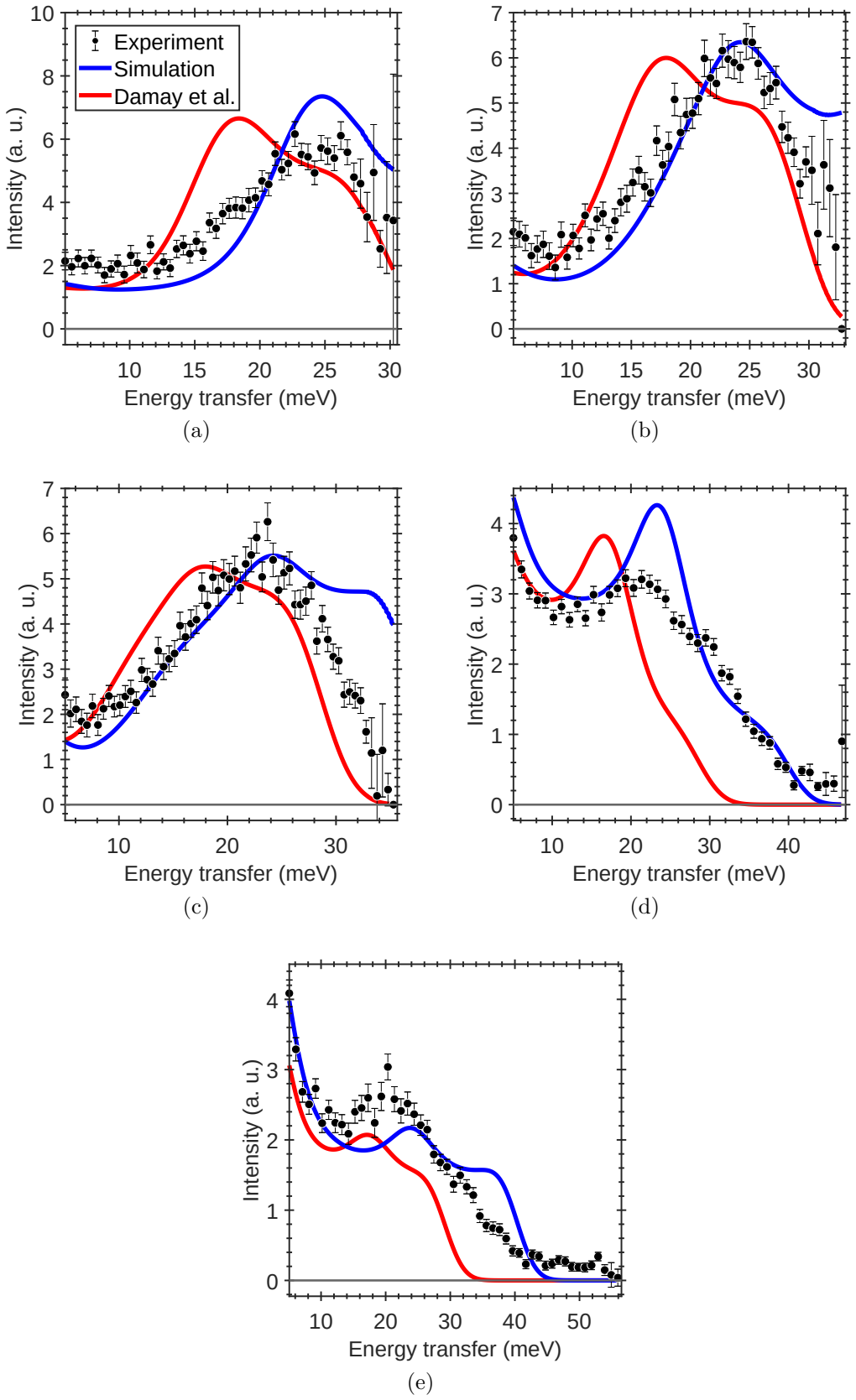

Figure 3.22: **Constant Q line plots comparing high energy excitations observed on MAPS and simulated with SpinW**. Q integrations were performed over (a) $1.1 \leq Q \leq 1.2$, (b) $1.2 \leq Q \leq 1.3$, (c) $1.3 \leq Q \leq 1.4$, (d) $1.7 \leq Q \leq 1.9$ and (e) $2.25 \leq Q \leq 2.35$ Å^{-1}.

Figs. 3.21 and 3.22. In this case the two models vary significantly. At low energies, the present model correctly identifies the modes at $Q = 0.7$ and $1.1\,\text{Å}^{-1}$, whereas the previous model under estimates the energies of those modes. At $Q = 1.1\,\text{Å}^{-1}$, both models deviate from the experimental data between 3 and 4 meV, which corresponds to the band of scattering from Fig. 3.18a that is likely phononic in origin.

Figure 3.22 shows energy scans further out in reciprocal space. In this region the experiment detected a broad mode peaking at ~ 25 meV, and another presenting as a shoulder around 30 meV. The model in the literature predicts modes with peak energies of 20 and 25 meV, whereas the current model predicts peak energies to be 25 and 36 meV. Both models give a poor description of data above $2\,\text{Å}^{-1}$, which may arise from greater phonon intensity combined with much lower magnetic intensity due to the magnetic form factor.

The Hamiltonian reported by Damay *et al.* consistently underestimates the energies of excitations in $AgCrSe_2$. A key difference of that data set is the highly limited energy transfer coverage at low Q, only managing to partially capturing the high energy modes originating from $Q = 0.5$ and $2\,\text{Å}^{-1}$. The peak energies of these modes have not been measured at all. Furthermore, the low energy modes cannot be resolved at all because of the instrumental resolution of ~ 0.5 meV. On the other hand, the Hamiltonian proposed here often performs much better owing to the data that has fully captured and resolved both the high and low energy excitations.

3.4 Conclusions

Polycrystalline neutron scattering was performed to investigate the origin of ultra-low lattice thermal conductivity in $AgCrSe_2$. Previous works used unpolarised neu-

tron scattering to understand the dynamics in $AgCrSe_2$ and reached contradictory conclusions over the validity of the PLEC concept. Here, *xyz* neutron polarisation analysis was employed, enabling each scattering contribution to be studied individually, thereby making it possible to draw unambiguous conclusions about diffusion rates and mechanisms using QENS.

Incoherent QENS from $AgCrSe_2$ shows that the ionic diffusion is not fast enough to suppress the transverse acoustic phonons even in the superionic phase. Therefore, $AgCrSe_2$ does not qualify as a PLEC material and ionic diffusion is not important for the extraordinary thermal properties. Perhaps this bodes well for applications in waste heat recuperation and as Peltier coolers. The results presented here show that it is possible for diffusion to be suppressed without an increase in κ_L.

The unpolarised QENS in the superionic phase previously attributed to incoherent scattering by Li *et al.* [14] is shown to instead arise almost entirely from coherent QENS and damped magnons. It is thought that dynamic defects within the Ag layer give rise to the significant coherent QENS observed. Additional modelling and polarised neutron measurements over a wider Q range are required to resolve the nature of the defect structure.

Moreover, a spin Hamiltonian constructed with one ferromagnetic and two antiferromagnetic exchange couplings is found to reproduce all resolvable magnetic excitations well below T_N at 6 K. Simulations show that the exchange values reported by Damay *et al.* consistently underestimate the energy levels of magnetic excitations, especially those with a maximum below 2 meV. The new exchange values $J_N \sim -2.88(1), J_{NN} \sim 0.99(1)$ and $J_c \sim 0.16(2)$ meV give a significantly better description of the experimental observations.

Chapter 4

Ionic diffusion in $Na_xFe_{1/2}Mn_{1/2}O_2$

4.1 Literature review

The high energy density of Li-ion batteries has lead to their adoption in many aspects of everyday life. Layered lithium transition-metal oxides of the form Li_xMeO_2 (Me = Co, Mn, Ni) have found great commercial success. High capacity and good cycling properties of the prototypical Li-ion cathode Li_xCoO_2 has attracted much interest in its Na analogue Na_xCoO_2. The performance of a battery cathode is ultimately governed by the transport of the ions. Microscopic diffusion pathways and activation energies for ion transport in Na_xCoO_2 have been extensively studied via scattering experiments and computer modelling.

Two very promising polymorphs of layered Na_xCoO_2 are the P2 and O3-type structures. The difference is that NaO_6 polyhedra occupy prismatic (P) or octahedral (O) sites with repetition units in the out-of-plane direction denoted by 2 and

3 [123, 124], see Fig. 4.1. The ABC notation is used to describe the stacking of the three different oxygen layers in Fig. 4.1. The stacking sequence in the P2 structure with space group $P6_3/mmc$ leads to two inequivalent Na sites, Na1 and Na2 (Wyckoff sites 2*b* and 2*d*). In contrast, the O3 structure with space group $R\bar{3}m$ only hosts Na ions on the Na2 site [125, 126].

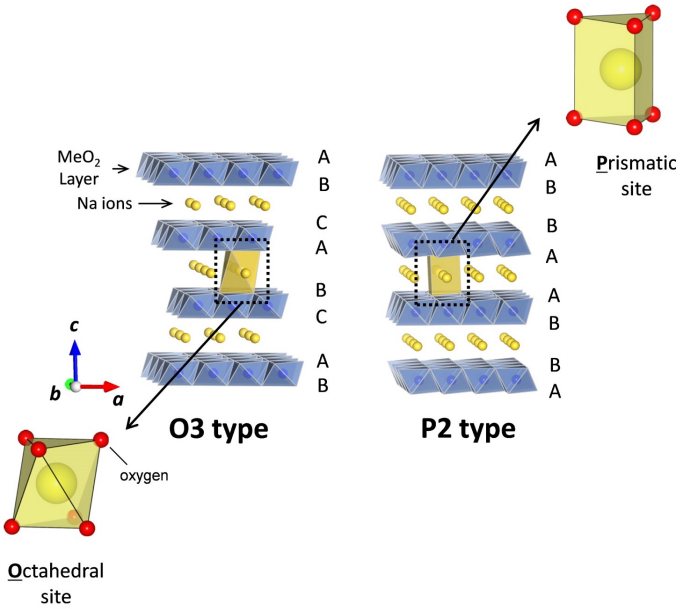

Figure 4.1: **Schematic illustration of P2 and O3-type Na_xMeO_2 structures**. Both are comprised of Na layers surrounded by layers of edge-sharing MeO_6. In the ABC notation the prismatic (P) Na site is surrounded by AA-type stacking of oxygen layers, whereas the octahedral (O) site is surrounded by AB-type stacking of oxygen layers. Adapted from Ref. [20].

A study by Willis *et al.* used x-ray diffraction, neutron spectroscopy and *ab-initio* molecular dynamics (AIMD) simulations to investigate the diffusion mechanism in P2-$Na_{0.8}CoO_2$ [21]. Single-crystal x-ray diffraction data at $T = 100\,\mathrm{K}$ were described by a fully ordered superstructure with stripes of tri-vacancy clusters, as shown in Fig. 4.2a. The Na-vacancies were found to reorder above $\sim 290\,\mathrm{K}$ to the

partially ordered stripe phase in which the tri-vacancy clusters within stripes are no longer correlated between stripes, see Fig. 4.2b. At $\sim 370\,\mathrm{K}$ the sharp superstructure reflections give way to diffuse scattering which was simulated using the Monte Carlo technique to reveal a third phase in which the Na-vacancies adopt a disordered mixture of multi-vacancy clusters, see Fig. 4.2c [21].

First-principles calculations and kinetic Monte Carlo simulations performed by Van der Ven *et al.* revealed that the migration mechanism and activation barriers in Li_xCoO_2 depend strongly on the local arrangement of Li vacancies. Isolated vacancies were found to have high activation barriers, and diffusion is instead mediated by so-called divacancies in the system [127]. Mo *et al.* have shown that O3-Na_xCoO_2 has the same divacancy diffusion mechanism as isostructural Li_xCoO_2 [22]. However, adjacent pairs of vacancies are not stable in P2-Na_xCoO_2, where the promotion of a Na2 ion to a Na1 site instead leads to the formation of the divacancy cluster [128]. Unlike in O3 structures, where diffusing ions hop between regular sites (Na2−Na2), diffusion in the P2 structure is predicted to be dominated by Na2−Na1 hops.

Mo *et al.* further investigated the activation energies (E_A) and diffusion coefficients (D) for various Na concentrations (x) to understand the influence of the different diffusion mechanisms in the P2 and O3 structures. Figure 4.3 shows that partially desodiated P2-Na_xCoO_2 is expected to have lower activation energies and higher diffusion rates compared to the O3 structures [22]. These calculations predict the performance of P2-Na_xCoO_2 to be comparable to that of high performance Li-ion cathodes [129]. It is also predicted that diffusion of Na ions in P2 structures will have greater sensitivity to changes in the local Na environment.

Willis *et al.* investigated the diffusion mechanism in P2-$Na_{0.8}CoO_2$ via QENS.

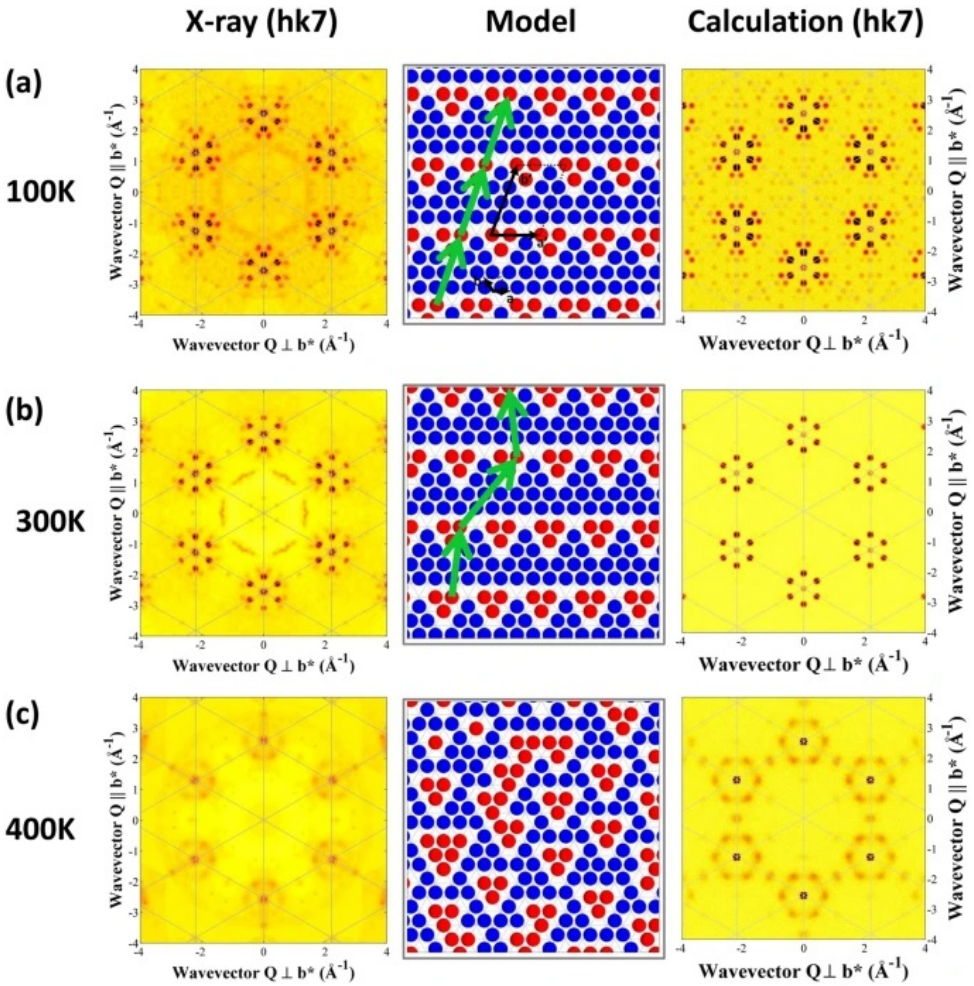

Figure 4.2: **X-ray diffraction measurements and computer simulations of sodium ordering in $Na_{0.8}CoO_2$.** (a) Sharp superlattice reflections in the fully ordered tri-vacancy stripe phase which has highly correlated tri-vacancy clusters. A tri-vacancy cluster is formed when three Na-ion vacancies enable three N -ions on Na2 (blue) sites to be promoted to Na1 (red) sites. (b) Partially disordered tri-vacancy stripe phase in which tri-vacancy clusters between stripes are no longer correlated. (c) The disordered phase with short-range ordering of multi-vacancy clusters gives rise to diffuse scattering [21].

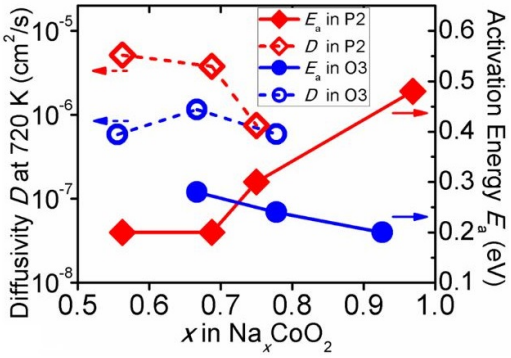

Figure 4.3: **AIMD calculations of diffusion rates and activation energies for P2 and O3-Na_xCoO_2 at different Na concentrations (x).** For any given composition, P2 and O3-Na_xCoO_2 have different diffusion rates and activation energies, and the composition dependence depends on local ordering [22].

The Q dependence of the energy broadening in the dynamic phases show that diffusion is dominated by Na2−Na1 hops, see Fig. 4.4a. At room temperature, 1D diffusion in the partially disordered phase has a diffusion coefficient of $1.4(2) \times 10^{-7}\,\mathrm{cm^2 s^{-1}}$, with an associated activation energy $E_A \sim 170(20)\,\mathrm{meV}$ determined by Arrhenius fitting of the QENS energy broadening, see Fig. 4.4b. In the high-temperature disordered phase there is a transition from 1D to 2D diffusion with a significantly smaller activation energy of $\sim 85(5)\,\mathrm{meV}$ [21].

Room temperature measurements of self-diffusion using the Potentiostatic Intermittent Titration Technique (PITT) are shown in Fig. 4.5. Sudden dips in the diffusion are observed for fractional x, which correspond to the formation of ideal superstructures [24]. This behaviour was interpreted by Willis *et al.* as arising from zero net diffusion in highly ordered superstructures. AIMD simulations of the highly ordered superstructures predict only local hopping of Na ions back and forth between neighbouring sites, giving a correlation factor $f \sim 0$. Away from ideal stoichiometry for superstructures the bulk diffusion coefficient of $1.2(5) \times 10^{-7}\,\mathrm{cm^2 s^{-1}}$ corresponds

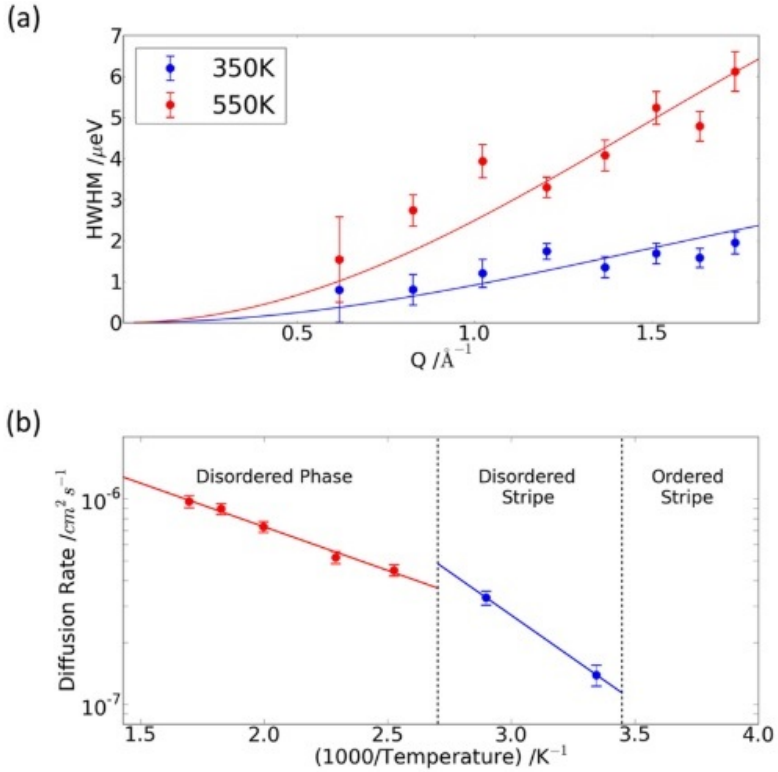

Figure 4.4: **Jump diffusion models for P2-$Na_{0.8}CoO_2$**. (a) Q-dependent QENS measurements in the fully disordered phase (red) and the partially disordered stripe phase (blue) are described by the Chudley-Elliott model of jump diffusion for Na2−Na1 hops represented by the solid lines. (b) Arrhenius plots of diffusion coefficients in the disordered and partially disordered stripe phase give $E_A \sim 85(5)$ meV and 170 meV, respectively [21]. No diffusion is detected in the QENS measurements of the fully ordered stripe phase.

to $f = 0.9(4)$. Hence, the addition of disorder enables multiple hops leading to translational diffusion [21].

The results discussed above demonstrate the potential of layered sodium transition-metal oxides as commercially viable cathode materials in secondary batteries. Typically, reversible capacity of Na-ion cathode materials is limited to $100\,\mathrm{mAhg}^{-1}$. However, P2-$Na_xFe_{1/2}Mn_{1/2}O_2$ has outstanding reversible capacity, $190\,\mathrm{mAhg}^{-1}$, which corresponds to $\sim 72\,\%$ of the theoretical capacity [20]. The energy density is estimated to be $520\,\mathrm{mWhg}^{-1}$, which is comparable to $LiFePO_4$ and higher than $LiMn_2O_4$. A comparison of reversible capacity and operating voltage ranges for various layered Na insertion materials is provided in Fig. 1.1. This shows that P2-$Na_xFe_{1/2}Mn_{1/2}O_2$ has the most promising performance of any of the Na insertion materials and even outperforms these two widely adopted Li-ion materials. Most importantly, $Na_xFe_{1/2}Mn_{1/2}O_2$ is composed entirely of earth-abundant elements, thereby removing concerns over supply and cost typically associated with Li-ion based alternatives [130, 131].

To date there have been x-ray diffraction studies of the stacking sequence as a function of sodium composition, but no studies of the ordering of Na ions within planes. Whether disorder within the transition-metal plane suppresses superlattice formation within the Na layers is an open question. Furthermore, there have been no previous QENS studies of the Na-ion diffusion mechanism. This chapter details x-ray and neutron scattering experiments performed on $Na_xFe_{1/2}Mn_{1/2}O_2$ to understand how the disorder within the transition-metal planes influences superlattice formation and ionic diffusion.

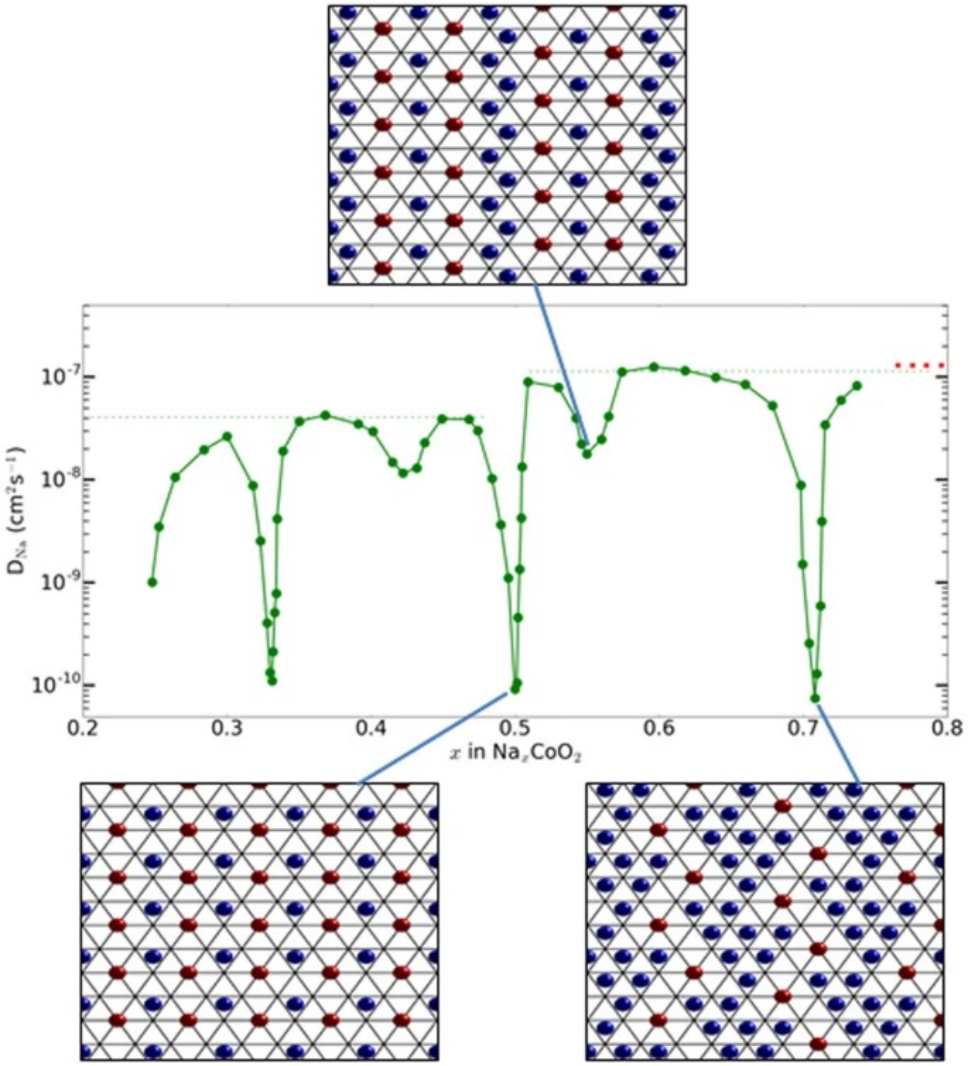

Figure 4.5: x **dependence of bulk diffusion in P2-Na$_x$CoO$_2$.** Ambient temperature PITT measurements show sudden dips in the diffusion rate at value of x ideal for superstructure formation, shown here for $x = 1/2, 5/9$ and $5/7$ [21, 23, 24].

4.2 Experimental procedure

4.2.1 Polycrystalline XRD

Polycrystalline samples of $Na_{0.67}Fe_{1/2}Mn_{1/2}O_2$ and $Na_1Fe_{1/2}Mn_{1/2}O_2$ were synthesised by Dr. Sivaperumal Uthayakumar following Ref. [1], and checked with powder X-ray diffraction (PXRD) using the Xcalibur diffractometer, see Fig. 2.12. To perform PXRD, the tip of a fine glass capillary is first coated with a thin layer of silicone gel to act as an adhesive, then with the sample. The sample is then mounted on the goniometer to be measured in transmission mode. Mo Kα radiation was used to generate monochromatic X-rays ($\lambda = 0.71\,\text{Å}$) by accelerating electrons across a potential difference of $\sim 50\,\text{keV}$ before striking the Mo target [102]. The signal at the CCD camera area detector was processed in the CrysAlis$^{\text{Pro}}$ software, and analysed using custom python scripts.

Room temperature measurements were performed in ambient atmosphere before and after neutron spectroscopy on LET. The grey curves in Fig. 4.6 show that pure phases of each composition were synthesised, with all observed reflections labelled by the expected pattern from these systems. These diffraction patterns are consistent with the PXRD data reported by Yabuuchi *et al.* [1]. Both samples are susceptible to uptake of hydrogen from the atmosphere, which leads to a shift in the position of the (002) and (003) reflections. However, PXRD performed after neutron scattering shows that both samples remain unchanged. It is worth noting that differences in intensities between the before and after data may be explained by variations in measurement duration and the amount of sample in the beam. Furthermore, the background signal is dependent on the silicone on the capillary, and the ambient atmosphere.

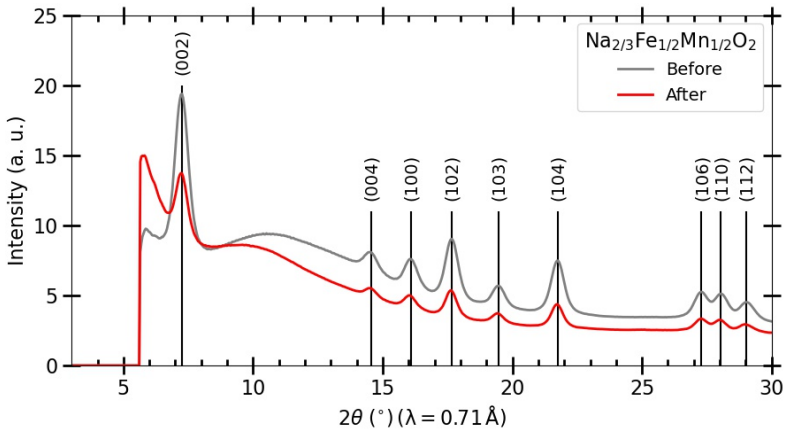

(a)

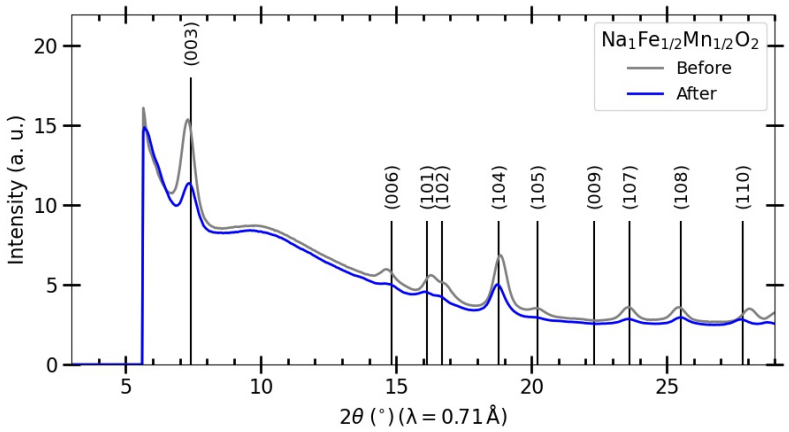

(b)

Figure 4.6: **Room temperature PXRD before and after neutron scattering**. (a) From P2-$Na_{0.67}Fe_{1/2}Mn_{1/2}O_2$. (b) From O3-$Na_1Fe_{1/2}Mn_{1/2}O_2$. Differences in intensity may be explained by variation in the amount of sample and measurement duration.

4.2.2 Single crystal XRD

Crystal samples of $Na_{0.67}Fe_{1/2}Mn_{1/2}O_2$ were synthesised at Royal Holloway by Dr. Sivaperumal Uthayakumar using the optical floating zone technique. Initially, a mixture of precursor chemicals is finely ground into a homogeneous powder that then undergoes one or more calcination processes - heating the precursor mixture in a controlled atmosphere. This process enables the break down of precursor compounds and the formation of new bonds. The resulting mixture is then compacted into a thin cylinder which undergoes sintering at high temperatures to enlarge the grain size [132].

The cylindrical crystal is split in two to form the *feed* and *seed* within the optical floating zone furnace. The furnace employs elliptical mirrors that focus the heat from four halogen lamps onto a specific region. The *feed* and *seed* crystals are mounted in vertical alignment such that the ends meet at the focal point. The interface between the rods is heated to form a molten zone. A crystal boule is produced by slowly moving the *feed* through the focal point while the two rods are counter-rotated to improve homogeneity [132, 133].

Single crystal X-ray diffraction was performed with the assistance of Dr. Daniel Nye and Dr. Gavin Stenning on the Agilent Gemini S diffractometer in the Materials Characterisation Laboratory at the ISIS Neutron and Muon Source. This is a lab based diffractometer with two independent X-ray sources (Mo and Cu), and is equipped with a 4-circle kappa goniometer and a HyPix-6000HE area detector. The Cryostream 800 Plus system allow temperature control over $\sim 100 - 500\,\mathrm{K}$ using highly laminar nitrogen gas flow to avoid ice formation on the sample [104].

Crystal boules of $Na_{0.67}Fe_{1/2}Mn_{1/2}O_2$ were found to contain many small crystal-

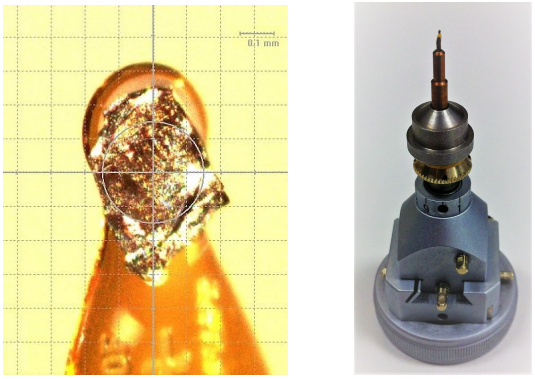

(a) (b)

Figure 4.7: **Sample preparation for single crystal X-ray diffraction**. (a) Close-up of a platelet wedge of $Na_{0.67}Fe_{1/2}Mn_{1/2}O_2$ crystal mounted on a microloop with 300 μm sample aperture using Fomblin. (b) Sample and microloop mounted on an adjustable magnetic base, ready to be installed into the sample position of the diffractometer.

lites with different orientations. Small samples were cleaved from the boule in an attempt to isolate a single grain. Preliminary measurements sampling a large region of reciprocal space were performed to check the samples, and identify a single grain. Each sample was mounted on a MiTeGen microloop using vacuum grease (Fomblin) to be mounted in the sample position of the diffractometer, see Fig. 4.7. The spot size of the beam was smaller than the samples being screened, and it was possible to scan over the samples. The sample shown in Fig. 4.7a was found to consist of a large single crystal with a small portion of a second crystallite on one side. The extended measurement was performed by focusing the beam on a region of the large single crystal well separated from the second crystallite.

All measurements were performed using Mo Kα radiation and analysed with the CrysAlis^{Pro} program [134]. A high redundancy experiment strategy was calculated by the program, and the sample was measured for 16 h 50 m at room tempera-

ture. A constant nitrogen flow around the sample provided an inert atmosphere to prevent changes in the composition during the measurement. This also ensured a constant temperature was maintained throughout. The data were processed by the CrysAlis^{Pro} program and exported for analysis and simulation using custom python scripts.

4.2.3 Unpolarised INS

Polycrystalline P2-$Na_{0.67}Fe_{1/2}Mn_{1/2}O_2$ and O3-$Na_1Fe_{1/2}Mn_{1/2}O_2$ were loaded into cylindrical niobium sample cans, and mounted in a furnace on the LET spectrometer [9]. Both samples were initially heated up to $T \sim 450\,\mathrm{K}$ to remove potential contamination from atmospheric hydrogen while loading the samples. Measurements were performed over the temperature range $T \sim 323 - 1000\,\mathrm{K}$. The "intermediate" aperture of the resolution chopper, at a resolution frequency of 240 Hz and pulse removal frequency of 80 Hz, provided a good balance between neutron flux and resolution. Chopper 1 was operated at 120 Hz to suppress the tails of the neutron energy distribution. Repetition rate multiplication was employed and this gave incident neutron energies $E_\mathrm{i} \sim 12.13, 3.70, 1.77$ and $1.03\,\mathrm{meV}$. A proton charge of $80\,\mu$Ahr ($1\,\mathrm{hr} = 40\,\mu$Ahr) was detected at the target during measurements above $T \sim 550\,\mathrm{K}$. Measurements at $T \sim 550$ and $323\,\mathrm{K}$ recorded a proton charge of 240 and $120\,\mu$Ahr, respectively. The data were reduced and analysed using a combination of the Mantid package [117] and custom python scripts.

An empty niobium can and a standard vanadium sample were also measured using the same instrument configuration. A proton charge of $40\,\mu$Ahr was detected at the target for both measurements. The empty can measurement gave the back-

ground signal that was subtracted from the sample data. The vanadium data set was used to determine the instrument energy resolution, given by the FWHM of a Gaussian distribution. At the elastic line, the energy resolution of $E_i \sim 12.13, 3.70$ and 1.77 meV were found to be $\delta E = 25.4(2), 67.5(4)$ and $332(3)\,\mu$eV, respectively.

4.2.4 *xyz*-polarised QENS

Polarised neutron scattering experiments were performed using the ThALES spectrometer [116] with *xyz*-polarisation analysis. Before each experiment, a cylindrical aluminium sample can (with an inner diameter of ~ 16 mm) was loaded with ~ 7 g of powdered sample to cover the $3 \times 2\,\mathrm{cm}^2$ cross section of the incident beam. The can was sealed using tungsten screws, and masked with gadolinium foil to prevent scattering contributions from aluminium and tungsten, see Fig. 4.8.

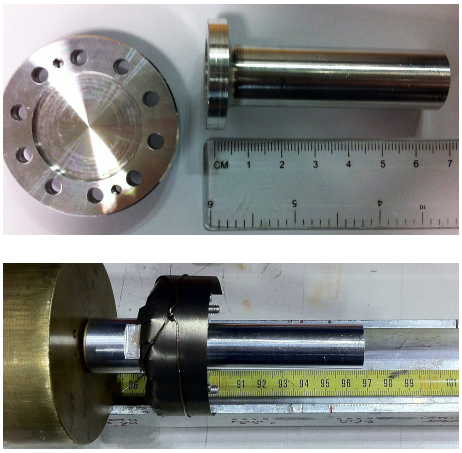

Figure 4.8: **Cylindrical aluminium sample can used on ThALES**. Bulk of the aluminium mass is contained in the head of the sample can, where it is sealed using tungsten screws. Scattering contributions from the head are prevented using gadolinium foil to mask it from neutrons.

ThALES was set up with large focusing Heusler monochromator and analyser

combination. Control of incident neutron spin was achieved using a Helmholtz coil set around the sample environment, and a Mezei flipper was used to switch between non-spin-flip (nsf) and spin-flip (sf) scattering. A beryllium filter was employed to minimise spurious scattering from the sample environment. However, this restricted the maximum attainable k_f to $1.55\,\text{Å}^{-1}$. Measurements were performed at several temperatures using a standard orange cryofurnace with an operating temperature range of $T = 1.8 - 573\,\text{K}$.

All measurements during the $Na_{0.67}Fe_{1/2}Mn_{1/2}O_2$ experiment were performed with k_f fixed at $1.5\,\text{Å}^{-1}$. The instrument energy resolution, δE was determined by fitting a Gaussian distribution to the scattering from a standard vanadium sample at room temperature, giving $\delta E = 194(3)\,\mu\text{eV}$. The temperature dependence of QENS from $Na_{0.67}Fe_{1/2}Mn_{1/2}O_2$ was studied over $T \sim 225 - 530\,\text{K}$ at constant $Q \sim 2.35\,\text{Å}^{-1}$. Similarly, the Q-dependent measurements were performed over $Q \sim 0.75 - 2.35\,\text{Å}^{-1}$ at $T \sim 530\,\text{K}$.

$Na_1Fe_{1/2}Mn_{1/2}O_2$ was measured over $T \sim 100 - 540\,\text{K}$ at constant $Q \sim 1.25\,\text{Å}^{-1}$ using $k_f = 1.3\,\text{Å}^{-1}$, and $Q \sim 2.20\,\text{Å}^{-1}$ using $k_f = 1.5\,\text{Å}^{-1}$. A Gaussian distribution was fitted to the $T \sim 100\,\text{K}$ data sets to determine the corresponding energy resolutions. Measurements using $k_f = 1.3\,\text{Å}^{-1}$ benefited from a narrow energy resolution of $\delta E = 85(1)\,\mu\text{eV}$, but at the expense of a limited Q range. Those using $k_f = 1.5\,\text{Å}^{-1}$ had access to an extended Q range with a broader energy resolution of $\delta E = 183(3)\,\mu\text{eV}$. This arrangement is suited for the study of ionic diffusion since models of translational diffusion predict narrow QENS widths at low Q which become broadened at higher Q. Measurements at $T \sim 540\,\text{K}$ were performed over $Q \sim 0.5 - 1.25\,\text{Å}^{-1}$ using $k_f = 1.3\,\text{Å}^{-1}$, and over $Q \sim 0.75 - 2.35\,\text{Å}^{-1}$ using $k_f = 1.5\,\text{Å}^{-1}$.

The polarisation axes were set up with x parallel to the scattering vector Q and z perpendicular to the scattering plane defined by k_i and k_f. The flipping ratio was determined by measuring the scattering from a quartz sample in the non-spin-flip (nsf) and spin-flips (sf) channels with incident neutron spins polarised along the x, y and z directions. The flipping ratios achieved during the $Na_{0.67}Fe_{1/2}Mn_{1/2}O_2$ experiment were $F_x = 11.3(1), F_y = 10.4(1)$ and $F_z = 12.7(1)$. For measurements on $Na_1Fe_{1/2}Mn_{1/2}O_2$, the flipping ratios were $F_x = 27.4, F_y = 26.0$ and $F_z = 28.1$ at $k_f = 1.5\,\text{Å}^{-1}$, and $F_x = 24(1), F_y = 24(1)$ and $F_z = 28(1)$ at $k_f 1.3\,\text{Å}^{-1}$.

The M, I and N components of scattering were once again determined using the expressions in Eq. (3.3), with associated statistical errors given by Eq. (3.4). These experiments aimed to enable the study of ionic diffusion via QENS in the nuclear spin incoherent (I) scattering cross section. Hence, the measurement durations of the six cross sections were chosen to minimise the uncertainty in the nuclear spin incoherent component of scattering. For both experiments, all nsf channels were measured for $\sim 35\,\text{s}$ each, and the sf channels for 5 times as long.

4.3 Results

4.3.1 Superstructure

Willis *et al.* [21] and Pandiyan [135] previously characterised the different Na-vacancy ordering patterns and determined the diffusion pathways in the structurally related Na_xCoO_2. However, the influence of the disorder within the transition-metal plane on Na-vacancy ordering and diffusion pathways currently remains an open question.

Here, the ordering of Na-vacancies has been investigated using single crystal x-ray diffraction from P2-$Na_{0.67}Fe_{1/2}Mn_{1/2}O_2$ to determine how superlattice formation is affected by the introduction of disorder within the transition-metal plane.

Room temperature x-ray diffraction is presented in Figs. 4.9 and 4.10, showing cuts in the (hk) plane at integer l and the l-dependence of the scattering, respectively. The Bragg reflections are indexed by the hexagonal unit cell with lattice parameters $a = 2.9335(3)$ and $c = 11.224(1)$ Å [1]. The in-plane scattering exhibits 6-fold rings of superstructure reflections around each Bragg reflection, similar to those observed from the ab planes of $Na_{0.67}CoO_2$ at 300 K [135]. These lie on a hexagonal grid $1/6^{\text{th}}$ the size of each in-plane reciprocal lattice parameter. Hence, the superstructure can be described by a supercell 6×6 times the underlying hexagonal unit cell. In fact, it is possible to use a smaller supercell to describe the observed scattering, see below. The absence of diffuse scattering implies the absence of short range correlations. This suggests the presence of a relatively well-ordered superstructure in the Na layers, and it is also consistent with random occupation of sites in the transition-metal layers by Fe and Mn. However, x-rays have limited sensitivity to ordering of Fe and Mn since they are next to each other in the periodic table.

Using density functional theory (DFT) calculations, Meng *et al.* identified two distinct Na-vacancy ordering patterns for $Na_{0.67}CoO_2$, both of which are consistent with a supercell 6×6 times the underlying hexagonal lattice [136]. The stripe structure shown in Fig. 4.11a naturally leads to a two layer periodicity that maximises separation between Na1 ions in subsequent layers, see Fig. 4.12a. The corresponding supercell vectors of the stripe structure are $\vec{a}' = 4\vec{a} + 2\vec{b}$, $\vec{b}' = \vec{a} + 2\vec{b}$ and $\vec{c}' = \vec{c}$. The honeycomb structure shown in Fig. 4.11b corresponds to a supercell twice as large in the ab plane, comprised of 6 Na layers, see Fig. 4.12b. The supercell vectors of

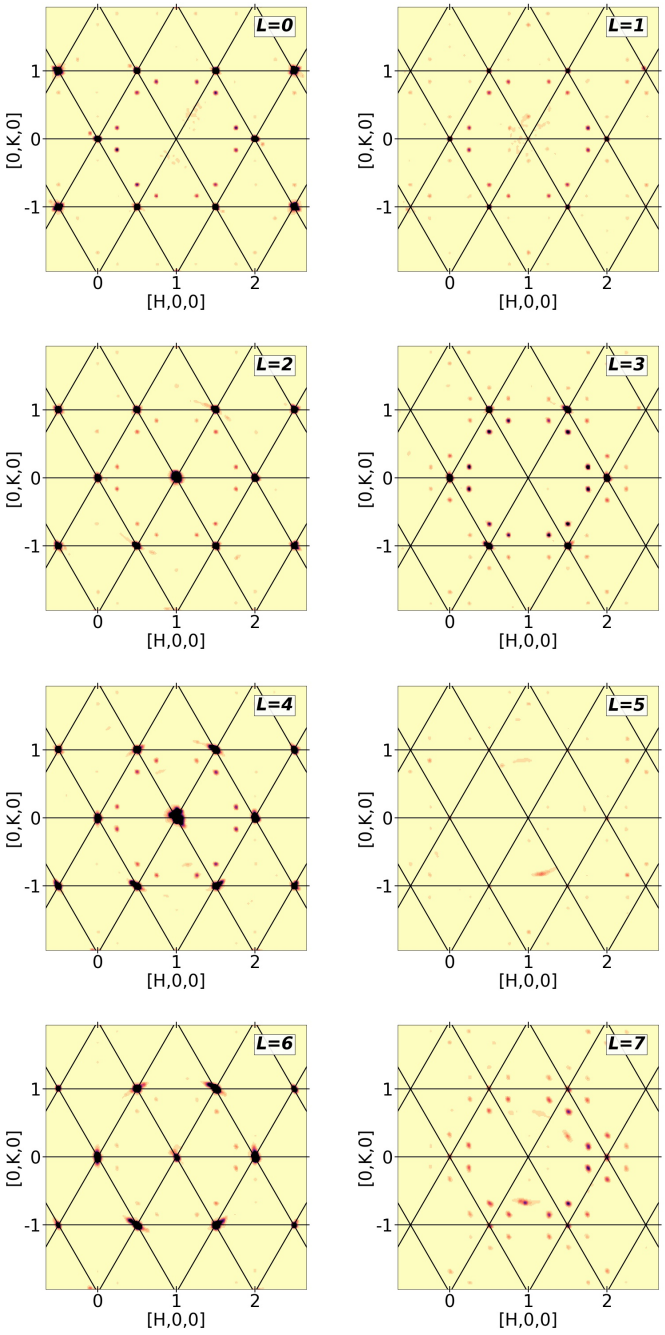

Figure 4.9: **X-ray diffraction from the (hk) plane of $Na_{0.67}Fe_{1/2}Mn_{1/2}O_2$ for $l = 0 - 7$.** Clear superlattice reflections are observed around principal Bragg reflections.

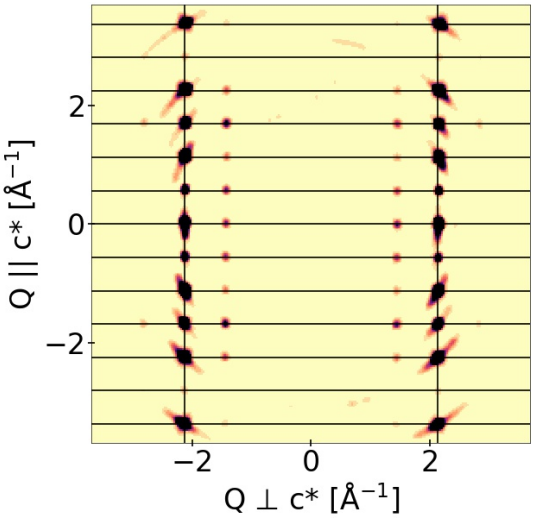

Figure 4.10: **X-ray diffraction along the l-direction of $\mathbf{Na_{0.67}Fe_{1/2}Mn_{1/2}O_2}$.** Displacement of superlattice reflections from Bragg reflections suggests a superlattice with a $1/6^{\text{th}}$ cell.

the honeycomb structure are $\vec{a}' = 4\vec{a} + 2\vec{b}$, $\vec{b}' = 2\vec{a} + 4\vec{b}$ and $\vec{c}' = 3\vec{c}$ [137].

Simulations of the x-ray diffraction patterns were performed using the simulation package `Dans-Diffraction` developed by Dr. Dan Porter [138]. Figures 4.11c and 4.11d show that both models correctly predict the in-plane scattering from the $(h, k, 3)$ plane of $Na_{0.67}Fe_{1/2}Mn_{1/2}O_2$. Along the l-direction, the two layer stripe model predicts the observed periodicity, see Fig. 4.12c. In contrast, both Alloul *et al.* [137] and Pandiyan [135] have shown that in $Na_{0.67}CoO_2$ the out-of-plane stacking sequence is in excellent agreement with the six layer periodicity of the honeycomb supercell. Hence, the disorder in the transition-metal planes changes the periodicity along the l-direction, and this leads to a different superstructure to $Na_{0.67}CoO_2$. By analogy with $Na_{0.8}CoO_2$, the formation of a striped superstructure is likely to favour quasi-1D diffusion [21]. Furthermore, the occupation of both Na1 and Na2 sites suggests that the hopping between Na1 and Na2 sites may occur, as for Na_xCoO_2.

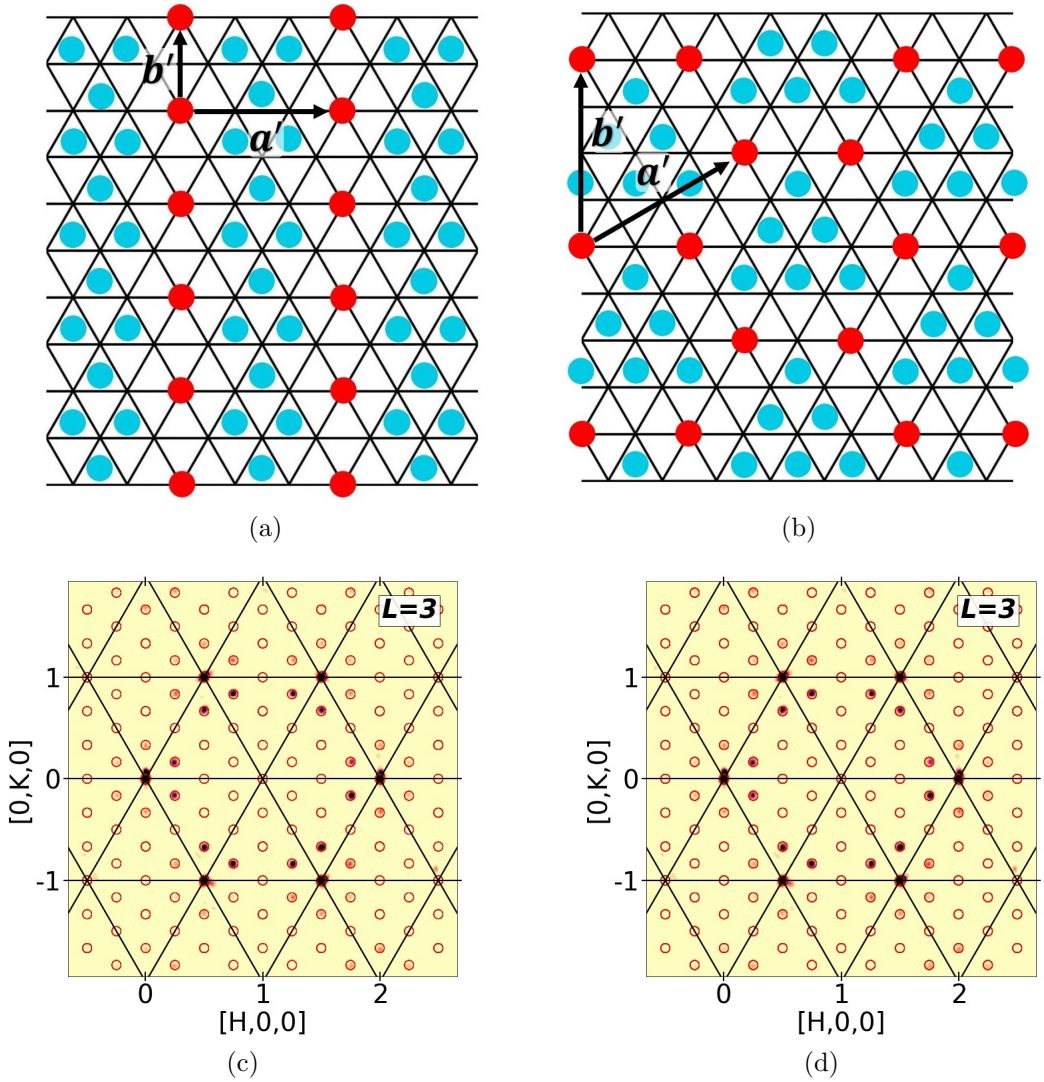

Figure 4.11: **Simulation of the structure in the** $(h, k, 3)$ **plane.** (a) Stripe model with a column of Na1 ions (red sites) in between three columns of Na2 ions (blue sites), and unit vectors $\vec{a}' = 4\vec{a} + 2\vec{b}$ and $\vec{b}' = \vec{a} + 2\vec{b}$. (b) Honeycomb model with unit vectors $\vec{a}' = 4\vec{a} + 2\vec{b}$ and $\vec{b}' = 2\vec{a} + 4\vec{b}$. (c) In-plane x-ray scattering simulated by the stripe model. (d) In-plane scattering simulated by the honeycomb model. Both models provide identical descriptions of the in-plane scattering.

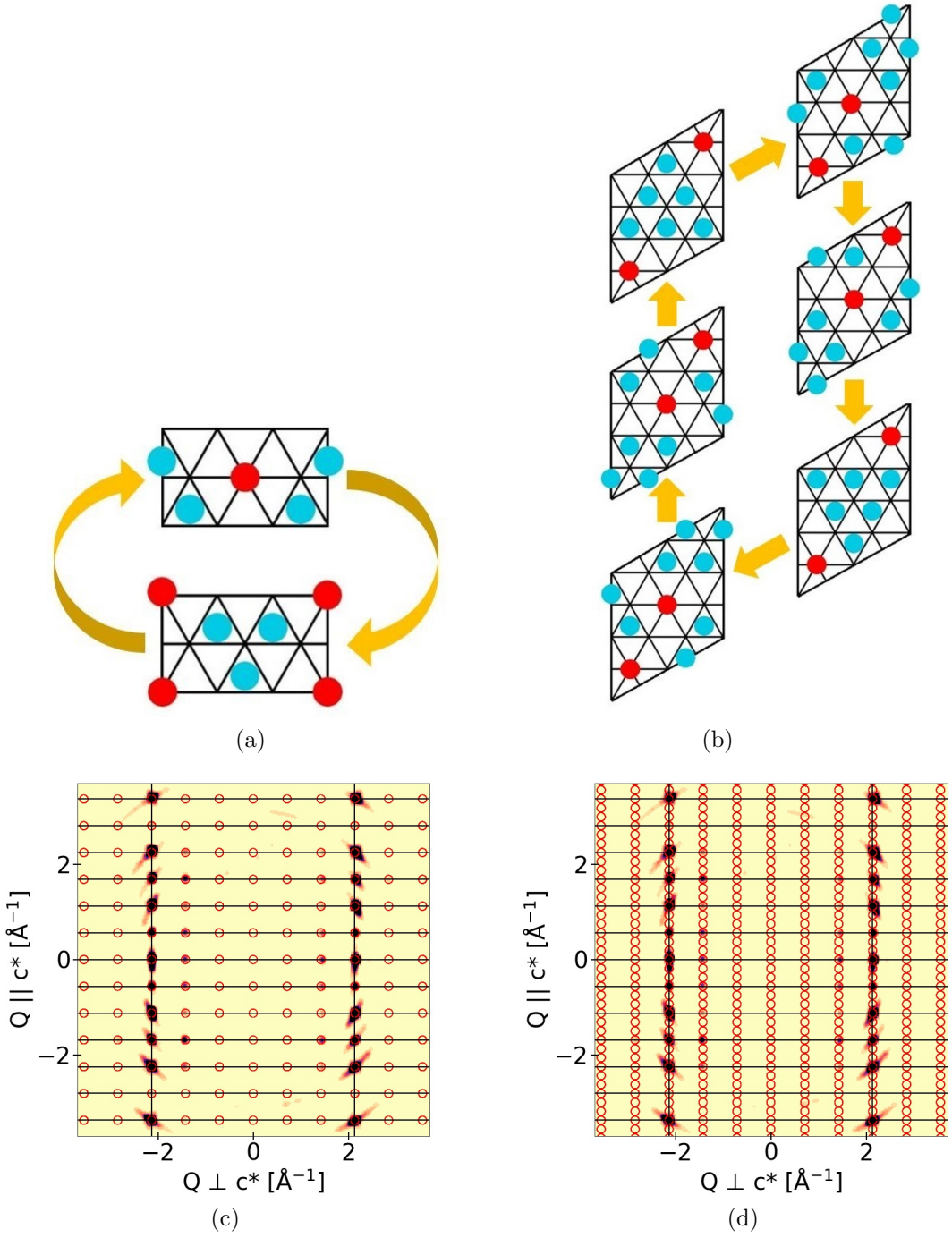

Figure 4.12: **Simulation of the scattering along the l-direction.** (a) The unit cell of the stripe model is made up of two Na layers. (b) The unit cell of the honeycomb model consists of six Na layers. (c) Out-of-plane scattering simulated by the stripe model. (d) Out-of-plane scattering simulated by the honeycomb model. The stripe model correctly predicts the positions of superlattice reflections observed in the data.

4.3.2 QENS from P2-$Na_{0.67}Fe_{1/2}Mn_{1/2}O_2$

The temperature evolution of unpolarised INS measured on the LET spectrometer using $E_i = 3.7\,\text{meV}$ is shown in Fig. 4.13. The broad diffuse scattering present at $Q < 1\,\text{Å}^{-1}$ and $T = 323\,\text{K}$ quickly decays at higher Q, see Fig. 4.13a. A low intensity band of scattering is also observable at 0.5 meV, spanning the entire Q range with negligible variation in intensity. Very broad diffuse scattering develops at high Q upon heating the sample up to $T = 550\,\text{K}$, with two significantly broad signals at $Q \sim 2.0$ and $2.4\,\text{Å}^{-1}$, see Fig. 4.13b. This diffuse signal is further enhanced at $T = 1000\,\text{K}$, at which temperature broad diffuse scattering is observed throughout the Q range shown in Fig. 4.13c.

The data set acquired using $E_i = 1.77\,\text{meV}$ provides better energy resolution to further investigate this diffuse scattering. Figure 4.14 shows the intensity as a function of energy transfer for $Q = 0.75$ and $1.55\,\text{Å}^{-1}$ at $T = 323$ and 550 K. The energy resolution function of the instrument was determined by fitting a Gaussian distribution to the scattering from a standard vanadium sample, and is represented by a grey curve in each sub-figure of Fig. 4.14. At low temperature and low Q, QENS in Fig. 4.14a shows a distinct energy broadening that is suppressed at higher Q in Fig. 4.14b, where the data is much closer to the resolution function. Upon heating up to $T = 550\,\text{K}$, the diffuse signal at low Q grows in intensity, as shown in Fig. 4.14c. Interestingly, at this temperature the data at the higher Q of $1.55\,\text{Å}^{-1}$, shown in Fig. 4.14d, exhibits a dramatic broadening in energy that cannot even be approximately described by the resolution function alone.

The behaviour observed at $T = 323\,\text{K}$ is consistent with scattering arising from the magnetic cross section, which is expected to have a greater intensity at low Q

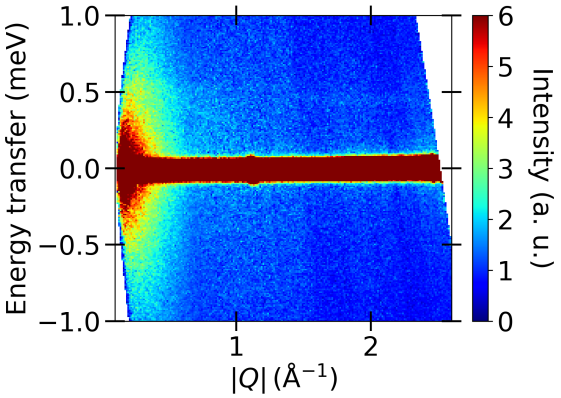

(a)

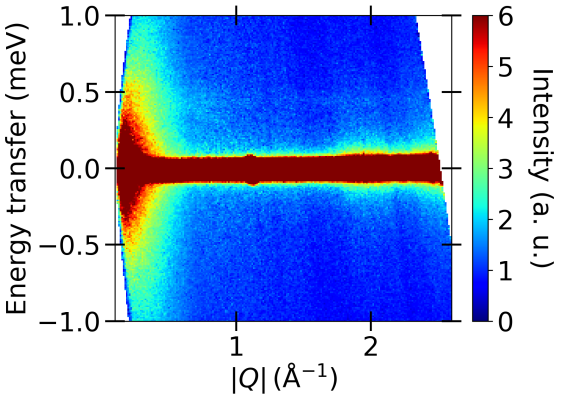

(b)

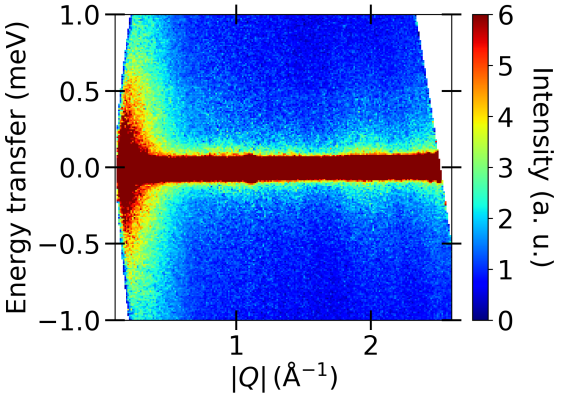

(c)

Figure 4.13: **Temperature evolution of unpolarised INS from $Na_{0.67}Fe_{1/2}Mn_{1/2}O_2$.** (a) At $T = 323\,\mathrm{K}$ the scattering exhibits a very diffuse contribution for $Q < 1\,\mathrm{Å}^{-1}$. (b) At $T = 550\,\mathrm{K}$, another very broad diffuse signal develops in the high Q region, most prominent at $Q = 2\,\mathrm{Å}^{-1}$. (c) All diffusely scattering contributions persist at $T = 1000\,\mathrm{K}$, where the signal at higher Q further broadens.

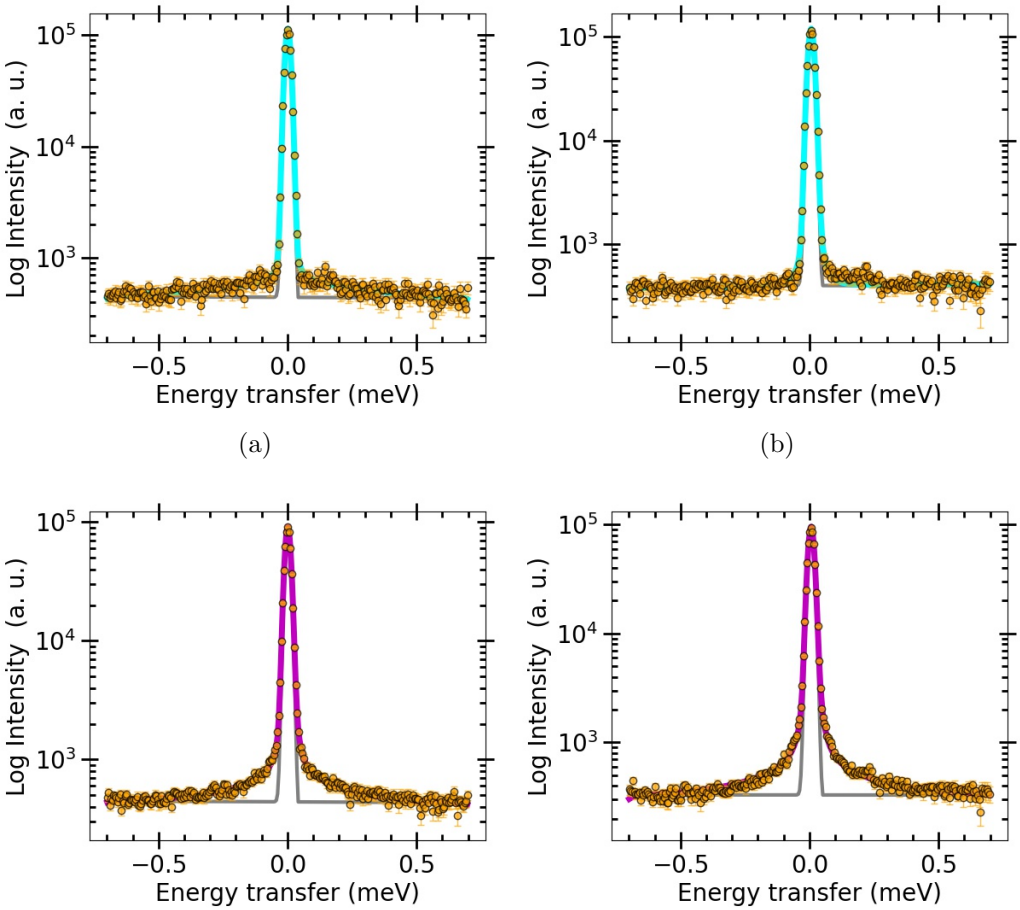

Figure 4.14: **Unpolarised QENS from $Na_{0.67}Fe_{1/2}Mn_{1/2}O_2$ measured with $E_i = 1.77\,\mathrm{meV}$ on LET.** (a) At $T = 323\,\mathrm{K}$ and $Q = 0.75\,\mathrm{Å}^{-1}$ the scattering exhibits energy broadening beyond the instrument resolution (represented by the grey curve), which is best described by an additional Lorentzian term in the fit model (cyan curve). (b) At $T = 323\,\mathrm{K}$ and $Q = 1.55\,\mathrm{Å}^{-1}$ the data is close to being resolution limited. (c) At $T = 550\,\mathrm{K}$ and $Q = 0.75\,\mathrm{Å}^{-1}$ there is increased intensity of the diffuse scattering observed at the lower temperature. The data are best described using two additional Lorentzian terms in the fit model (magenta curve). (d) A very broad QENS signal develops at $Q = 1.55 Å^{-1}$ upon heating up to $T = 550\,\mathrm{K}$. This signal has a narrower energy width than at $Q = 0.75\,\mathrm{Å}^{-1}$, but with a larger amplitude.

that decays with increasing Q due to the magnetic form factor. Magnetic diffuse scattering may arise from dynamic short-range ordering of spins just above T_N and paramagnetic scattering at higher temperatures. The data in Fig. 4.14 were all collected in the paramagnetic phase of $Na_{0.67}Fe_{1/2}Mn_{1/2}O_2$, which has a magnetic ordering temperature $T_N \sim 12.7\,\mathrm{K}$ [139].

At $T = 550\,\mathrm{K}$, the Q dependence of QENS energy width indicates scattering beyond magnetism. This is evidenced by the temperature dependence of QENS at $Q = 1.55\,\mathrm{\AA}^{-1}$, which becomes significantly broadened and intense upon further heating the sample. In fact, the temperature and Q dependence of the diffuse scattering shown in Fig. 4.14d is consistent with the onset of translational diffusion of ions. All models of translational diffusion predict small energy widths at low Q (tending to zero as Q tends to zero) and larger widths at higher Q (even though widths may tend to zero at Bragg points, powder averaging gives a significant width at high Q). The onset of ionic diffusion at higher temperature is consistent with ions gaining sufficient energy to overcome the activation barrier associated with translational diffusion.

Ionic diffusion is studied through the self-correlation function, which is determined from incoherent QENS. However, it is not possible to isolate scattering from each cross section using unpolarised neutron scattering. The contributions from nuclear and magnetic cross sections make it almost impossible to extract meaningful energy widths to study microscopic diffusion. Further progress can be made by employing a polarised neutron spectrometer to isolate the nuclear spin incoherent scattering, and better determine the magnitudes and energy widths of QENS arising from diffusing ions.

QENS data acquired on the ThALES spectrometer using *xyz*-polarisation analy-

sis are shown in Fig. 4.15 for $T = 530\,\mathrm{K}$. The total scattering in Fig. 4.15a exhibits the same behaviour previously observed in Figs. 4.14c and 4.14d. At $Q = 0.75\,\mathrm{\AA}^{-1}$, the energy broadening in the nuclear spin incoherent cross section is very close to that at $1.50\,\mathrm{\AA}^{-1}$, see Fig. 4.15b. Therefore, the highly diffuse QENS observed with unpolarised neutron scattering is dominated by signal that does not originate from ionic diffusion. This demonstrates the necessity of using polarised neutron scattering. Without polarisation analysis the contributions from other scattering cross sections in an unpolarised neutron experiment would dominate this minor variation in the nuclear spin incoherent cross section. Scattering from the magnetic cross section, shown in Fig. 4.15c, reveals that the energy width of the scattering from magnetic fluctuations is comparable to the widths observed using unpolarised neutrons.

The diffusion mechanism for Na^+ ions has been studied by fitting a Lorentzian distribution to the nuclear spin incoherent QENS data acquired at $Q = 0.75 - 2.35\,\mathrm{\AA}^{-1}$ at a constant temperature of $T = 530\,\mathrm{K}$. The Q-dependence of the extracted Lorentzian HWHM, Γ was modelled using the Chudley-Elliott model of jump diffusion

$$\Gamma = \frac{\hbar}{\tau}\left(1 - r\frac{\sin(Ql_{12})}{Ql_{12}} - (1-r)\frac{\sin(Ql_{22})}{Ql_{22}}\right), \tag{4.1}$$

where $l_{12} = 1.6937(2)$ and $l_{22} = 2.9335(3)\,\mathrm{\AA}$ are the fixed jump lengths for Na1-Na2 and Na2-Na2 hops respectively, r is the ratio between the two different hops, and τ is the mean residence time of ions [1, 91]. Initial fits were performed using models with only one hop length by fixing r at 0 for Na2-Na2 hops and at 1 for Na1-Na2 hops. Neither of these models describe the data over the full Q range, see the dashed curves in Fig. 4.16a. Subsequent fitting with r as a freely varying parameter provides the best description for $r = 0.4(1)$, which corresponds to 40%

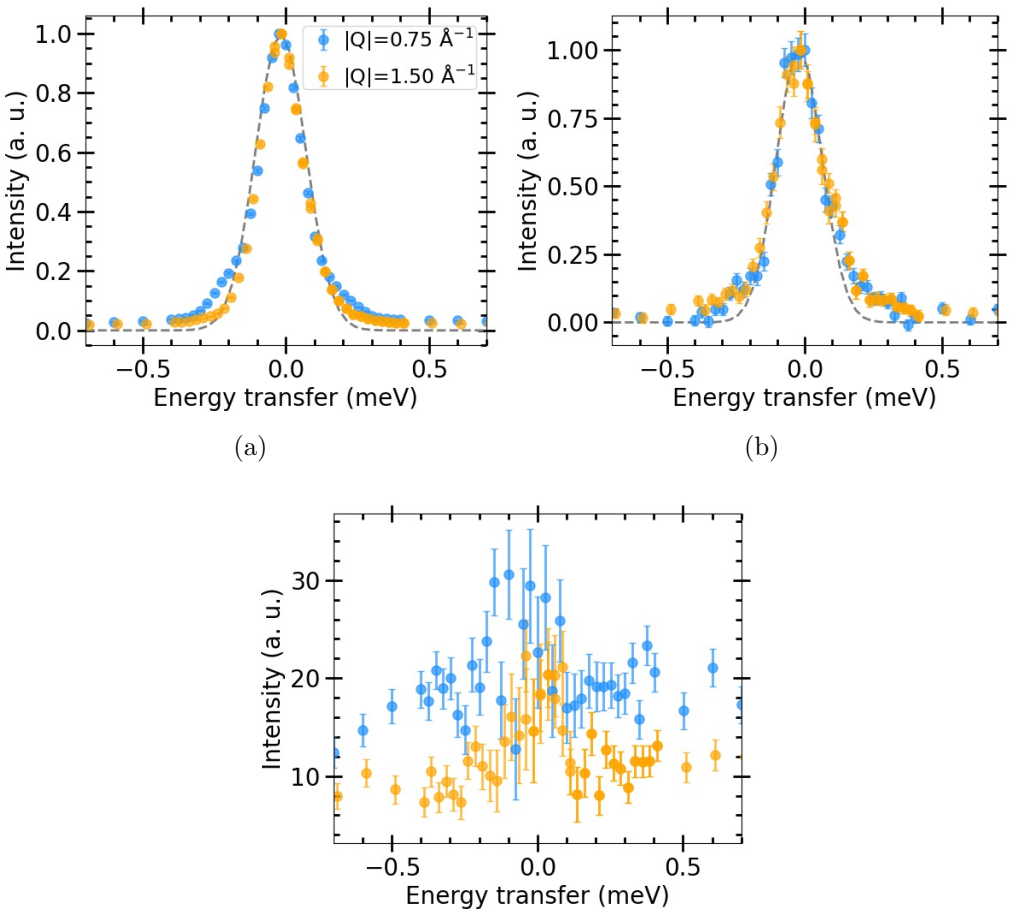

Figure 4.15: ***xyz*-polarised QENS from $Na_{0.67}Fe_{1/2}Mn_{1/2}O_2$ measured at $T = 530\,K$ on the ThALES spectrometer.** (a) Total scattering at $Q = 0.75$ has a larger energy width than at $Q = 1.50\,Å^{-1}$. (b) Nuclear spin incoherent scattering at $Q = 0.75$ and $1.50\,Å^{-1}$ exhibit similar energy widths, hence ionic diffusion is not the dominant source of QENS in the total scattering. Intensities for total and nuclear spin incoherent scattering have been normalised by respective peak intensities. (c) Magnetic scattering cross section exhibits very broad QENS that is much more intense at $Q = 0.75\,Å^{-1}$, as is predicted by the magnetic form factor.

Na1-Na2 hops, see the red curve in Fig. 4.16a. This gives a mean residence time of $\langle\tau\rangle = 17.9(9)\,\text{ps}$ for the two different hop lengths, and a mean diffusion coefficient $\langle D\rangle = (rl_{12}^2 + [1-r]l_{22}^2)/4\langle\tau\rangle = 9(3)\times10^{-6}\,\text{cm}^2\text{s}^{-1}$ [21].

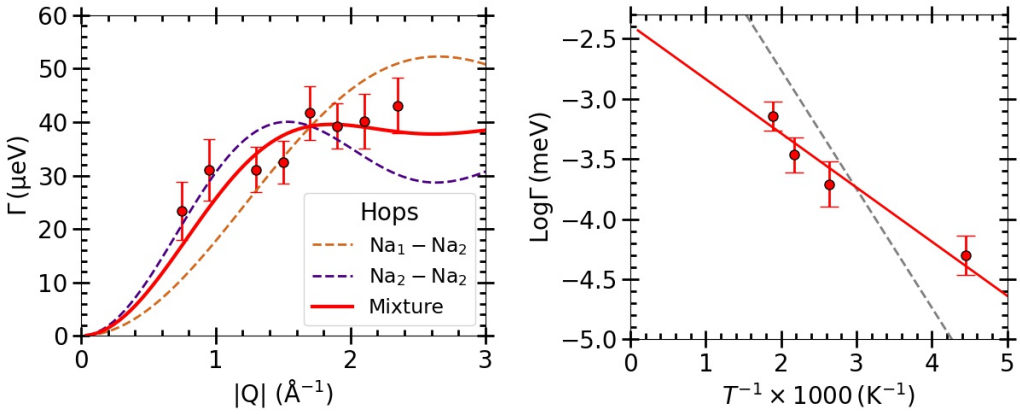

(a) (b)

Figure 4.16: **Jump diffusion models for $\mathbf{Na_{0.67}Fe_{1/2}Mn_{1/2}O_2}$.** (a) Fits of the Chudley-Elliott jump diffusion model to the quasi-elastic energy widths extracted from the nuclear spin incoherent cross section at different values of Q. The purple dashed curve is a fit using a model with only Na2-Na2 hops, and has a reduced chi-squared statistic $\chi^2_N = 2.15$. The brown dashed curve is a fit of a model with only Na1-Na2 hops and has $\chi^2_N = 2.75$. Best description is provided by the red curve with $\chi^2_N = 1.02$, which is a fit of a model with 40% Na1-Na2 hops. (b) A fit of the Arrhenius equation to quasi-elastic energy widths extracted at a range of temperatures at a constant $Q = 2.35\,\text{Å}^{-1}$. The red line is the best fit to data, corresponding to an activation energy $E_A = 39(4)\,\text{meV}$. The grey dashed line represents $Na_{0.8}CoO_2$ with $E_A = 85(5)\,\text{meV}$ [21].

The activation energy of the translational diffusion was also probed through measurements of nuclear spin incoherent QENS at $Q = 2.35\,\text{Å}^{-1}$ over $T = 225 - 530\,\text{K}$. A Lorentzian model was fitted to the data to determine Γ at each temperature, revealing a $\sim 218\,\%$ increase from $14(2)\,\mu\text{eV}$ at $T = 225\,\text{K}$ to $43(5)\,\mu\text{eV}$ at $T = 530\,\text{K}$. Figure 4.16b shows modelling of the temperature dependence of Γ using the Ar-

rhenius equation to obtain a value of $E_A = 39(4)\,\text{meV}$ for the activation energy, which corresponds to a temperature of $T_A = 450(50)\,\text{K}$. The grey dashed line represents the fit of the Arrhenius equation to the temperature dependent QENS from $Na_{0.8}CoO_2$, and corresponds to $E_A = 85(5)\,\text{meV}$ ($T_A = 990(60)\,\text{K}$) [21].

4.3.3 QENS from $Na_1Fe_{1/2}Mn_{1/2}O_2$

The temperature evolution of unpolarised INS performed on the LET spectrometer using $E_i = 3.7\,\text{meV}$ is shown in Fig. 4.17. At $T = 323\,\text{K}$, the low Q region at $\leq 0.5\,\text{Å}^{-1}$ displays a broad diffuse signal that quickly decays in intensity as Q increases, see Fig. 4.17a. Heating the sample up to $T = 550\,\text{K}$ results in increased intensity of the highly diffuse scattering at low Q, and another diffuse signal develops at higher Q with distinct features in the vicinity of $Q \sim 2.0\,\text{Å}^{-1}$, see Fig. 4.17b.

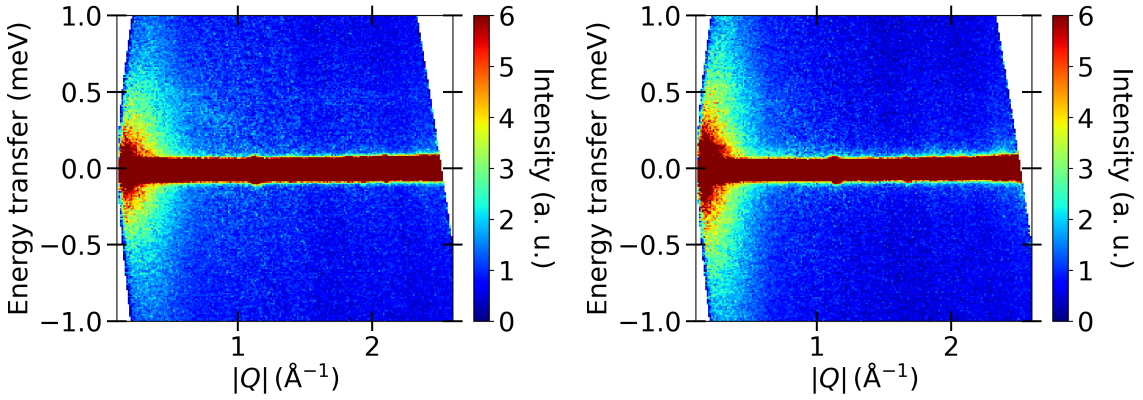

Figure 4.17: **Temperature evolution of unpolarised INS on LET.** (a) At $T = 323\,\text{K}$ the scattering exhibits a very diffuse contribution for $Q \leq 0.5\,\text{Å}^{-1}$, with another much narrower diffuse signal above $Q \sim 1.0\,\text{Å}^{-1}$. (b) At $T = 550\,\text{K}$ the diffuse scattering at low Q become more intense while the diffuse scattering at high Q broadens and develops distinct features around $Q \sim 2.0\,\text{Å}^{-1}$.

The extent of variation in the diffuse scattering at higher temperature suggests that the energy broadening and therefore the rate of diffusion in O3-type $Na_xFe_{1/2}Mn_{1/2}O_2$ is much slower than in the P2-type. Moreover, the variation in the Q dependence of diffuse scattering signals suggest that multiple scattering cross sections contribute to the diffuse scattering seen in Fig. 4.17. It is therefore very challenging to investigate the ionic diffusion in $Na_1Fe_{1/2}Mn_{1/2}O_2$ through unpolarised QENS using the LET data set.

The Q dependence of the QENS in the nuclear spin incoherent cross section was studied to determine the diffusion rate in $Na_1Fe_{1/2}Mn_{1/2}O_2$. Based on the results from LET, *xyz*-polarised neutron measurements were performed on ThALES using two values of k_f, to achieve a narrower energy resolution with $k_f = 1.3\,\text{Å}^{-1}$ for measurements at $Q = 0.50 - 1.25\,\text{Å}^{-1}$, while also having access to an extended Q range of $2.20 - 2.35\,\text{Å}^{-1}$ using $k_f = 1.5\,\text{Å}^{-1}$. The QENS measured over the entire Q range at constant $T = 540\,\text{K}$ was modelled once again by the convolution of the instrumental resolution function with a Lorentzian distribution. Subsequently, the Chudley-Elliott model of jump diffusion [91] was fitted to the Q dependence of Γ. Unlike in the P2-type structure, the Na^+ ions in the O3-type can only occupy the Na2 sites due to the different stacking sequence, with a hop length $l = 2.9590(6)\,\text{Å}$ between neighbouring sites [1]. The fit curve in Fig. 4.18a, generated using this fixed hop length, corresponds to a mean residence time $\langle\tau\rangle = 72(6)\,\text{ps}$, giving a mean diffusion coefficient $\langle D\rangle = l^2/4\langle\tau\rangle = 3.0(3) \times 10^{-6}\,\text{cm}^2\text{s}^{-1}$ [21].

The activation energy was determined by studying the behaviour of the nuclear spin incoherent QENS over $T = 100 - 540\,\text{K}$ at constant values of Q. Measurements with $k_f = 1.3\,\text{Å}^{-1}$ were performed at $Q = 1.25\,\text{Å}^{-1}$ and those with $k_f = 1.5\,\text{Å}^{-1}$ at $Q = 2.20\,\text{Å}^{-1}$. The instrumental energy resolution was determined by fitting a

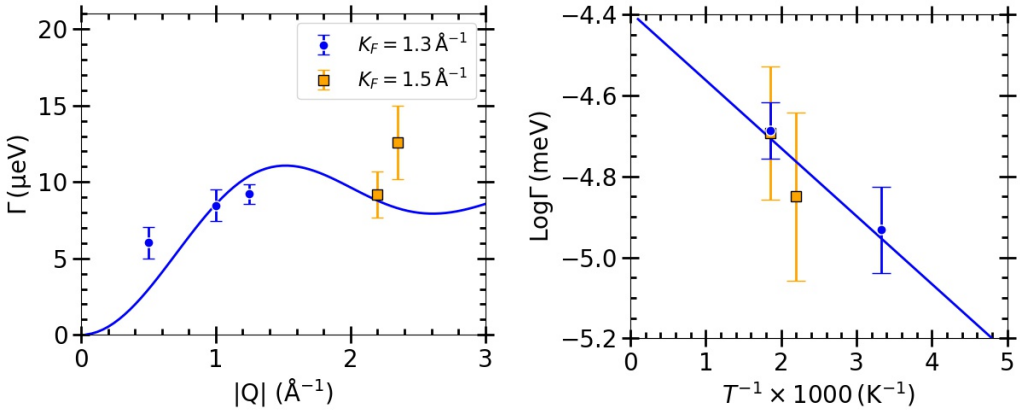

(a) (b)

Figure 4.18: **Jump diffusion model for $Na_1Fe_{1/2}Mn_{1/2}O_2$.** (a) Fit of the Chudley-Elliott model of jump diffusion with a single fixed hop length yields a residence time $\tau = 72(6)$ ps. (b) A fit of the Arrhenius equation to the temperature dependence of Γ yields $E_A = 14(2)$ meV. Values of Γ from different k_f were normalised to common high temperature point.

Gaussian profile to the scattering at $T = 100$ K for both values of Q. The scattering for $T > 100$ K exhibits QENS that broadens further with increasing temperature, consistent with the behaviour seen in Fig. 4.17, and could not be adequately described using only the resolution function. At $Q = 1.25\,Å^{-1}$ and $T = 300$ K the Lorentzian HWHM is $\Gamma = 7.2(8)\,\mu$eV and increases by $\sim 28\,\%$ to $9.2(6)\,\mu$eV at 540 K. Fitting the Arrhenius equation to the temperature dependence of Γ yields an activation energy $E_A = 14(2)$ meV ($T_A = 160(20)$ K), see Fig. 4.18b.

4.4 Discussion & Conclusions

4.4.1 Superstructure

For $x = 2/3$, the presence of the different, disordered transition-metal layer is sufficient to change the details of the superstructure compared to the corresponding composition for Na_xCoO_2. However, it does not entirely suppress the formation of a superstructure, perhaps because the energetics are dominated by the in-plane Coulomb interactions [128]. Furthermore, it is known that Na_xCoO_2 exhibits superstructure reflections at all compositions [135] even when the bulk diffusion coefficient is high [24]. Hence, it is unlikely that the presence of a superstructure will significantly suppress translational diffusion at most compositions.

4.4.2 Diffusion

The results for the diffusion in P2 and O3-type $Na_xFe_{1/2}Mn_{1/2}O_2$ are summarised in Fig. 4.19. P2-$Na_{0.67}Fe_{1/2}Mn_{1/2}O_2$ has a diffusion rate ~ 3 times greater than O3-$Na_1Fe_{1/2}Mn_{1/2}O_2$ at $T \sim 530\,\mathrm{K}$, but O3 has a lower activation energy. It should be noted that the activation energies are averaged over a range of local environments. Activation energies will depend upon the interactions between the Na and Fe & Mn in the transition-metal layer. Nevertheless, a similar trend is predicted for P2 and O3-type Na_xCoO_2, see Fig. 4.3 [22].

The diffusion mechanism for P2-$Na_{0.67}Fe_{1/2}Mn_{1/2}O_2$ differs from the mechanism proposed for P2-$Na_{0.8}CoO_2$, since both Na2$-$Na1 and Na2$-$Na2 hops are required to explain the Q-dependence of the energy widths in Fig. 4.16a. However, it must be noted that the $Na_{0.8}CoO_2$ data do not go to high enough Q to distinguish between

the two models.

P2-$Na_{0.67}Fe_{1/2}Mn_{1/2}O_2$ has a diffusion coefficient an order of magnitude larger than P2-$Na_{0.8}CoO_2$ at $T \sim 530\,\mathrm{K}$, see Fig. 4.4b, and its activation energy is a factor two lower, which is promising for battery performance. It should be noted that QENS gives hop frequencies, and does not distinguish between localised or translational diffusion. However, by analogy with Na_xCoO_2, away from ideal stoichiometry the degree of translational diffusion is presumably high. The diffusion rate of O3-$Na_1Fe_{1/2}Mn_{1/2}O_2$ is intermediate between the two rates for the P2 compositions.

It is interesting to note that the diffusion rates for P2-type layered sodium transition-metal oxides may be partly explained by the interlayer separation in these compounds. The separation of sodium and oxygen planes in P2-$Na_xFe_{1/2}Mn_{1/2}O_2$ is $\sim 1.76\,\text{Å}$ [140], approximately 3% greater than $\sim 1.71\,\text{Å}$ for P2-Na_xCoO_2 [141].

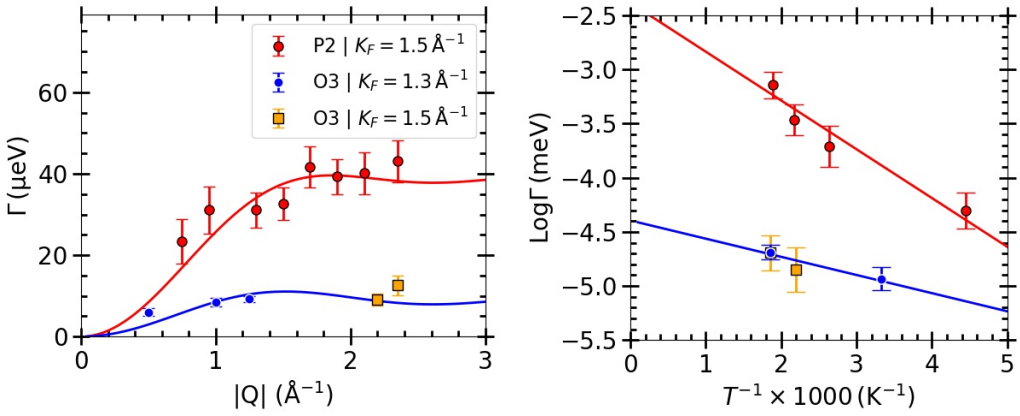

(a) (b)

Figure 4.19: **Comparing jump diffusion models for P2 and O3-type $Na_xFe_{1/2}Mn_{1/2}O_2$.** (a) Chudley-Elliott model of jump diffusion with a single hop length for $Na_1Fe_{1/2}Mn_{1/2}O_2$ (blue) compared to a model with the two hop lengths for $Na_{0.67}Fe_{1/2}Mn_{1/2}O_2$ (red). (b) Arrhenius plots with gradient corresponding to $E_A \sim 14(2)$ (blue) and $\sim 39(4)\,\mathrm{meV}$ (red).

These results demonstrate the need to measure nuclear spin incoherent scattering using polarization analysis in order to obtain completely reliable, quantitative data. It is interesting to speculate why the previous experiment on Na_xCoO_2 using unpolarised neutrons seems to have worked well. One possibility is the narrower energy resolution using the OSIRIS spectrometer may have made the wider components much less visible. Another factor is the smaller magnetic moment in Na_xCoO_2. Incoherent scattering will usually be narrower than these components and, therefore, it is a good strategy using unpolarised neutrons to use narrower energy resolution. However, the price paid for achieving this is a smaller Q range, and this makes it more difficult to determine the diffusion mechanism.

Chapter 5

z^+ Polarisation Analysis on LET Spectrometer

5.1 Background

The previously discussed technique of *xyz* polarisation analysis (PA) achieves unambiguous separation of the nuclear, magnetic, and nuclear spin incoherent components of the scattering from measurements of 6 polarisation-dependent cross sections. It is an evolution of uniaxial PA and has been well established on multi-detector instruments such as the D7 spectrometer at the ILL, and is particularly relevant for instruments at spallation neutron sources where detector banks covering a large solid-angle are often employed [84]. Novel magnetic ground states of the pyrochlore lattice have garnered much interest, and have been extensively studied using a range of neutron PA techniques [25, 26, 142]. Presented here is a brief review highlighting the capabilities of PA techniques used to study $Ho_2Ti_2O_7$.

The pyrochlore structure includes corner-sharing tetrahedra of magnetic ions.

For $Ho_2Ti_2O_7$, the crystal electric field makes the Ho ion Ising-like, such that moments can only point towards or away from the centre of the tetrahedron. The ground state of this system is macroscopically degenerate with two spins pointing in and two pointing out for each tetrahedron. This system maps onto ice with a tetrahedral arrangement of water molecules with two long and two short bond lengths. For this reason the magnetic ground state of $Ho_2Ti_2O_7$ is known as spin ice [143]. The ice rules (two spins in, two spins out) leads to characteristic features in the magnetic diffuse scattering - pinch-point singularities, which are bow-tie like diffuse signals centred on reciprocal lattice points. The low energy excitations from this ground state give emergent magnetic monopoles [144], and broadening of the pinch-point scattering has been related to the separation between magnetic monopoles.

The pinch-point singularities contribute very weakly to the total scattering and can be masked by the structural scattering near the Brillouin zone centre. Fennell *et al.* employed uniaxial (z) polarisation analysis to isolate the nsf and sf scattering components from a single-crystal sample of $Ho_2Ti_2O_7$ at $T = 1.7\,\text{Å}^{-1}$ [25]. The sf scattering along z measures the components of the magnetic moments perpendicular to z, and the correlations from these components are important in identifying the spin ice state. The nsf channel along z measures the components of the magnetic moments parallel to z, which are important in probing the correlations due to the long-range dipolar interactions [145].

The sf signal in Fig. 5.1(a) shows pure magnetic signal on top of a flat nuclear spin incoherent background, and exhibits pinch-point singularities at $(0, 0, 2)$, $(1, 1, 1)$ and $(2, 2, 2)$, as expected from a spin ice. The nsf channel in Fig. 5.1(b) exhibits strong structural scattering which dominates the unpolarised scattering signal shown in Fig. 5.1(c). These polarised scattering results combined with Monte Carlo simula-

tions in Fig. 5.1(d-f) have verified the nearest-neighbour spin ice model in $Ho_2Ti_2O_7$. The disagreement between the observed and predicted nsf scattering was resolved by a correction to the nearest-neighbour model identified through further polarised neutron scattering experiments [25].

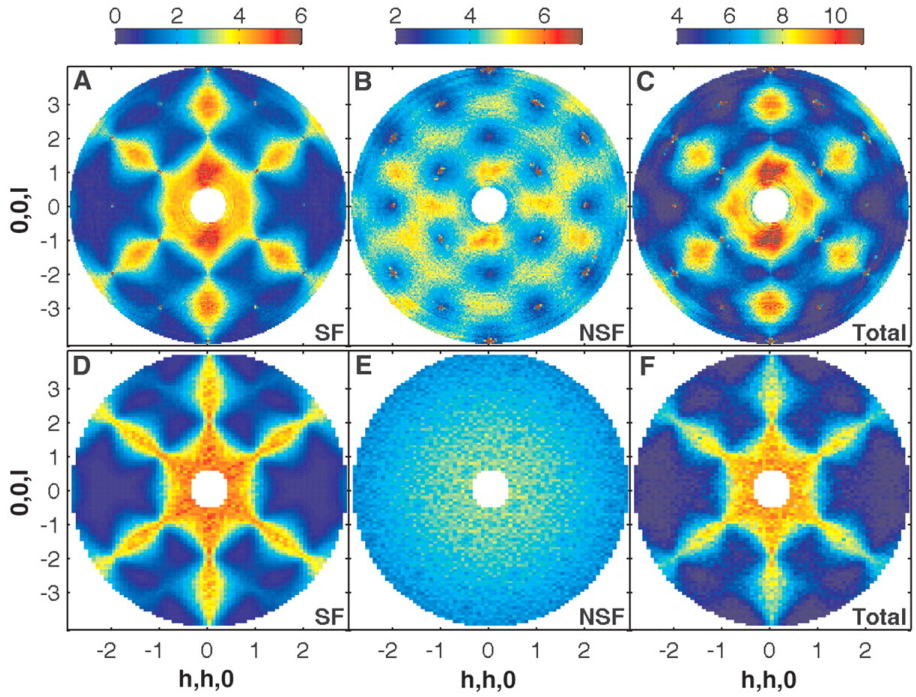

Figure 5.1: **Diffuse scattering of polarised neutrons from $Ho_2Ti_2O_7$ at** $T = 1.7\,\mathrm{K}$. (a) to (c) Experimental observations. (d) to (f) Monte Carlo simulations of the nearest-neighbour spin ice model. (a) The SF channel with pinch points at $(0, 0, 2n)$ and (n, n, n), where n is a positive integer. (b) Observed NSF channel. (c) The sum of (a) and (b), equivalent to unpolarised scattering. (d) Calculated SF channel. (e) Calculated NSF channel. (f) The sum of (d) and (e) [25].

Hallas *et al.* developed a method to extract detailed information on spin correlations from powder neutron scattering data using reverse Monte Carlo (RMC) techniques [26]. This method requires very accurate measurements of the magnetic signal, and they achieved that using *xyz* PA, where it is possible to eliminate the

nuclear spin incoherent and nuclear contributions to the scattering. The results of an experiment on polycrystalline $Ho_2Ti_2O_7$ measured using *xyz* PA are presented in Fig. 5.2. The spin correlations determined using RMC allow the single-crystal magnetic diffuse scattering to be calculated. Remarkably, the pinch points in the scattering are accurately reproduced, see Fig. 5.2(b).

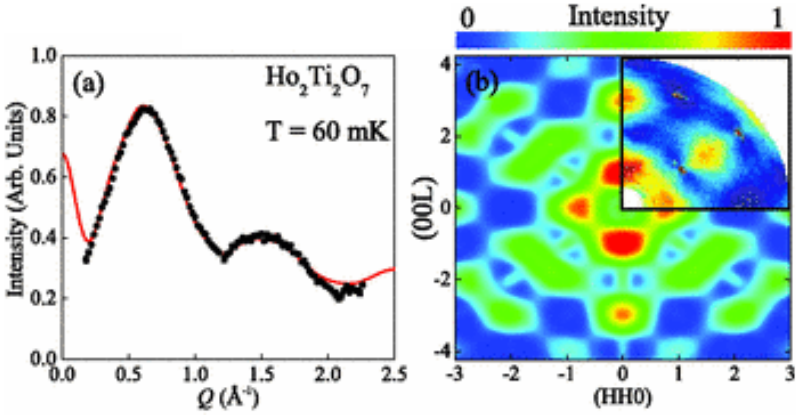

Figure 5.2: **RMC refinements of the magnetism in $Ho_2Ti_2O_7$.** (a) RMC refinement of the magnetic scattering at $T = 60\,\mathrm{mK}$ obtained with *xyz* PA. (b) Single-crystal magnetic scattering calculated from an ensemble of refined RMC configurations [26]. Inset shows experimental single-crystal scattering data from Ref. [25].

It is known that *xyz* polarisation analysis of scattering with out-of-plane components exhibit anomalous behaviour at low scattering angles. For a large area detector with significant coverage out of the horizontal scattering plane, such as on LET, this severely limits the utility of the *xyz* PA technique. The 10-point technique proposed by Ehlers *et al.* avoids this problem by including measurements with incident neutron polarisation along two additional direction [142], but the extended measurement times often render this approach infeasible. Additionally, both techniques employ Helmholtz coils to control the orientation of incident neutron spin. The geometry of the Helmholtz coils effectively masks regions of the detector, thereby restricting the

accessible range in reciprocal space.

The z$^+$ technique described in this chapter uses the out-of-plane variation in the scattering of neutrons polarised along the z-direction to enable the isolation of magnetic, nuclear spin incoherent and nuclear cross sections for polycrystalline samples. This greatly enhances the capabilities of instruments such as LET with significant out-of-plane detector coverage, including for inelastic neutron scattering.

5.2 Explanation of z$^+$

The scattering of neutrons from atoms can arise from the short-range nuclear and magnetic interactions between the two systems, with each interaction having a different effect on the spin of the neutrons. Interactions via the nuclear force cause *nuclear coherent* and *isotope incoherent* scattering. Nuclear coherent scattering arises from the average scattering lengths of the nuclei in a sample. In general, variations in the scattering lengths within a sample lead to incoherent scattering. Since the scattering length is different for each isotope, a random distribution of isotopes gives rise to isotope incoherent scattering. Polarisation analysis is unable to distinguish between nuclear coherent and isotope incoherent scattering because the neutron spin is unchanged during the scattering event, hence these interactions are known as *nuclear* (N) scattering [142].

The scattering length also varies depending on whether the neutron spin is parallel or anti-parallel to the nuclear spin, and the random configuration of nuclear spins within a sample lead to *nuclear spin incoherent* (I) scattering. This type of interaction has a 2/3 probability of flipping the neutron spin. Scattering can also arise from the interaction between the magnetic moment of the neutron and the local

magnetic field of an atom with unpaired electrons, giving rise to *magnetic* (M) scattering. The details of the magnetic structure within the sample determine whether the neutron spin is flipped during a magnetic scattering event [142].

The z$^+$ method is able to separate the three different scattering components by measuring the non-spin-flip (nsf) and spin-flip (sf) cross sections with the incident beam polarisation, $\vec{P}$ only along the z-direction. The partial differential neutron scattering cross section, which is the sum over all three contributions to the scattering, can be expressed in terms of the nsf and sf scattering cross sections as

$$\begin{aligned}\left(\frac{\partial^2\sigma}{\partial\Omega\partial E}\right)_{total} &= N + I + M \\ &= \left[\left(\frac{\partial^2\sigma}{\partial\Omega\partial E}\right)_{coh} + \left(\frac{\partial^2\sigma}{\partial\Omega\partial E}\right)_{incoh}^{isotope}\right] + \left(\frac{\partial^2\sigma}{\partial\Omega\partial E}\right)_{incoh}^{spin} + \left(\frac{\partial^2\sigma}{\partial\Omega\partial E}\right)_{mag} \\ &= \left(\frac{\partial^2\sigma}{\partial\Omega\partial E}\right)_{nsf}^{z} + \left(\frac{\partial^2\sigma}{\partial\Omega\partial E}\right)_{sf}^{z}.\end{aligned} \tag{5.1}$$

For a polycrystalline paramagnetic-like scatter, the nsf and sf cross sections include the following contributions from each of the scattering components N, I and M

$$\left(\frac{\partial^2\sigma}{\partial\Omega\partial E}\right)_{nsf} = N + \frac{1}{3}I + \frac{1}{2}M\left[1 - (\hat{P}\cdot\hat{Q})^2\right], \tag{5.2a}$$

$$\left(\frac{\partial^2\sigma}{\partial\Omega\partial E}\right)_{sf} = \frac{2}{3}I + \frac{1}{2}M\left[1 + (\hat{P}\cdot\hat{Q})^2\right], \tag{5.2b}$$

where $\hat{P}\cdot\hat{Q}$ is the projection of the incident polarisation $\vec{P}$ onto the momentum transfer wave-vector $\vec{Q}$ [146]. The geometry of a z$^+$ polarisation analysis experiment

on a spectrometer employing a cylindrical detector array is illustrated in Fig. 5.3. This set-up is characterised by the azimuthal angle ϕ around the Debye-Scherrer cone, the scattering angle 2θ between the incident neutron wave-vector k_i and scattered wave-vector k_f, $2\theta_p$ which is the projection of 2θ onto the horizontal scattering plane, and the angle γ between the horizontal plane and k_f. Then the variation of the magnetic scattering described by $(\hat{P} \cdot \hat{Q})^2$ can be parametrised to give the relation

$$(\hat{P} \cdot \hat{Q})^2 = \frac{E_f \cos^2(\frac{\pi}{2} - \phi)[1 + \cos^2 2\theta_p \cos^2 2\theta - 2\cos 2\theta_p \cos 2\theta \cos\gamma]}{E_i + E_f - 2\cos 2\theta\sqrt{E_i E_f}}, \qquad (5.3)$$

which was derived by Dr. Gøran Nilsen [147]. Hence, the intensity of magnetic diffuse scattering is predicted to vary as $\cos^2(\pi/2 - \phi)$ around the Debye-Scherrer cone. Then the magnitude of each scattering component is determined by substituting Eq. (5.3) into Eqs. (5.2a) and (5.2b) and fitting the empirically observed ϕ-dependence. For a non-magnetic system, the separation of N and I components is achieved simply by subtracting half of the intensity in sf channel from the intensity in the nsf channel.

5.3 Experimental Procedure

Realising z^+ polarisation analysis on the time-of-flight neutron spectrometer LET involves generating an incident spin-polarised neutron beam and analysing the polarisation of the scattered beam. Modifications necessary to achieve this are illustrated in Fig. 5.4. A spin-polarised neutron beam is obtained using a removable transmission-based two-channel "V-cavity" FeSi super-mirror polariser along the lin-

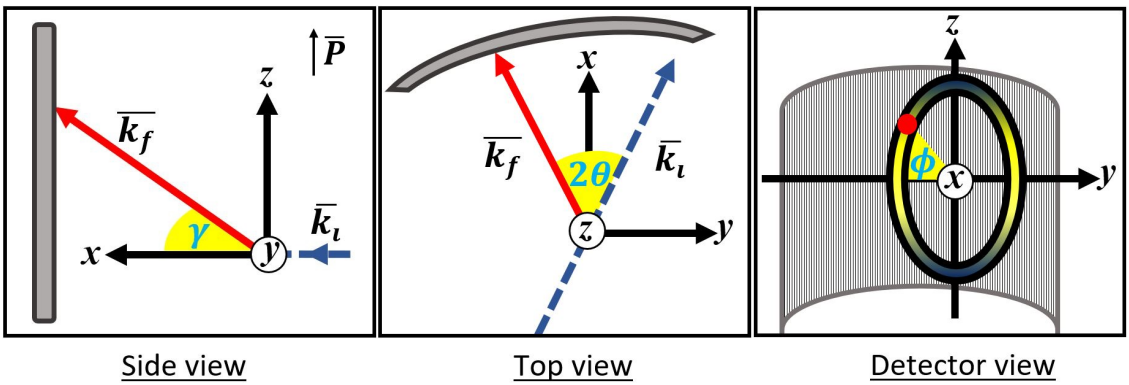

Figure 5.3: **Scheme of a z^+ PA experiment on a large area multi-detector instrument**. γ is the angle between the horizontal scattering plane and the scattered neutron wave-vector k_f. 2θ is the scattering angle between the incident and scattered neutron wave-vector with $2\theta_p$ as its projection onto the horizontal scattering plane. ϕ is the azimuthal angle around the Debye-Scherrer cone. The area multi-detector is shown in grey in each panel.

early converging section of the beam guide between the moderator and the sample position [148]. The combinations of super-mirror coatings inside the polariser ensure the transmission of the desired spin state while the undesired spin state is scattered out of the beam and absorbed by the side walls [27]. Details of the polariser are provided in Ref. [27] and Ref. [28]. Once polarised, the beam encounters a precession coil neutron spin flipper before being transported to the sample environment through guide fields.

The standard LET sample environment is modified as illustrated in Fig. 5.5 to enable analysis of the scattered neutron polarisation over the $\sim \pi$ st of continuous detector coverage. The z^+ technique is made possible using a hyper-polarised ^{3}He spin-filter, the so-called "banana cell", which covers 180 ° in the horizontal plane and $\gamma = \pm 30.2$ ° in the vertical direction [27]. The banana cell, mounted on the exterior of a orange cryostat, is housed within a gas tank installed in the LET main

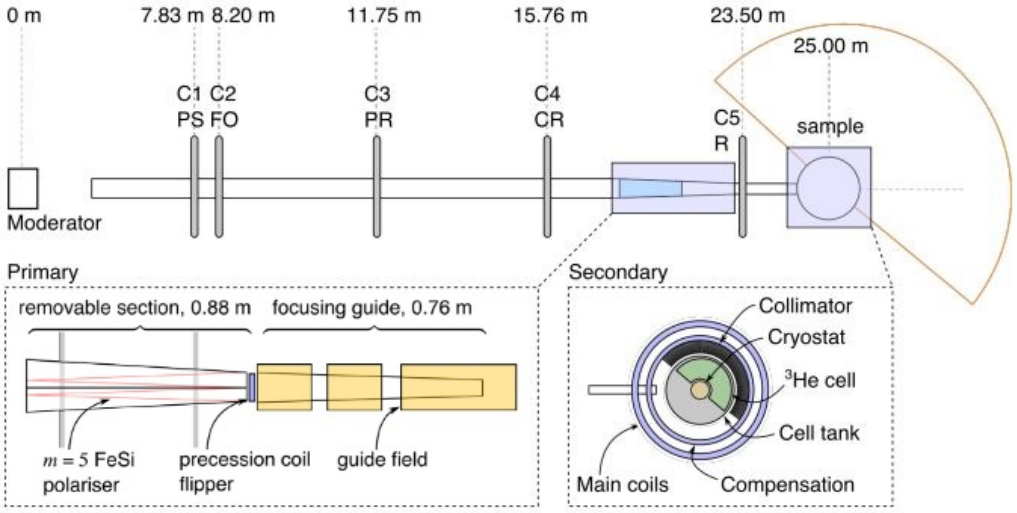

Figure 5.4: **Schematic of the LET spectrometer with $\mathbf{z}^+$ PA**. Positions of the polariser and flipper, and the analyser are shown in the magnified regions. The spin-polarised beam is created by the super-mirrors shown as red line, and passes through an adiabatic spin flipper and guide fields before reaching the sample environment where it is analysed by a wide-angle ^{3}He spin-filter analyser. Sourced from Ref. [27].

vacuum tank. Isolating the banana cell from the vacuum tank in this way allows for rapid and reproducible cell changeover during long experiments. Inside the vacuum tank, a radial oscillating collimator is employed to minimise the background from the modified sample environment and the spin-filter analyser. Above and below the collimator are the holding field coils, comprised of a main and compensation set, which provide a highly homogeneous magnetic environment to minimise depolarisation of the banana cell due to magnetic field gradients [27, 28]. Beyond the sample environment, a permanent transmitted beam monitor is installed behind a pinhole drilled into the beam-stop. During a z^+ PA experiment, this monitor measures the flipping ratio of the transmitted beam, thus allowing corrections for the time-dependent analysing power of the banana cell [28].

A powder sample of $Ho_2Ti_2O_7$ was measured in a thin walled annular aluminium can at $T = 2\,\mathrm{K}$ using an orange cryostat with an operating temperature range of $\sim 1.8 - 300\,\mathrm{K}$. The resolution and pulse remover choppers were operated at 240 and 120 Hz, respectively. Measurements were performed using $E_i = 4\,\mathrm{meV}$, achieving an energy resolution of 0.1 meV at the elastic line. The time-dependent polarisation of the banana cell necessitates short measurements of the nsf and sf channels to maintain an approximate equal polarisation during measurements of nsf and sf pairs. Hence, 29 measurements of each channel were performed with a proton charge of $10\,\mu$Ahr detected at the target during each measurement, which translates to approximately 15 mins per measurement. Measurements of this duration also avoid overheating of the spin flipper. Section 5.4 details preprocessing and analysis of the collected data.

The polarisation corrections performed on the data depend on the polarising efficiency of the polariser, which is quantified using the scattering from a diffuse

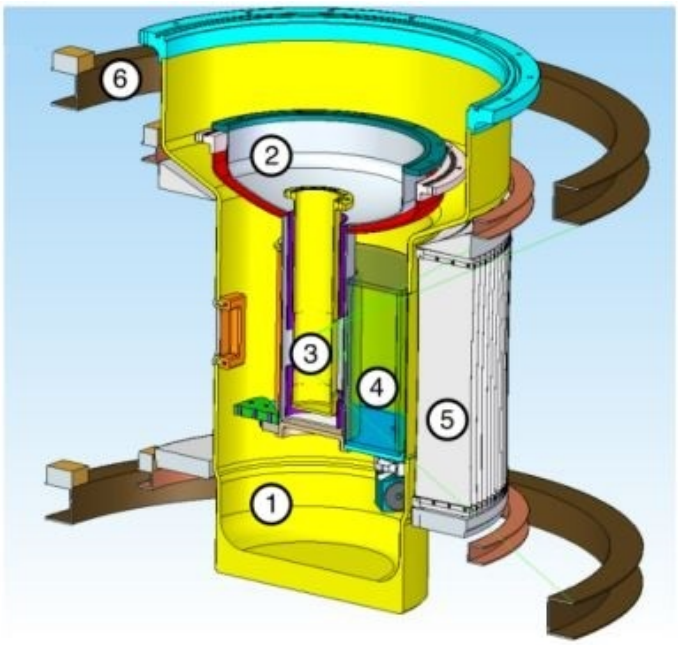

Figure 5.5: **Mechanical drawing cross-section of PA enabled LET sample position**. The analyser insert is comprised of the gas tank (1) which houses the cryostat (2) and the sample position (3). The ^{3}He spin-filter cell (4) sits on a shelf in the tail of the cryostat within the gas tank. Inside the main vacuum tank of LET are the radial oscillating collimator (5) with main holding field coils (6) above and below [28].

scatterer such as quartz [28]. Room temperature measurements of a quartz rod were performed by the instrument scientists using the same configuration from above.

5.4 Results

Polarised neutron scattering data collected using any technique requires substantial preprocessing before arriving at the isolated scattering cross sections. The polarised scattering data acquired on LET have undergone two crucial preprocessing steps. Initially, the data were reduced using custom python scripts developed by the instrument scientists at the ISIS neutron facility. This applies a correction for the finite detector efficiency using the scattering from a standard vanadium sample. The scattering from vanadium is expected to be uniform across all detector tubes since vanadium is a strongly incoherent scatterer with negligible coherent scattering cross section. Deviations from a uniform signal can arise due to the inherent variation in the efficiency of different detectors.This normalisation is performed on all LET data regardless of the neutron polarisation.

The data must also be corrected for absorption in the polarisation analyser and the finite efficiencies of the polariser, neutron spin flipper, and analyser. Quantifying the degree of inefficiency in the hardware enables the counts in each polarisation channel (nsf and sf) to be corrected for leakage between the channels. Fundamentally, this is achieved by determining the time-dependent flipping ratio using the scattering from a quartz sample and the transmitted beam monitor, as detailed in Ref. [28]. An ideal polarisation experiment with perfect polariser, flipper and analyser will only have counts in the nsf channel since quartz is a purely nuclear scatterer [84].

The advantage of performing polarised neutron scattering using the LET multi-detector spectrometer is the ability to survey large regions of reciprocal space, resolving both wave-vector and energy transfer. D7 has a multi-detector in the horizontal scattering plane, whereas LET employs an area detector with extensive out-of-plane coverage. Furthermore, D7 detectors measure the intensity integrated over energy transfer in their usual mode of operation, whereas LET always operates in a time-of-flight mode that resolves energy transfer. Hence, using LET it is possible to cover a very large range in reciprocal space, while at the same time to focus on small regions of Q and energy transfer. The magnetic diffuse scattering from $Ho_2Ti_2O_7$ is known to be elastic and, therefore, the analysis presented here focuses on the elastic line between -0.2 and 0.2 meV. Eliminating the scattering outside this window helps to reduce the background.

The nsf and sf signal measured with $E_i = 4\,\mathrm{meV}$ are shown in Figs. 5.6a and 5.6b after the corrections have been applied. A detector mask was applied to remove the straight-through beam and signal from regions not covered by the banana cell polarisation analyser. The sf channel exhibits a ϕ dependent signal at low 2θ which has an intensity maximum at the top of the detector. At the same 2θ position the nsf scattering exhibits an intensity maximum in the centre of the detector. The nsf channel also contains scattering from three Bragg reflections of $Ho_2Ti_2O_7$. Scattering intensities at low 2θ are modulated along the height of the detectors, see Fig. 5.6b. This modulation arises from a damaged polarisation analysis collimator and leads to significantly reduced intensity at the bottom of the detectors. The vanadium normalisation could not correct this behaviour since it was measured without any collimation.

The modulated intensities have been corrected using the nsf scattering from a

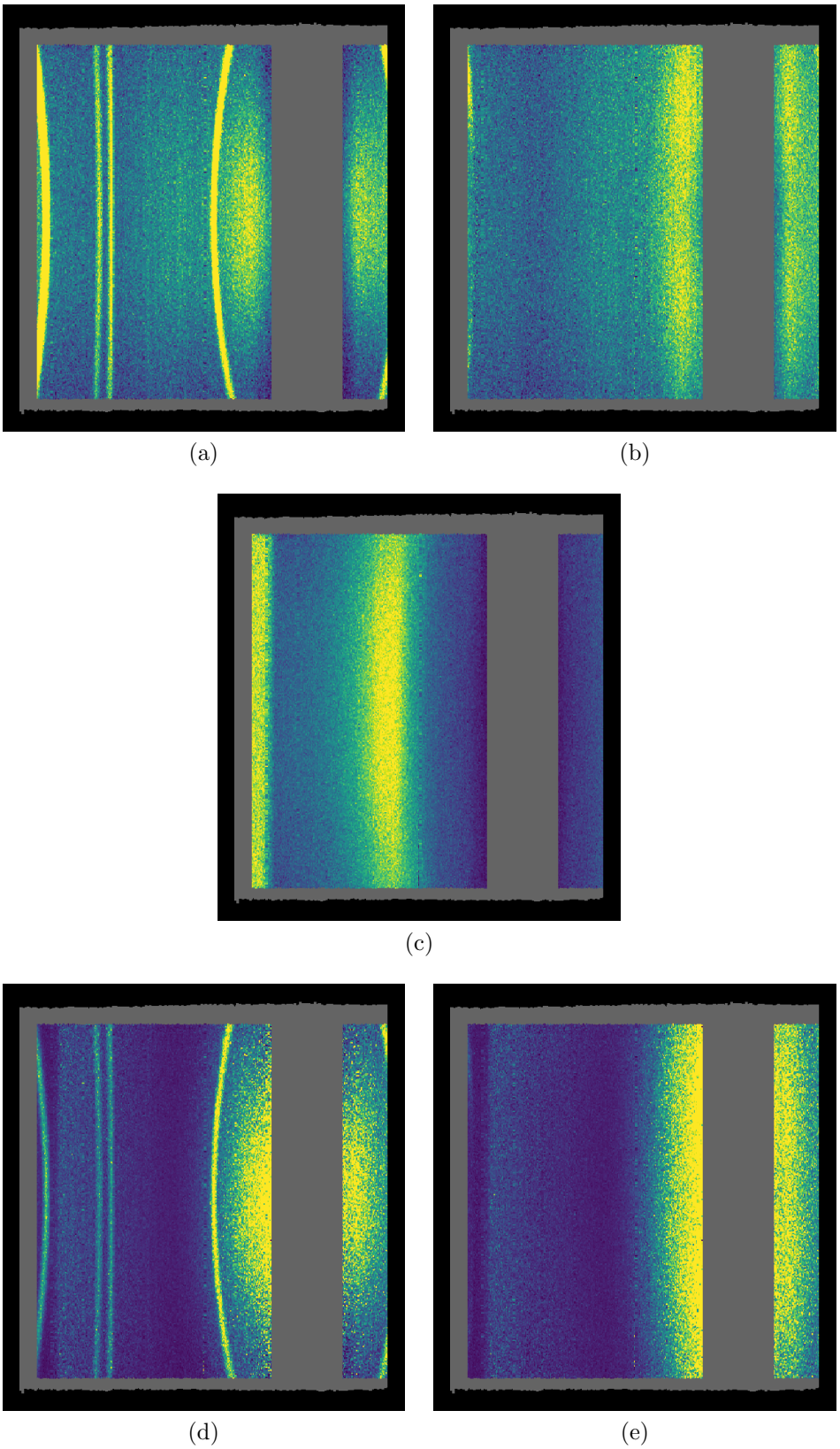

Figure 5.6: **Detector signal from $E_i = 4\,\mathrm{meV}$ data integrated over $-0.2 \leq \Delta E \leq 0.2\,\mathrm{meV}$.** (a) $Ho_2Ti_2O_7$ nsf at $T = 2\,\mathrm{K}$. (b) $Ho_2Ti_2O_7$ sf at $T = 2\,\mathrm{K}$. (c) Quartz nsf. (d) Quartz normalised $Ho_2Ti_2O_7$ nsf. (e) Quartz normalised $Ho_2Ti_2O_7$ sf. A detector mask was applied to only retain scattering signal from polarised neutrons and to exclude the straight-through beam.

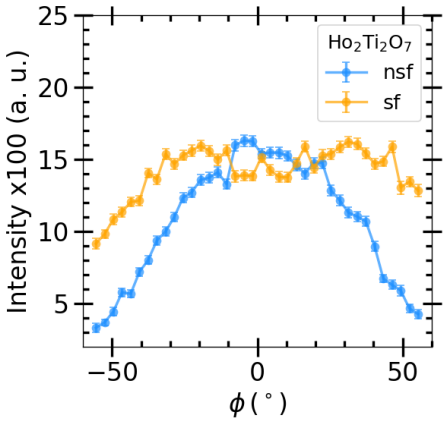

(a)

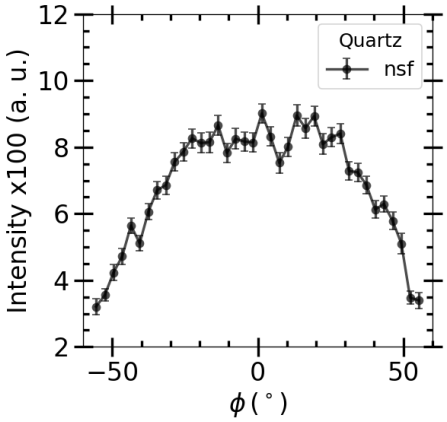

(b)

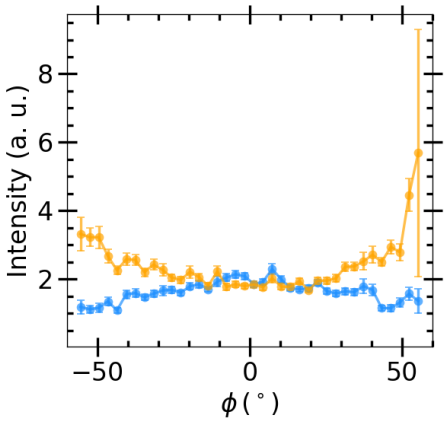

(c)

Figure 5.7: **The ϕ dependence of nsf and sf scattering before and after quartz correction**. Line plots show elastic scattering measured with $E_i = 4\,\text{meV}$ integrated over $28 - 30\,^\circ$ in 2θ. (a) $Ho_2Ti_2O_7$ data before division by quartz data. (b) Quartz nsf scattering. (c) $Ho_2Ti_2O_7$ data after quartz normalisation.

quartz sample also measured with the polarisation analysis collimator, see Fig. 5.6c. Scattering intensity from quartz is independent of ϕ because all of the scattering is structural. Therefore differences in the quartz intensity along the height of the tubes can only arise from the collimator, and dividing the data on $Ho_2Ti_2O_7$ by the quartz removes this behaviour. Figures 5.6d and 5.6e show both channels after this quartz correction.

Figure 5.7 better demonstrates the influence of the quartz correction on the ϕ dependence of scattering. At $2\theta = 29\,^\circ$, where there is strong magnetic diffuse scattering, the sf channel exhibits the incorrect ϕ dependence, see Fig. 5.7a. After the correction using quartz data shown in Fig. 5.7b, both the nsf and sf scattering exhibit the correct ϕ dependence as predicted by Eqs. (5.2a), (5.2b) and (5.3), see Fig. 5.7c.

The Q dependence of each cross section is calculated by simultaneously fitting Eqs. (5.2a) and (5.2b) to the ϕ dependence of nsf and sf scattering for a range of Q (or equivalently 2θ) values. The data in both channels were integrated over $2\,^\circ$ steps between $18 - 130\,^\circ$ in 2θ, and fitted with $\Delta E = 0.0(2)\,\mathrm{meV}$. The performance of the fits are shown in Fig. 5.8 for regions containing magnetic diffuse scattering and Bragg reflections. Figures 5.8b and 5.8d show that magnetic intensity can be extracted even in regions with strong Bragg reflections. The sensitivity of this approach is demonstrated in Fig. 5.8c, which shows that even very small magnetic signals are well described by Eq. (5.3).

The analysis procedure involves dividing each ϕ scan by the corresponding quartz data set, and that introduces an artificial Q dependence from the quartz. This is addressed by multiplying the cross sections with the Q-dependent quartz structure factor obtained by integrating the intensity over ϕ, see Fig. 5.9. The isolated nuclear

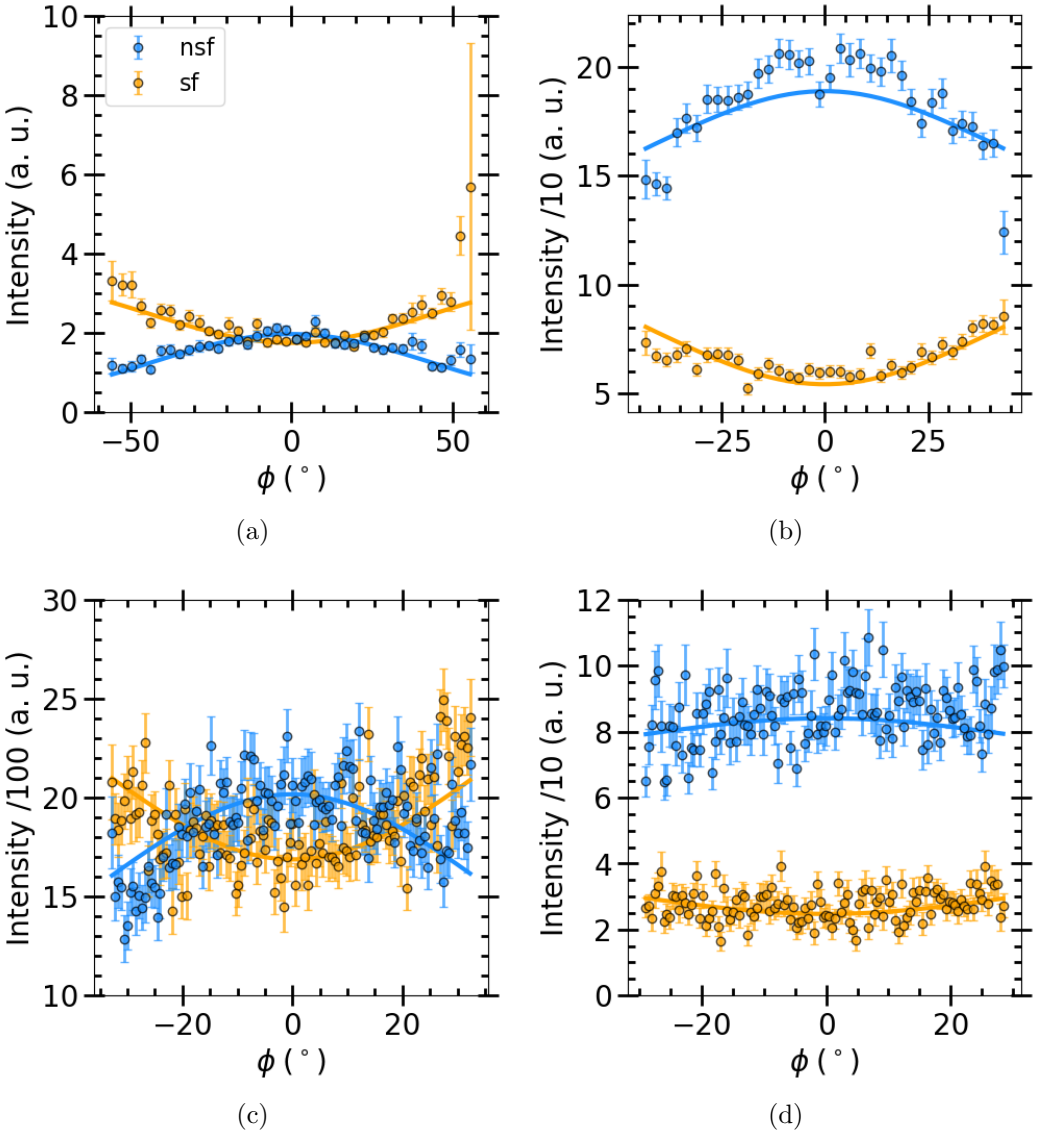

Figure 5.8: **Fits of ϕ-dependent nsf and sf scattering** (a) $2\theta = 28 - 30\,°$. (b) $2\theta = 44 - 46\,°$. (c) $2\theta = 62 - 64\,°$. (d) $2\theta = 94 - 96\,°$.

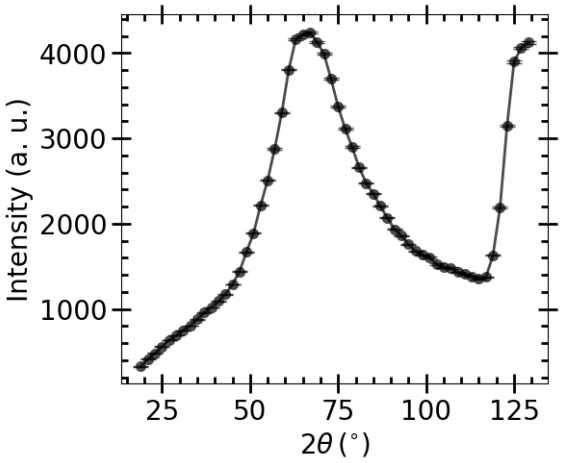

Figure 5.9: **Quartz structure factor**. Obtained by integrating over ϕ at each 2θ position.

cross section contains only the three expected Bragg reflections of $Ho_2Ti_2O_7$ at $Q \sim 1.07, 2.04$ and $2.14\,\text{Å}^{-1}$, see Fig. 5.10a. The incoherent cross section in Fig. 5.10b exhibits fluctuations about a constant intensity as expected.

The magnetic cross section measured on LET using the z+ technique is shown in Fig. 5.11. The Q-dependence of the magnetic cross section is compared with the experimental data of Hallas *et al.* obtained using *xyz* polarisation analysis and with their reverse Monte Carlo fit. The simpler z+ approach is in full agreement with the results from D7.

Relatively larger uncertainty in the cross sections determined using z+ polarisation analysis on LET may be explained by differences in neutron flux during the experiment. The experimental data of Hallas *et al.* is obtained using a white beam of neutrons and integrating over all energy transfer. In constrast, the energy-resolved LET data is obtained using a monochromatic beam of neutrons with $E_i = 4\,\text{meV}$. This leads to a reduction of up to 4 orders of magnitude in the incident neutron flux [149].

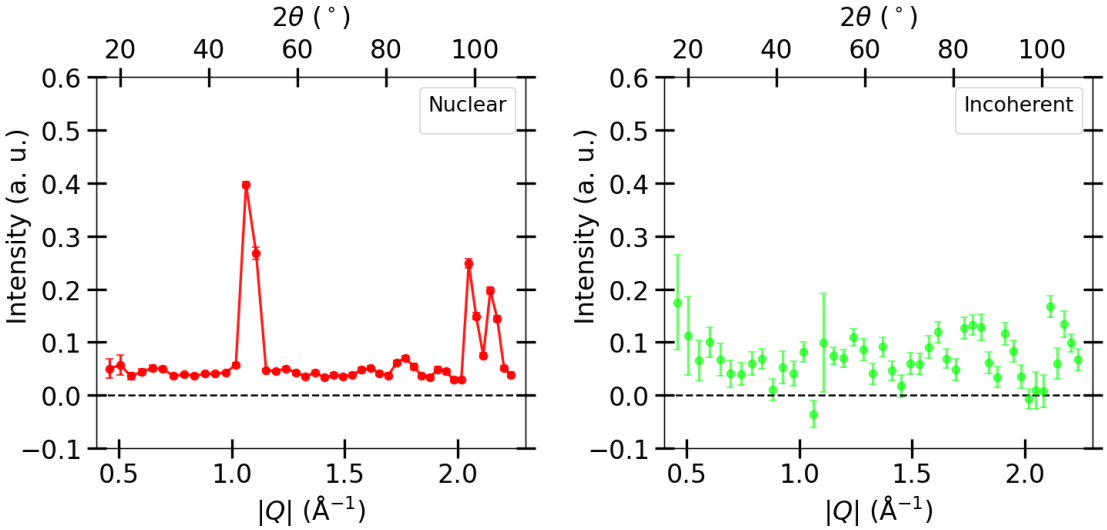

(a) (b)

Figure 5.10: **Separation of nuclear and incoherent cross sections**. (a) Nuclear cross section exhibits a relatively flat background with well defined Bragg reflections at $Q \sim 1.07, 2.04$ and $2.14\,\text{Å}^{-1}$. (b) The incoherent cross section can be approximated as flat scattering independent of Q.

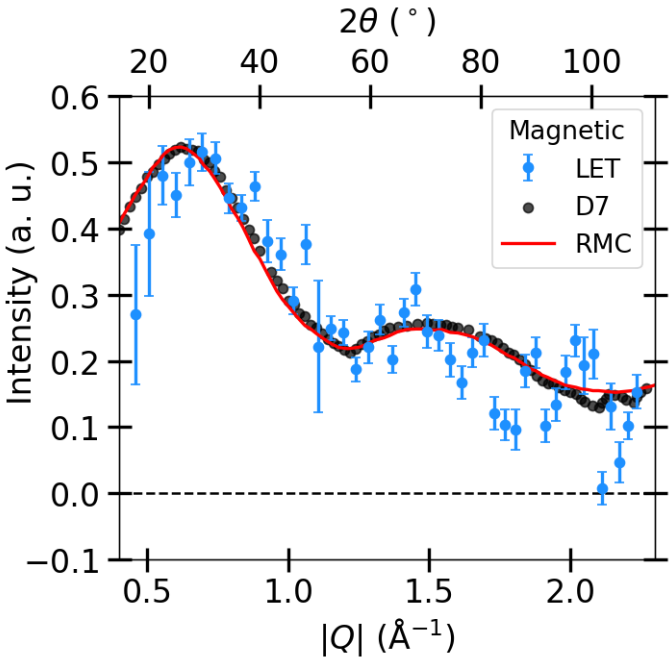

Figure 5.11: Q **dependence of the magnetic scattering cross section**. LET data points are shown as blue circles, D7 as black circles, and the reverse Monte Carlo fit from Ref. [26] as a red line. A scaling factor is used to plot the different data on the same axes.

The noise is necessarily larger in the magnetic and incoherent cross sections at the Q values corresponding to Bragg reflections due to relatively larger leakage from the nsf channel. The nuclear, magnetic and nuclear spin incoherent cross sections obtained using the z+ technique are entirely consistent with those obtained using *xyz* polarisation analysis.

5.5 Discussion & Conclusions

The z^+ polarisation analysis technique provides unambiguous separation of the nuclear, magnetic and nuclear spin incoherent scattering through measurements of only the non-spin-flip and spin-flip cross sections along the z-direction. For a paramagnetic-like scatterer, this is achieved through the variation of magnetic intensity around the Debye-Scherrer cone. Therefore this technique is only applicable to polycrystalline systems. Excellent description of the scattering in Fig. 5.8c is proof that full separation can be performed even when the magnetic signal is very weak. Polarisation analysis is also crucial for quasi-elastic neutron scattering, and the sensitivity of z^+ is well suited for component dependent studies of the dynamics in biological systems and battery materials.

The implementation on the direct geometry time-of-flight LET spectrometer demonstrates how well z^+ is suited to instruments which employ a large area multi-detector, such as WISH at the ISIS pulsed neutron facility [150], and CNCS at the Spallation Neutron Source (SNS) [151, 152]. The geometry of the holding field coils and the use of a ^{3}He spin-filter analyser enables polarisation analysis across the entire detector coverage without any obstructed zones. This makes z^+ the best performing polarisation analysis technique currently available at the ISIS neutron facility.

Combining this technique with the excellent energy resolution and repetition-rate-multiplication on LET offer great potential to study nuclear spin incoherent, nuclear and magnetic dynamics separately.

For single crystals, it is necessary to use xyz PA on triple-axis spectrometers. Recent developments of the PASTIS-3 concept have extended this to wider angle detectors [153]. However, for powder samples, the ability to use uniaxial PA and detector coverage over a very wide range both in and out of the horizontal scattering plane makes z^+ very competitive in terms of the efficient use of neutron beam time.

Similarities between z^+ and PASTIS-3 may indicate the design direction of future polarisation analysis development. New direct geometry time-of-flight spectrometers CSPEC at the European Spallation Source (ESS) [154] and CHESS at the SNS [155] could offer opportunities to perform polarised inelastic neutron scattering [156]. At ISIS, indirect geometry time-of-flight spectrometer MUSHROOM is planned to received similar polarisation analysis capability to allow component dependent studies of systems with slow dynamics [156,157]. The growing demand for polarised neutron instrumentation has also attracted much interest in new super-mirror geometries for wide-angle analysers, and improved ^{3}He cell designs to extend the characteristic cell lifetime.

Chapter 6

Summary and future outlook

This thesis has examined the microscopic dynamics in two classes of energy materials, with the aim of gaining insights into the role of diffusing ions in their performance. In the case of thermoelectric $AgCrSe_2$, the validity of the PLEC model was examined through *xyz* polarised QENS. Incoherent QENS shows that $AgCrSe_2$ does not qualify as a PLEC material since the diffusion rate is too slow to suppress the acoustic phonons. These results show that ultra-low lattice thermal conductivity can be maintained even when ionic diffusion is suppressed.

The diffuse QENS in the superionic phase arises mostly from coherent nuclear scattering with a contribution from damped magnons. At present, the significant coherent QENS is thought to arise from dynamic defects within the Ag layer. Two ways in which to extend this work would be to perform molecular dynamics simulations and temperature dependent single-crystal scattering to better understand the nature of the dynamic defects.

The spin Hamiltonian of the magnetic structure formed below $T_N \sim 55\,K$ was studied using high resolution neutron scattering and modelled with the SpinW pack-

age based on linear spin wave theory. The new Hamiltonian, with one ferromagnetic coupling $J_N \sim 2.88(1)\,\mathrm{meV}$ and two antiferromagnetic couplings $J_{NN} \sim (0.99(1)$ and $J_c \sim 0.16(2)\,\mathrm{meV}$, provides a good description of the resolvable spin wave excitations. Model quality may be further improved using polarised neutron scattering to isolate the magnetic cross-section.

The second class of energy material under investigation was the battery cathode material $Na_xFe_{1/2}Mn_{1/2}O_2$. At room temperature, superstructure formation in P2-$Na_{0.67}Fe_{1/2}Mn_{1/2}O_2$ is not suppressed by the disorder in the transition-metal layer, however the details of the resulting structure differ from the structure in P2-$Na_{0.8}CoO_2$. Exploring the superstructure formation as a function of temperature and Na concentration x, and comparing with previous results on Na_xCoO_2 will provide greater insights into the sensitivity of Na ions to changes in the local environment. This will require further computational modelling to determine the corresponding Na ordering at each point.

The diffusion mechanism in P2-$Na_{0.67}Fe_{1/2}Mn_{1/2}O_2$ differs from that proposed for P2-$Na_{0.8}CoO_2$, with both Na2-Na1 and Na2-Na2 jumps contributing to the observed Q-dependence of energy widths. At $T \sim 530\,\mathrm{K}$, P2-$Na_{0.67}Fe_{1/2}Mn_{1/2}O_2$ has a diffusion coefficient an order of magnitude greater than P2-$Na_{0.8}CoO_2$, with an activation energy that is lower by a factor two. The diffusion coefficient for O3-$Na_1Fe_{1/2}Mn_{1/2}O_2$ lies between the rates for the P2 compositions, with approximately half the activation energy of P2-$Na_{0.67}Fe_{1/2}Mn_{1/2}O_2$.

The diffusion rates and activations energies reported in this thesis are averaged over the two jumps in the new mechanism. It is necessary to perform momentum resolved spectroscopy on a single crystal of P2-$Na_{0.67}Fe_{1/2}Mn_{1/2}O_2$ to investigate the two jumps separately. For future measurements, it would be helpful to study single-

crystal samples using QENS. This would make it much easier to determine the Q-dependence of the energy widths, and that would make it easier to determine details of the hopping geometry. It would also be helpful to perform molecular dynamics simulations of the sodium-ion diffusion as has been performed for Na_xCoO_2, to enable direct comparison with the QENS.

The use of polarisation analysis has been crucial to the success of the studies summarised above. The z^+ technique reported in this thesis is able to unambiguously separate the nuclear spin incoherent, magnetic and nuclear contributions to the scattering by analysing the neutron polarisation only along the z-axis. The technique has the advantage of being an optional upgrade to existing instruments. Once the instrument is adapted, it is quick to install and uninstall the polarisation hardware necessary for z^+. However, the nature of this technique means it is only suitable for polycrystalline scattering on large-area detector neutron instruments.

z^+ analysis of elastic scattering from $Ho_2Ti_2O_7$ shows good agreement with simulations and experimental data previously reported using *xyz* polarisation analysis. It is worth noting that the reliance of z^+ on fitting makes it highly susceptible to systematic errors. Based on results presented here, the z^+ technique will be a highly effective method for QENS on systems with slow dynamics, such as energy materials. It will be informative to explore the performance of z^+ on inelastic scattering, where the scattering intensities are much lower.

Bibliography

[1] N. Yabuuchi, M. Kajiyama, *et al.*, "P2-type Nax[Fe1/2Mn1/2]O2 made from earth-abundant elements for rechargeable Na batteries," *Nature Materials*, vol. 11, pp. 512–517, jun 2012.

[2] X. L. Shi, J. Zou, and Z. G. Chen, "Advanced thermoelectric design: From materials and structures to devices," *Chemical Reviews*, vol. 120, no. 15, pp. 7399–7515, 2020.

[3] G. E. Murch, "Diffusion Kinetics in Solids," *Materials Science and Technology*, 2013.

[4] M. T. Dove, *Structure and Dynamics — An Atomic View of Materials*. Oxford: Oxford University Press, 2002.

[5] D. Sivia, *Elementary Scattering Theory*. Oxford University Press, jan 2011.

[6] A. T. Boothroyd, *Principles of Neutron Scattering from Condensed Matter*. Oxford University Press, jul 2020.

[7] B. T. M. Willis and C. J. Carlile, *Experimental Neutron Scattering*. Oxford: Oxford University Press, 2013.

[8] R. A. Ewings, J. R. Stewart, *et al.*, "Upgrade to the MAPS neutron time-of-flight chopper spectrometer," *Review of Scientific Instruments*, vol. 90, no. 3, 2019.

[9] R. I. Bewley, J. W. Taylor, and S. M. Bennington., "LET, a cold neutron multi-disk chopper spectrometer at ISIS," *Nuclear Instruments and Methods in Physics Research, Section A: Accelerators, Spectrometers, Detectors and Associated Equipment*, vol. 637, no. 1, pp. 128–134, 2011.

[10] "ThALES Characteristics."

[11] K. Beauvois and M. Klicpera, "All you need is neutron," 2015.

[12] T. J. Willis, *Determination of Diffusion Mechanisms in Battery Materials using Experimental and Computational Techniques*. PhD thesis, Royal Holloway, University of London, 2016.

[13] F. Gascoin and A. Maignan, "Order–Disorder Transition in AgCrSe 2 : a New Route to Efficient Thermoelectrics," *Chemistry of Materials*, vol. 23, pp. 2510–2513, may 2011.

[14] B. Li, H. Wang, *et al.*, "Liquid-like thermal conduction in intercalated layered crystalline solids," *Nature Materials*, vol. 17, no. 3, pp. 226–230, 2018.

[15] J. Ding, J. L. Niedziela, *et al.*, "Anharmonic lattice dynamics and superionic transition in AgCrSe 2," *Proceedings of the National Academy of Sciences*, p. 201913916, 2020.

[16] J. L. Niedziela, D. Bansal, *et al.*, "Selective breakdown of phonon quasiparticles across superionic transition in CuCrSe 2," *Nature Physics*, vol. 15, no. 1, pp. 73–78, 2019.

[17] F. M. Engelsman, G. A. Wiegers, *et al.*, "Crystal structures and magnetic structures of some metal(I) chromium(III) sulfides and selenides," *Journal of Solid State Chemistry*, vol. 6, no. 4, pp. 574–582, 1973.

[18] F. Damay, S. Petit, *et al.*, "Localised Ag+ vibrations at the origin of ultralow thermal conductivity in layered thermoelectric AgCrSe2," *Scientific Reports*, vol. 6, p. 23415, sep 2016.

[19] S. Toth and B. Lake, "Linear spin wave theory for single-Q incommensurate magnetic structures," *Journal of Physics Condensed Matter*, vol. 27, no. 16, pp. 1–12, 2015.

[20] N. Yabuuchi and S. Komaba, "Recent research progress on iron- and manganese-based positive electrode materials for rechargeable sodium batteries," *Science and Technology of Advanced Materials*, vol. 15, no. 4, 2014.

[21] T. J. Willis, D. G. Porter, *et al.*, "Diffusion mechanism in the sodium-ion battery material sodium cobaltate," *Scientific Reports*, vol. 8, no. 1, pp. 1–10, 2018.

[22] Y. Mo, S. P. Ong, and G. Ceder, "Insights into diffusion mechanisms in p2 layered oxide materials by first-principles calculations," *Chemistry of Materials*, vol. 26, no. 18, pp. 5208–5214, 2014.

[23] Y. Hinuma, Y. S. Meng, and G. Ceder, "Temperature-concentration phase diagram of P2-NaxCoO2 from first-principles calculations," *Physical Review B*, vol. 77, p. 224111, jun 2008.

[24] G. J. Shu and F. C. Chou, "Sodium-ion diffusion and ordering in single-crystal P2-NaxCoO2," *Physical Review B*, vol. 78, p. 052101, aug 2008.

[25] T. Fennell, P. P. Deen, *et al.*, "Magnetic Coulomb Phase in the Spin Ice Ho2Ti2O 7," *Science*, vol. 326, no. 5951, pp. 415–417, 2009.

[26] A. M. Hallas, J. A. Paddison, *et al.*, "Statics and dynamics of the highly correlated spin ice Ho 2Ge 2O 7," *Physical Review B - Condensed Matter and Materials Physics*, vol. 86, no. 13, pp. 1–5, 2012.

[27] G. J. Nilsen, J. Košata, *et al.*, "Polarisation analysis on the LET time-of-flight spectrometer," *Journal of Physics: Conference Series*, vol. 862, no. 1, p. 012019, 2017.

[28] G. Cassella, J. R. Stewart, *et al.*, "Polarization analysis on the LET cold neutron spectrometer using a 3 He spin-filter: first results," *Journal of Physics: Conference Series*, vol. 1316, p. 012007, oct 2019.

[29] E. Cemal, *Spin-wave measurements of sodium cobaltate and linarite using inelastic neutron scattering Eron Cemal*. PhD thesis, Royal Holloway, University of London, 2016.

[30] "COP26: The Glasgow Climate Pact," (Glasgow), United Nations Climate Change, 2021.

[31] G. J. Snyder and E. S. Toberer, "Complex thermoelectric materials," *Nature Materials*, vol. 7, no. 2, pp. 105–114, 2008.

[32] L. E. Bell, "Cooling, heating, generating power, and recovering waste heat with thermoelectric systems," *Science*, vol. 321, no. 5895, pp. 1457–1461, 2008.

[33] N. Espinosa, M. Lazard, *et al.*, "Modeling a Thermoelectric Generator Applied to Diesel Automotive Heat Recovery," *Journal of Electronic Materials*, vol. 39, pp. 1446–1455, sep 2010.

[34] D. T. Crane and J. W. LaGrandeur, "Progress Report on BSST-Led US Department of Energy Automotive Waste Heat Recovery Program," *Journal of Electronic Materials*, vol. 39, pp. 2142–2148, sep 2010.

[35] B. Orr, A. Akbarzadeh, *et al.*, "A review of car waste heat recovery systems utilising thermoelectric generators and heat pipes," *Applied Thermal Engineering*, vol. 101, pp. 490–495, may 2016.

[36] M. K. Ababneh, A. A. Al-Jarrah, *et al.*, "Recovering Waste Heat from Automobile Engine Using Thermoelectric Power Generators," *International Review of Mechanical Engineering (IREME)*, vol. 11, p. 845, nov 2017.

[37] Q. Cao, W. Luan, and T. Wang, "Performance enhancement of heat pipes assisted thermoelectric generator for automobile exhaust heat recovery," *Applied Thermal Engineering*, vol. 130, pp. 1472–1479, feb 2018.

[38] S. A. Mostafavi and M. Mahmoudi, "Modeling and fabricating a prototype of a thermoelectric generator system of heat energy recovery from hot exhaust

gases and evaluating the effects of important system parameters," *Applied Thermal Engineering*, vol. 132, pp. 624–636, mar 2018.

[39] G. Solbrekken, K. Yazawa, and A. Bar-Cohen, "Thermal management of portable electronic equipment using thermoelectric energy conversion," in *The Ninth Intersociety Conference on Thermal and Thermomechanical Phenomena In Electronic Systems (IEEE Cat. No.04CH37543)*, (Las Vegas), pp. 276–283, IEEE, 2004.

[40] Y. Zhou, S. Paul, and S. Bhunia, "Harvesting Wasted Heat in a Microprocessor Using Thermoelectric Generators: Modeling, Analysis and Measurement," in *2008 Design, Automation and Test in Europe*, pp. 98–103, IEEE, mar 2008.

[41] M. Guan, K. Wang, *et al.*, "Design and experimental investigation of a low-voltage thermoelectric energy harvesting system for wireless sensor nodes," *Energy Conversion and Management*, vol. 138, pp. 30–37, apr 2017.

[42] M. Al Musleh, E. Topriska, *et al.*, "Thermoelectric generator experimental performance testing for wireless sensor network application in smart buildings," *MATEC Web of Conferences*, vol. 120, p. 08003, aug 2017.

[43] T. Torfs, V. Leonov, *et al.*, "Body-Heat Powered Autonomous Pulse Oximeter," in *2006 5th IEEE Conference on Sensors*, pp. 427–430, IEEE, oct 2006.

[44] A. Amar, A. Kouki, and H. Cao, "Power Approaches for Implantable Medical Devices," *Sensors*, vol. 15, pp. 28889–28914, nov 2015.

[45] A. R. M. Siddique, R. Rabari, *et al.*, "Thermal energy harvesting from the human body using flexible thermoelectric generator (FTEG) fabricated by a dispenser printing technique," *Energy*, vol. 115, pp. 1081–1091, nov 2016.

[46] A. R. M. Siddique, S. Mahmud, and B. V. Heyst, "A review of the state of the science on wearable thermoelectric power generators (TEGs) and their existing challenges," *Renewable and Sustainable Energy Reviews*, vol. 73, pp. 730–744, jun 2017.

[47] M. Thielen, L. Sigrist, *et al.*, "Human body heat for powering wearable devices: From thermal energy to application," *Energy Conversion and Management*, vol. 131, pp. 44–54, jan 2017.

[48] N. Jaziri, A. Boughamoura, *et al.*, "A comprehensive review of Thermoelectric Generators: Technologies and common applications," *Energy Reports*, vol. 6, pp. 264–287, 2020.

[49] H. Liu, X. Shi, *et al.*, "Copper ion liquid-like thermoelectrics," *Nature Materials*, vol. 11, no. 5, pp. 422–425, 2012.

[50] K. Trachenko, "Heat capacity of liquids: An approach from the solid phase," *Physical Review B - Condensed Matter and Materials Physics*, vol. 78, p. 104201, sep 2008.

[51] S. Hameer and J. L. van Niekerk, "A review of large-scale electrical energy storage," *International Journal of Energy Research*, vol. 39, pp. 1179–1195, jul 2015.

[52] J. M. Tarascon and M. Armand, "Issues and challenges facing rechargeable lithium batteries," *Nature*, vol. 414, pp. 359–367, nov 2001.

[53] N. Nitta, F. Wu, *et al.*, "Li-ion battery materials: present and future," *Materials Today*, vol. 18, pp. 252–264, jun 2015.

[54] F. Risacher and B. Fritz, "Origin of Salts and Brine Evolution of Bolivian and Chilean Salars," *Aquatic Geochemistry*, vol. 15, pp. 123–157, feb 2009.

[55] A. Yaksic and J. E. Tilton, "Using the cumulative availability curve to assess the threat of mineral depletion: The case of lithium," *Resources Policy*, vol. 34, pp. 185–194, dec 2009.

[56] C. Grosjean, P. H. Miranda, *et al.*, "Assessment of world lithium resources and consequences of their geographic distribution on the expected development of the electric vehicle industry," *Renewable and Sustainable Energy Reviews*, vol. 16, pp. 1735–1744, apr 2012.

[57] M. D. Slater, D. Kim, *et al.*, "Sodium-ion batteries," *Advanced Functional Materials*, vol. 23, no. 8, pp. 947–958, 2013.

[58] B. L. Ellis and L. F. Nazar, "Sodium and sodium-ion energy storage batteries," *Current Opinion in Solid State and Materials Science*, vol. 16, no. 4, pp. 168–177, 2012.

[59] M. H. Han, E. Gonzalo, *et al.*, "A comprehensive review of sodium layered oxides: Powerful cathodes for Na-ion batteries," *Energy and Environmental Science*, vol. 8, no. 1, pp. 81–102, 2015.

[60] F. J. Disalvo, "Thermoelectric cooling and power generation," *Science*, vol. 285, no. 5428, pp. 703–706, 1999.

[61] K. S. Ong, L. Jiang, and K. C. Lai, "4.20 Thermoelectric Energy Conversion," in *Comprehensive Energy Systems*, vol. 4-5, pp. 794–815, Elsevier, 2018.

[62] D. Wu, S. Huang, *et al.*, "Revisiting AgCrSe2 as a promising thermoelectric material," *Physical Chemistry Chemical Physics*, vol. 18, no. 34, pp. 23872–23878, 2016.

[63] P. Ren, Y. Liu, *et al.*, "Recent advances in inorganic material thermoelectrics," *Inorganic Chemistry Frontiers*, vol. 5, no. 10, pp. 2380–2398, 2018.

[64] D. G. Porter, *Control of electrons through patterning of superstructures in sodium cobaltate*. PhD thesis, Royal Holloway, University of London, 2012.

[65] R. Venkatasubramanian, E. Siivola, *et al.*, "Thin-film thermoelectric devices with high room-temperature figures of merit," *Nature*, vol. 413, pp. 597–602, oct 2001.

[66] T. C. Harman, P. J. Taylor, *et al.*, "Quantum Dot Superlattice Thermoelectric Materials and Devices," *Science*, vol. 297, pp. 2229–2232, sep 2002.

[67] B. Poudel, Q. Hao, *et al.*, "High-Thermoelectric Performance of Nanostructured Bismuth Antimony Telluride Bulk Alloys," *Science*, vol. 320, pp. 634–638, may 2008.

[68] J. Ma, O. Delaire, *et al.*, "Glass-like phonon scattering from a spontaneous nanostructure in AgSbTe 2," *Nature Nanotechnology*, vol. 8, no. 6, pp. 445–451, 2013.

[69] D. J. Voneshen, K. Refson, *et al.*, "Suppression of thermal conductivity by rattling modes in thermoelectric sodium cobaltate," *Nature Materials*, vol. 12, no. 11, pp. 1028–1032, 2013.

[70] O. Delaire, J. Ma, *et al.*, "Giant anharmonic phonon scattering in PbTe," *Nature Materials*, vol. 10, no. 8, pp. 614–619, 2011.

[71] C. W. Li, J. Hong, *et al.*, "Orbitally driven giant phonon anharmonicity in SnSe," *Nature Physics*, vol. 11, no. 12, pp. 1063–1069, 2015.

[72] D. J. Voneshen, H. C. Walker, *et al.*, "Hopping Time Scales and the Phonon-Liquid Electron-Crystal Picture in Thermoelectric Copper Selenide," *Physical Review Letters*, vol. 118, no. 14, pp. 1–5, 2017.

[73] D. W. Murphy, "Superionic Conduction in AgCrS2 and AgCrSe2," *Journal of The Electrochemical Society*, vol. 124, no. 8, p. 1268, 1977.

[74] R. A. Yakshibayev, V. N. Zabolotsky, and R. F. Almukhametov, "Structural features and ionic transport in two-dimensional MxYSe2 (M = Cu, Ag; Y = Cr, Nb) mixed conductors," *Solid State Ionics*, vol. 31, pp. 1–4, oct 1988.

[75] Y. He, T. Zhang, *et al.*, "High thermoelectric performance in copper telluride," *NPG Asia Materials*, vol. 7, no. 8, 2015.

[76] S. Bhattacharya, R. Basu, *et al.*, "CuCrSe2: A high performance phonon glass and electron crystal thermoelectric material," *Journal of Materials Chemistry A*, vol. 1, no. 37, pp. 11289–11294, 2013.

[77] W. L. R. e. James R. Birk (auth.) Gerald D. Mahan, *Superionic Conductors*. Physics of Solids and Liquids, Boston, MA: Springer US, 1 ed., 1976.

[78] J. Boyce and B. Huberman, "Superionic conductors: Transitions, structures, dynamics," *Physics Reports*, vol. 51, pp. 189–265, apr 1979.

[79] R. Hempelmann, *Quasielastic Neutron Scattering and Solid State Diffusion*. Oxford University Press, nov 2010.

[80] J. Haus and K. Kehr, "Diffusion in regular and disordered lattices," *Physics Reports*, vol. 150, pp. 263–406, jun 1987.

[81] H. Eyring, "The activated complex in chemical reactions," *The Journal of Chemical Physics*, vol. 3, no. 2, pp. 63–71, 1935.

[82] A. E. Stearn and H. Eyring, "Absolute rates of solid reactions: Diffusion," *Journal of Physical Chemistry*, vol. 44, no. 8, pp. 955–980, 1940.

[83] C. C. Miller, "The Stokes-Einstein law for diffusion in solution," *Proceedings of the Royal Society of London. Series A, Containing Papers of a Mathematical and Physical Character*, vol. 106, pp. 724–749, dec 1924.

[84] J. R. Stewart, P. P. Deen, *et al.*, "Disordered materials studied using neutron polarization analysis on the multi-detector spectrometer, D7," *Journal of Applied Crystallography*, vol. 42, no. 1, pp. 69–84, 2009.

[85] R. M. Moon, T. Riste, and W. C. Koehler, "Polarization analysis of thermal-neutron scattering," *Physical Review*, vol. 181, no. 2, pp. 920–931, 1969.

[86] O. Schärpf and H. Capellmann, "TheXYZ-Difference Method with Polarized Neutrons and the Separation of Coherent, Spin Incoherent, and Magnetic Scattering Cross Sections in a Multidetector," *Physica Status Solidi (a)*, vol. 135, pp. 359–379, feb 1993.

[87] S. H. Simon, *Oxford Solid State Physics*. Oxford: Oxford University Press, first ed., 2013.

[88] T. Janssen, A. Janner, *et al.*, "Incommensurate and commensurate modulated structures," in *International Tables for Crystallography*, vol. C, pp. 907–955, Chester, England: International Union of Crystallography, oct 2006.

[89] G. L. Squires, *Introduction to the Theory of Thermal Neutron Scattering*. New York: Dover, 1996.

[90] A.-J. Dianoux and G. Lander, *Neutron Data Booklet*. Philadelphia: Old City, 2 ed., 2003.

[91] C. T. Chudley and R. J. Elliott, "Neutron scattering from a liquid on a jump diffusion model," *Proceedings of the Physical Society*, vol. 77, no. 2, pp. 353–361, 1961.

[92] J. P. Embs, F. Juranyi, and R. Hempelmann, "Introduction to Quasielastic Neutron Scattering," *Zeitschrift für Physikalische Chemie*, vol. 224, pp. 5–32, feb 2010.

[93] E. Ressouche, "Polarized neutron diffraction," *École thématique de la Société Française de la Neutronique*, vol. 13, p. 02002, 2014.

[94] M. Enderle, "Neutrons and magnetism," *École thématique de la Société Française de la Neutronique*, vol. 13, p. 01002, 2014.

[95] M. Blume, "Polarization Effects in the Magnetic Elastic Scattering of Slow Neutrons," *Physical Review*, vol. 130, pp. 1670–1676, jun 1963.

[96] S. V. Maleev, V. G. Bar'yakhtar, and R. A. Suris, "The Scattering of Slow Neutrons by Complex Magnetic Structures," *Soviet Phys.-Solid State*, vol. 4, pp. 2533–9, 1963.

[97] D. J. Findlay, "ISIS - Pulsed neutron and muon source," *Proceedings of the IEEE Particle Accelerator Conference*, pp. 695–699, 2007.

[98] G. J. Nilsen, "Oxford School on Neutron Scattering - Polarized neutron scattering," 2019.

[99] J. B. Hayter, "Matrix analysis of neutron spin-echo," *Zeitschrift für Physik B Condensed Matter and Quanta*, vol. 31, pp. 117–125, mar 1978.

[100] A. R. Wildes, "Scientific Reviews: Neutron Polarization Analysis Corrections Made Easy," *Neutron News*, vol. 17, no. 2, pp. 17–25, 2006.

[101] P. J. Brown, A. G. Fox, *et al.*, "Intensity of diffracted intensities," in *International Tables for Crystallography*, pp. 554–595, Chester, England: International Union of Crystallography, oct 2006.

[102] "Xcalibur, Gemini User Manual," 2014.

[103] "HyPix-6000HE."

[104] "The 800 series Cryostream."

[105] A. Maignan, E. Guilmeau, *et al.*, "Revisiting some chalcogenides for thermoelectricity," *Science and Technology of Advanced Materials*, vol. 13, no. 5, 2012.

[106] P. F. Bongers, C. F. Van Bruggen, *et al.*, "Structures and magnetic properties of some metal (I) chromium (III) sulfides and selenides," *Journal of Physics and Chemistry of Solids*, vol. 29, no. 6, pp. 977–984, 1968.

[107] A. Van Der Lee and G. A. Wiegers, "Anharmonic thermal motion of Ag in AgCrSe2: A high-temperature single-crystal X-ray diffraction study," *Journal of Solid State Chemistry*, vol. 82, pp. 216–224, oct 1989.

[108] J. Frenkel, *Kintetic Theory of Liquids*. Oxford University Press, 1946.

[109] P. Brüesch, *Phonons: Theory and Experiments I*, vol. 34 of *Springer Series in Solid-State Sciences*. Berlin, Heidelberg: Springer Berlin Heidelberg, 1982.

[110] G. L. Squires, *Introduction to the Theory of Thermal Neutron Scattering*. Cambridge: Cambridge University Press, 2012.

[111] M. Bee, *Quasielastic neutron scattering : principles and applications in solid state chemistry, biology and materials science*. Bristol; Philadelphia: A. Hilger, 1988.

[112] M. More, J. Lefebvre, *et al.*, "Neutron diffuse scattering in the disordered phase of CrBr4. I. Experimental. Elastic and quasi-elastic coherent scattering in single crystals," *Journal of Physics C: Solid State Physics*, vol. 13, no. 15, pp. 2833–2846, 1980.

[113] A. P. Murani, "Recent Experimental Studies of Dynamics of Spin Glasses," *Le Journal de Physique Colloques*, vol. 39, no. C6, pp. C6–1517–C6–1526, 1978.

[114] B. D. Rainford, R. Cywinski, and S. J. Dakin, "Neutron and μSR studies of spin fluctuations in YMn2 and related alloys," *Journal of Magnetism and Magnetic Materials*, vol. 140-144, no. PART 2, pp. 805–806, 1995.

[115] U. K. Gautam, R. Seshadri, *et al.*, "Magnetic and transport properties, and electronic structure of the layered chalcogenide AgCrSe2," *Solid State Communications*, vol. 122, pp. 607–612, jun 2002.

[116] M. Boehm, A. Hiess, *et al.*, "ThALES - Three axis low energy spectroscopy at the Institut Laue-Langevin," *Measurement Science and Technology*, vol. 19, no. 3, 2008.

[117] O. Arnold, J. C. Bilheux, *et al.*, "Mantid - Data analysis and visualization package for neutron scattering and μ SR experiments," *Nuclear Instruments and Methods in Physics Research, Section A: Accelerators, Spectrometers, Detectors and Associated Equipment*, vol. 764, pp. 156–166, 2014.

[118] V. F. Sears, "Neutron scattering lengths and cross sections," *Neutron News*, vol. 3, pp. 26–37, jan 1992.

[119] L. Xie, D. Wu, *et al.*, "Direct atomic-scale observation of the Ag + diffusion structure in the quasi-2D "liquid-like" state of superionic thermoelectric AgCrSe2," *Journal of Materials Chemistry C*, vol. 7, no. 30, pp. 9263–9269, 2019.

[120] M. H. Dickens, W. Hayes, *et al.*, "Neutron scattering studies of acoustic phonon modes in PbF2 up to high temperatures," *Journal of Physics C: Solid State Physics*, vol. 12, no. 1, pp. 17–25, 1979.

[121] M. T. Hutchings, K. Clausen, *et al.*, "Investigation of thermally induced anion disorder in fluorites using neutron scattering techniques," *Journal of Physics C: Solid State Physics*, vol. 17, pp. 3903–3940, aug 1984.

[122] M. H. Dickens, W. Hayes, *et al.*, "Incoherent quasielastic neutron scattering investigation of chlorine ion hopping in the fast-ion phase of strontium chloride," *Journal of Physics C: Solid State Physics*, vol. 16, pp. L1–L6, jan 1983.

[123] C. Delmas, C. Fouassier, and P. Hagenmuller, "Structural classification and properties of the layered oxides," *Physica B+C*, vol. 99, pp. 81–85, jan 1980.

[124] C. Delmas, J. Braconnier, *et al.*, "Electrochemical intercalation of sodium in NaxCoO2 bronzes," *Solid State Ionics*, vol. 3-4, pp. 165–169, aug 1981.

[125] Q. Huang, M. L. Foo, *et al.*, "Coupling between electronic and structural degrees of freedom in the triangular lattice conductor ¡math display="inline"¿ ¡mrow¿ ¡msub¿ ¡mi mathvariant="normal"¿Na¡/mi¿ ¡mi¿x¡/mi¿ ¡/msub¿ ¡mi mathvariant="normal"¿Co¡/mi¿ ¡msub¿ ¡mi mathvariant="normal"¿O¡," *Physical Review B*, vol. 70, p. 184110, nov 2004.

[126] L. Viciu, J. W. Bos, *et al.*, "Crystal structure and elementary properties of Nax Co O2 (x=0.32, 0.51, 0.6, 0.75, and 0.92) in the three-layer NaCo O2 family," *Physical Review B - Condensed Matter and Materials Physics*, vol. 73, no. 17, pp. 1–10, 2006.

[127] A. Van der Ven, G. Ceder, *et al.*, "First-principles theory of ionic diffusion with nondilute carriers," *Physical Review B - Condensed Matter and Materials Physics*, vol. 64, no. 18, pp. 1–17, 2001.

[128] M. Roger, D. J. Morris, *et al.*, "Patterning of sodium ions and the control of electrons in sodium cobaltate," *Nature*, vol. 445, no. 7128, pp. 631–634, 2007.

[129] Y. Mo, S. P. Ong, and G. Ceder, "First Principles Study of the Li 10 GeP 2 S 12 Lithium Super Ionic Conductor Material," *Chemistry of Materials*, vol. 24, pp. 15–17, jan 2012.

[130] F. Risacher and B. Fritz, "Origin of Salts and Brine Evolution of Bolivian and Chilean Salars," *Aquatic Geochemistry*, vol. 15, pp. 123–157, feb 2009.

[131] A. Yaksic and J. E. Tilton, "Using the cumulative availability curve to assess the threat of mineral depletion: The case of lithium," *Resources Policy*, vol. 34, pp. 185–194, dec 2009.

[132] S. Uthayakumar, M. S. Pandiyan, *et al.*, "Crystal growth and neutron diffraction studies of Li x CoO 2 bulk single crystals," *Journal of Crystal Growth*, vol. 401, pp. 169–172, sep 2014.

[133] S. M. Koohpayeh, D. Fort, and J. S. Abell, "The optical floating zone technique: A review of experimental procedures with special reference to oxides," *Progress in Crystal Growth and Characterization of Materials*, vol. 54, no. 3-4, pp. 121–137, 2008.

[134] "CrysAlis Pro Software System," 2019.

[135] M. S. Pandiyan, *Phase Diagram and Control of Thermoelectric Properties of Sodium Cobaltate*. PhD thesis, Royal Holloway, University of London, 2013.

[136] Y. S. Meng, Y. Hinuma, and G. Ceder, "An investigation of the sodium patterning in NaxCoO2 (0.5¡x¡1) by density functional theory methods," *The Journal of Chemical Physics*, vol. 128, p. 104708, mar 2008.

[137] H. Alloul, I. R. Mukhamedshin, *et al.*, "Na ordering imprints a metallic kagomé lattice onto the Co planes of Na2/3CoO2," *Epl*, vol. 85, no. 4, 2009.

[138] D. G. Porter, "Dans-Diffraction," 2020.

[139] S. Palit, "Dielectric and magnetic investigations on novel P-2 type layered oxides," *IOSR Journal of Applied Physics*, vol. 6, no. 6, pp. 59–69, 2014.

[140] V. Duffort, E. Talaie, *et al.*, "Uptake of CO 2 in Layered P2-Na 0.67 Mn 0.5 Fe 0.5 O 2 : Insertion of Carbonate Anions," *Chemistry of Materials*, vol. 27, pp. 2515–2524, apr 2015.

[141] R. Balsys, "Refinement of the structure of Na0.74CoO2 using neutron powder diffraction," *Solid State Ionics*, vol. 93, pp. 279–282, jan 1997.

[142] G. Ehlers, J. R. Stewart, *et al.*, "Generalization of the classical xyz-polarization analysis technique to out-of-plane and inelastic scattering," *Review of Scientific Instruments*, vol. 84, no. 9, 2013.

[143] M. J. Harris, S. T. Bramwell, *et al.*, "Geometrical Frustration in the Ferromagnetic Pyrochlore Ho2Ti2O7," *Physical Review Letters*, vol. 79, pp. 2554–2557, sep 1997.

[144] C. Castelnovo, R. Moessner, and S. L. Sondhi, "Magnetic monopoles in spin ice," *Nature*, vol. 451, no. 7174, pp. 42–45, 2008.

[145] G. Sala, *Spin Ice: a Wonderful World*. PhD thesis, Royal Holloway, University of London, 2014.

[146] O. Schärpf and H. Capellmann, "TheXYZ-Difference Method with Polarized Neutrons and the Separation of Coherent, Spin Incoherent, and Magnetic Scattering Cross Sections in a Multidetector," *Physica Status Solidi (a)*, vol. 135, pp. 359–379, feb 1993.

[147] G. J. Nilsen, "Private correspondence," 2019.

[148] J. Košata, G. J. Nilsen, *et al.*, "Polarized primary spectrometer on the LET instrument at ISIS," *Physica B: Condensed Matter*, vol. 551, no. November, pp. 476–479, 2018.

[149] D. J. Voneshen, "Private correspondence," 2021.

[150] L. C. Chapon, P. Manuel, *et al.*, "Wish: The New Powder and Single Crystal Magnetic Diffractometer on the Second Target Station," *Neutron News*, vol. 22, pp. 22–25, apr 2011.

[151] D. L. Abernathy, M. B. Stone, *et al.*, "Design and operation of the wide angular-range chopper spectrometer ARCS at the Spallation Neutron Source," *Review of Scientific Instruments*, vol. 83, p. 015114, jan 2012.

[152] G. Ehlers, A. A. Podlesnyak, *et al.*, "The new cold neutron chopper spectrometer at the Spallation Neutron Source: Design and performance," *Review of Scientific Instruments*, vol. 82, p. 085108, aug 2011.

[153] D. Jullien, A. Petoukhov, *et al.*, "New design of a magnetic device for wide-angle XYZ polarization analysis PASTIS-3, from the concept to first tests with

thermal neutrons," *Nuclear Instruments and Methods in Physics Research, Section A: Accelerators, Spectrometers, Detectors and Associated Equipment*, vol. 1010, no. November 2020, p. 165558, 2021.

[154] P. P. Deen, S. Longeville, *et al.*, "CSPEC: The cold chopper spectrometer of the ESS, a detailed overview prior to commissioning," *Review of Scientific Instruments*, vol. 92, p. 105104, oct 2021.

[155] G. Sala, J. Y. Lin, *et al.*, "Conceptual design of CHESS, a new direct-geometry inelastic neutron spectrometer dedicated to studying small samples," *Journal of Applied Crystallography*, vol. 51, no. 2, pp. 282–293, 2018.

[156] G. J. Nilsen and C. Niedermayer, "LENS Webinar 3, New Directions in Instrumentation: Polarized time-of-flight spectroscopy," 2020.

[157] R. I. Bewley, "The Mushroom neutron spectrometer," *Nuclear Instruments and Methods in Physics Research, Section A: Accelerators, Spectrometers, Detectors and Associated Equipment*, vol. 998, no. January, p. 165077, 2021.